University of South Carolina
Scholar Commons

2018

Study Of 4H-SiC And ALxGA1-xN Based Heterojunction Devices For Ultraviolet Detection Applications

Venkata Surya Naga Raju Chava
University of South Carolina

STUDY OF 4H-SIC AND AL$_X$GA$_{1-X}$N BASED HETEROJUNCTION DEVICES FOR ULTRAVIOLET DETECTION APPLICATIONS

by

Venkata Surya Naga Raju Chava

Bachelor of Science
Andhra University, 2006

Master of Science
Andhra University, 2008

Master of Technology
Indian Institute of Technology Delhi, 2012

_____

Submitted in Partial Fulfillment of the Requirements

For the Degree of Doctor of Philosophy in

Electrical Engineering

College of Engineering and Computing

University of South Carolina

2018

Accepted by:

MVS Chandrashekhar, Major Professor

Tangali S. Sudarshan, Committee Member

Guoan Wang, Committee Member

Andrew B. Greytak, Committee Member

Cheryl L. Addy, Vice Provost and Dean of the Graduate School

ii

ACKNOWLEDGMENTS

First, I would like to express my deepest gratitude to my advisor Dr. MVS Chandrashekhar, for his constant support and guidance over the last four years. I would also like to thank my mentor and committee member Prof. T.S. Sudarshan for being a great source of inspiration and also for his endless support for my research work. I thank my Ph.D. committee member Dr. Guoan Wang for his support and encouragement. I would like to thank my committee member Dr. Andrew B. Greytak for his valuable suggestions and support during this research.

I would like to thank Prof. Asif Khan for allowing me to use his characterization lab. I thank Prof. Simin for his valuable feedback on my research work. I am indebted to all my past and present colleagues: Ifat, Anusha, Josh, Ken, Omar, and Mukta for all their help and many stimulating discussions during my Ph.D. I would also like to thank Dr. Kevin Daniels and Bobby for their help during this work. I would also like to thank all the members of Prof. Khan's group who helped me during this work.

I would also like to express my gratitude to all my teachers for their guidance and encouragement. I would also like to convey my heartfelt thanks to all my friends for always being there to encourage and support me. Last, but not the least, I would like to thank my parents and sister for their endless support throughout my life.

ABSTRACT

Ultraviolet (UV) detectors are important for their applications in flame detection, furnace gas control systems, plume monitoring etc. Due to their wide band-gap, 4H-SiC (E_g=3.26eV) and III-V semiconductors such as GaN (E_g=3.4eV), $Al_xGa_{1-x}N$ (E_g=3.4eV to 6.2eV) etc., are excellent candidates for visible($\lambda_{cut-0ff}$=400nm) and solar blind($\lambda_{cut-0ff}$=290nm) UV detectors. Conventional SiC UV detectors suffer from poor UV responsivities due to reflection/absorption/transmission losses caused by the metal electrodes used in those detectors.

In the first part, a novel bipolar transistor with epitaxial graphene(EG)/p-SiC (30µm)/n^+-SiC substrate was fabricated and characterized. The 2-3 ML thick, transparent and conducting, EG used in this work was grown by using thermal sublimation of SiC. Under 0.43 µW 365nm UV illumination, this device showed a responsivity(R) of 7.1A/W better than or comparable to the state of the art SiC Schottky and PiN diodes, and a bipolar current gain of 113, when operated in the Schottky emitter(SE) mode. Further, a UV-visible rejection (R_{365}: R_{444}) >10^3 is estimated for this device.

In the second part, EG/p-SiC(13µm)/ n^+-SiC bipolar transistor device structures were fabricated, where EG was grown by selectively etching Si from SiC using a novel Tetrafluorosilane(SiF_4) precursor. The photo-transistor showed responsivity as high as 25 A/W at 250 nm in the SE mode. The SC mode showed a responsivity of 17A/W at 270nm with a visible rejection (R_{270}: R_{400})>10^3. The fastest response was seen in the SC-mode,

with 10ms turn-on and 47ms turn-off, with a noise equivalent power(NEP) of 2.3fW at 20 Hz and a specific detectivity of 4.4×10^{13} Jones.

In the final part, HEMT devices with $Al_{0.85}Ga_{0.15}N/Al_{0.65}Ga_{0.35}N$ as barrier and channel layers, were fabricated and characterized. These devices showed a photo-responsivity $\sim 1 \times 10^{6}$A/W at 220nm, with solar and visible rejection $\sim 10^{2}$ limited by sub-bandgap states in the AlGaN. The lowest NEP was observed near the threshold voltage, 4.7fW at 220nm and ~4.4fW at 260nm, with a responsivity of $\sim 10^{3}$A/W. A measured slow response time of ~20s is attributed to trapping at the AlN/AlGaN growth interface. Potential solutions to reduce the trapping responsible for the increased response times are discussed.

TABLE OF CONTENTS

LIST OF TABLES

LIST OF FIGURES

ix

xiii

CHAPTER 1

INTRODUCTION

Silicon Carbide (SiC) and Gallium Nitride (GaN) based electronic and optoelectronic devices have been extensively studied for their applications in high voltage, high temperature and harsh radiation environments under which conventional Si devices cannot adequately perform. In particular, SiC's high temperature high power capabilities offer significant economic benefits to industries such as aircraft, power, automotive and energy production etc. In this chapter, the material properties of SiC and GaN, and their advantages compared to conventional semiconductors like silicon will be discussed. Further, various aspects of SiC growth technology including step controlled epitaxy for polytype uniformity, doping control is discussed. In section 1.3, the properties and uses of ultraviolet(UV) radiation will be discussed. Then, the need for UV detection is discussed and this is followed by introduction to wide bandgap(WBG) semiconductors based UV detectors along with their advantages and limitations. At the end of this chapter, the motivation for the present research work to develop visible-blind UV detectors using graphene/SiC devices and solar-blind UV detectors using Aluminum Gallium Nitride(AlGaN) high electron mobility transistor(HEMT) devices is discussed.

1.1 WIDE BANDGAP SEMICONDUCTOR MATERIALS

Since the last two decades, there has been an increasing demand for alternative energy sources to traditional gasoline and diesel due to increasing prices and diminishing supply; and the emissions from these sources is a major concern for environmental safety. Therefore, these days there is a great interest in using renewable energy sources for power generation, and also moving towards electrical and hybrid electrical vehicles. Power electronic devices are key components that play a vital role in the generation-storage-distribution cycle. With the widespread use of electronics in the consumer, industrial, medical and transportation sectors, power devices have a major impact on the economy because they determine the cost and efficiency of the systems. Traditionally Si power devices have been used in power systems, but Si power devices have limitations in their performance regarding the operation temperature, blocking voltage capability and switching frequency (Neudeck, Okojie, & Chen, 2002). Moreover, when operated at high voltages these Si power devices require additional cooling systems making the size of the power electronics bulky and this has become a bottleneck for their use in defense and aircraft applications. These limitations in Si power devices led to the development of WBG power semiconductor devices suitable for efficient, reliable, compact and low-cost power electronic systems (Hudgins, Member, Simin, Santi, & Khan, 2003).

1.2 PROPERTIES OF SiC AND GaN

Silicon Carbide(SiC) is a compound semiconductor that exists in a wide variety of crystal structures with unique physical and chemical properties. The strong chemical bonding between Si and C atoms in this semiconductor material makes it very hard material. It has

2

high chemical inertness and radiation hardness, therefore can perform better than Si in harsh environment conditions.

Among these different crystal structure also known as polytypes, 4H-SiC is more popular. Due to the difference in crystal structures, the band structure of each polytype is different and therefore exhibits different optical and electrical properties. Table 1.1 (Kimoto & Cooper, 2014) (Baliga, 2008) show a comparison of the material properties of the 4H-SiC, 6H-SiC with other semiconductors including narrow bandgap Si, GaAs and WBG GaN and diamond.

Table 1.1 Comparison of properties of different semiconductor materials.

Property	Si	GaAs	6H-SiC	4H-SiC	GaN	Diamond
Bandgap, E_g (eV)	1.12	1.43	3.03	3.26	3.45	5.45
Dielectric Constant, ε_r^1	11.9	13.1	9.66	10.1	9	5.5
Electric Breakdown Field, (MV/cm) (at $N_D=3 \times 10^{16} cm^{-3}$)	300	400	$\perp$: 1.7 $\parallel$: 3.0	$\perp$: 2.2 $\parallel$: 2.8	2000	10000
Electron Mobility, (cm^2/V-s)	1500	8500	$\perp$: 450 $\parallel$: 100	$\perp$: 1020 $\parallel$: 1200	1250	2200
Hole Mobility, (cm^2/Vs)	600	400	100	120	850	850
Intrinsic Carrier Concentration at 300 K, (cm^{-3})	1.45×10^{10}	1.79×10^{6}	1×10^{-6}	5×10^{-9}	1.9×10^{-10}	$\sim 10^{-27}$
Thermal conductivity, (W/cm/K)	1.5	0.46	4.9	4.9	1.3	22
Saturated Electron Drift Velocity, V_{sat} ($\times 10^7 cm/s$)	1	1	1.9	2.2	2.2	2.7

The intrinsic carrier concentration in 4H-SiC is 18 orders less compared to Si, and this causes a significant reduction in dark current in 4H-SiC devices. Further, the thermal conductivity of 4H-SiC is 3 times higher compared to thermal conductivity of Si, and as a result 4H-SiC can be used in high voltage devices without the need for additional cooling parts. Also, the breakdown field is almost 8 times higher in 4H-SiC, therefore significantly reducing the thickness of the device active layers. Low dark current, high thermal conductivity and reduced thickness of the 4H-SiC active layers compared to Si therefore makes 4H-SiC suitable for high temperature operation by using compact size devices. Further, the high saturated electron drift velocity(v_{sat}) of 4H-SiC makes it suitable for high frequency switching.

Another WBG semiconductor material, GaN is a major contender for 4H-SiC in high power and high frequency switching applications. Also, the direct bandgap nature of GaN makes it particularly advantageous to use it in optoelectronic applications. The major advantage of 4H-SiC in comparison with GaN is its high thermal conductivity, which is 3 times higher than the thermal conductivity of GaN. Due to its indirect bandgap, the carriers in SiC have a longer carrier lifetime compared to GaN, yielding longer diffusion lengths. This leads to high base transport factor, and thus high bipolar gain which is key for fabricating bipolar devices suitable for high voltage power devices (Chow et al., 2000).

1.2.1 SiC CRYSTAL STRUCTURE AND POLYTYPES

SiC is a compound semiconductor consisting of 50% Silicon and 50% Carbon atoms in its crystal lattice. Each Si atom is covalently bonded by sp^3 hybridization to four C atoms tetrahedrally, and vice versa. The basic building block for SiC crystal structure consists of a bilayer of Si and C atoms as shown in Figure 1.1(a). Further, Ramsdell's notation

4

(Shaffer, 1969) is commonly used to uniquely represent the SiC polytypes by considering the number of Si-C bilayers in the unit cell and the symmetry of the crystal system (C for cubic, H for hexagonal and R for rhombohedral). In Ramsdell's notation, the five most common polytypes of SiC are represented as 2H-SiC, 3C-SiC, 4H-SiC, 6H-SiC and 15R-SiC; where the numbers 2, 3,4,6 and 15 represents the number of bi-layers in the unit cell and the letters C, H and R corresponds to the cubic, hexagonal and rhombohedral crystal symmetry.
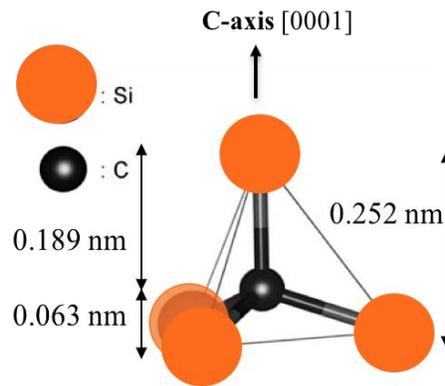
Figure 1.1. Tetrahedral basic unit of SiC.

In the hexagonal crystallographic system, there are four major crystallographic axes namely, a_1, a_2, a_3, and c-axis; where the equivalent axes a_1, a_2, a_3 lie in the same plane at an angle of 120° and c axis is perpendicular to this plane (Figure 1.2(b)).(Kimoto & Cooper, 2014).

5
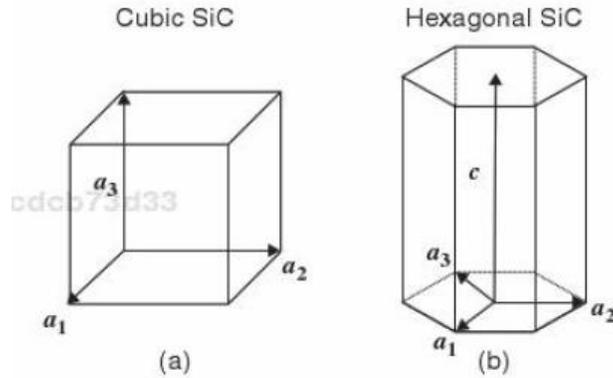
Figure 1.2 Primitive cells and fundamental translational vectors of (a) cubic and (b) hexagonal SiC.

In hcp system, there are three possible occupational sites in the basal plane represented by A, B and C sites (Figure 1.3(a)) (Kimoto & Cooper, 2014).. The tetrahedron or Si-C bilayer can occupy these three different (A, B or C) lattice positions with each layer in the basal plane consists of only one tetrahedral type or position. The variation in the occupied sites, by the Si-C bilayers or tetrahedral, along the c-axis in a hexagonal closed packed (hcp) system brings about different crystal structures, known as polytypes. The different polytypes in SiC therefore can be identified by looking at the occupation sites of Si-C bilayers or tetrahedral along the c-axis direction. As shown in Figure 1.3(b) (Kimoto & Cooper, 2014)., the Si-C bilayers may occupy any of the lattice sites A, B, and C to form close packed structures, where two successive layers cannot occupy the same site. For example, the next layer on top of A layer must occupy either "B" or "C" sites. Similarly, for C layer, the next layer has to occupy either "A" or "B" sites.

Also, as shown in Figure 1.4, the occupation of each lattice position, by the Si-C bilayer or tetrahedral, can possibly occur in two different variants corresponding to rotation around the c-axis by 180°. The twinned variants are denoted by a prime sign as in: A', B'

6

and C'. These two variants can be seen in 4H-SiC and 6H-SiC, in Figure 1.4 (Kimoto, 2016), where the stacking sequence is represented as ABA'C' and BCAC'B'A'.
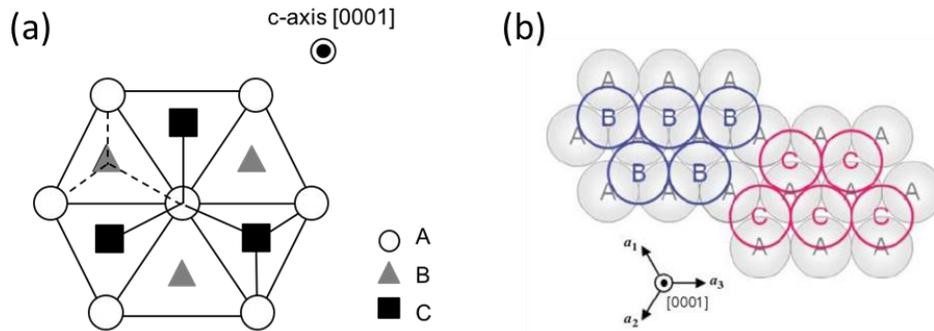
Figure 1.3 (a) ABC sites in hexagonal crystal lattice. (b) Occupational sites (A, B, and C) in the hexagonal closed-packed system in the hard sphere model.

The only cubic (zinc blende) polytype of SiC is 3C-SiC, also referred to as β-SiC. This has a stacking sequence of ABC. All other polytypes are referred to as α-SiC. The 2H-SiC show hexagonal (wurtzite) symmetry with ABAB…stacking order. Except 3C-SiC and 2H-SiC, all other polytypes have crystal structures which are a mixture of zinc-blende (cubic) and wurtzite (hexagonal) structures. 4H-SiC consists of an equal number of cubic and hexagonal bonds, hexagonality=0.5, with a stacking sequence of ABC'B'. 6H-SiC is composed of two-third cubic bonds and one-third hexagonal bonds, hexagonality=0.33, with a stacking sequences of ABCA'C'B'.

The hexagonality of a polytype can be defined as the percentage of hexagonal layers present in the unit cell. The overall symmetry is hexagonal for both polytypes, despite the presence of dominant cubic bonds in each of them. Similarly, 15R-SiC is a rhombohedral crystal structure composed of three-fifth cubic bonds and two-fifth hexagonal bonds.

7
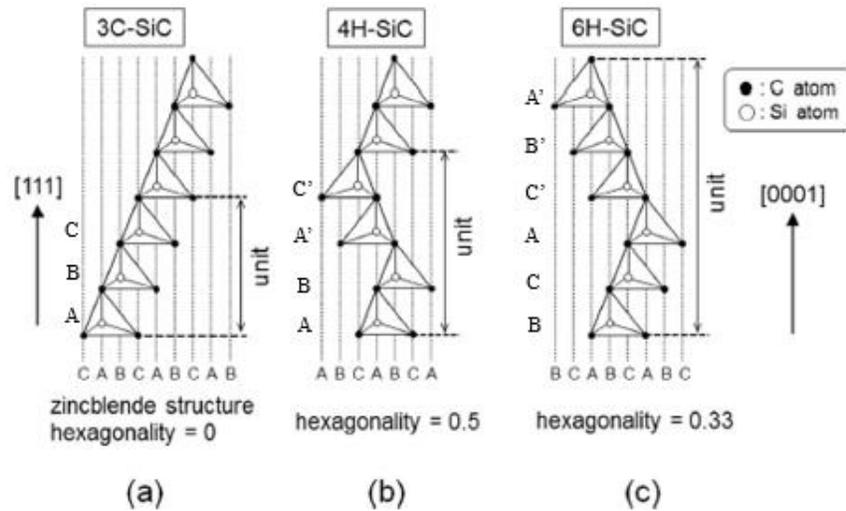
Figure 1.4 Stacking sequence of 3C, 4H and 6H polytypes of SiC.
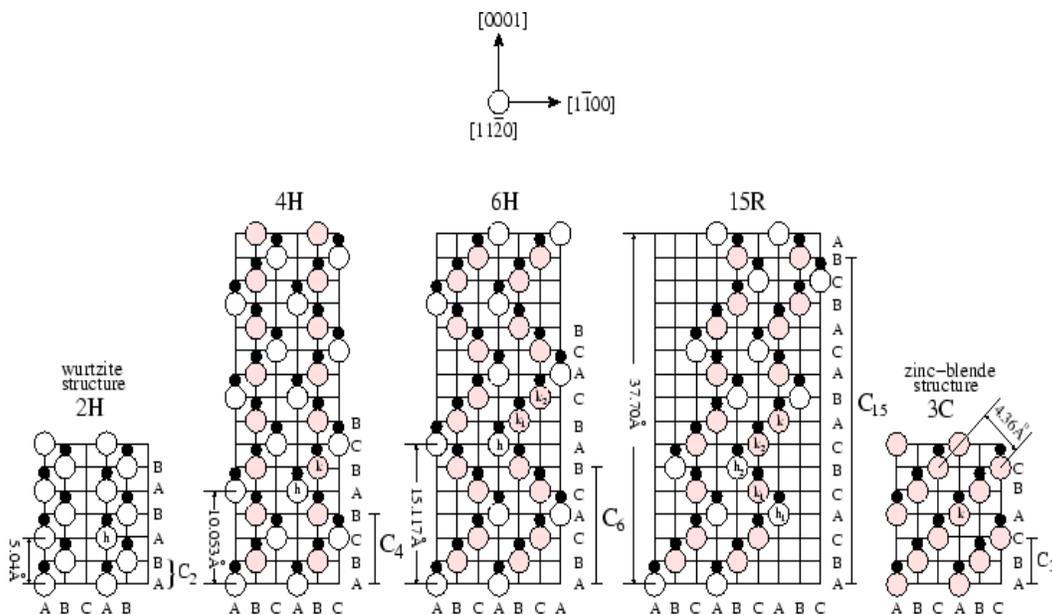
Figure 1.5 Stacking arrangements seen along [11$\bar{2}$0] direction of SiC polytypes. Here Si atoms are represented as open circles and C atoms are represented as filled circles.

As mentioned earlier, the 4H-SiC and 6H-SiC polytypes are not completely cubic or hexagonal but are mixed polytypes and have different hexagonality factors. Figure 1.5 (Ayalew, 2004) shows the stacking arrangement of five different polytypes of SiC. As shown, the silicon atoms labeled "h" or "k" denote Si-C double layers that reside in quasi-

8

hexagonal or quasi-cubic environments with respect to their immediately neighboring above and below bilayers (Ayalew, 2004). In the 4H stacking sequence of ABC'B', all the A sites are the hexagonal "h" sites and all the B and C sites are the cubic "k" sites. Similarly, in the 6H stacking sequence of ABCA'C'B', while all the A sites are the hexagonal "h" sites, there are two kinds of inequivalent quasi-cubic sites for B and C, denoted "k_1" and "k_2"sites, respectively (Ayalew, 2004). In Figure 1.5. the [$1\bar{1}00$] direction is often referred to as the p or m-axis and the [$11\bar{2}0$] direction is referred to as a-axis direction.
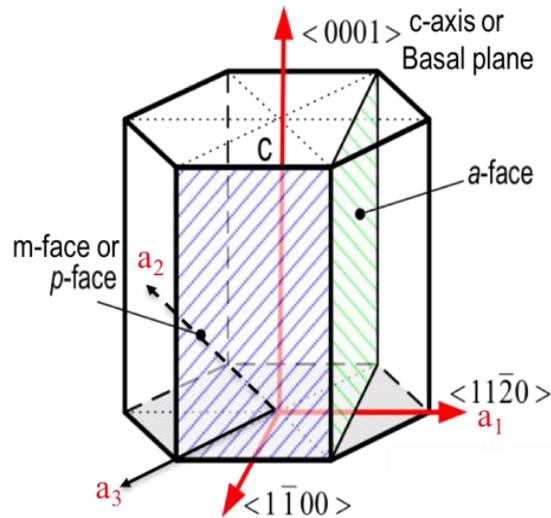
Figure 1.6 Hexagonal unit cell of SiC showing different crystal planes.

As mentioned before, the stacking sequence along the c-axis is different for each SiC polytypes. Therefore, they have different band structures resulting in different optical and electrical properties. Also, the material properties for a given polytype may be different along the c-axis or perpendicular to the c-axis and this is called anisotropy. The degree of anisotropy is measured by the quotient of a parameter value along and perpendicular to the c-axis and anisotropy of 1 is means isotropic material. The use of a particular SiC polytype

9

for a specific application may thus depend on this anisotropy in the material properties. For example, the mobility anisotropy in 6H-SiC is higher compared to 4H-SiC (Table 1.1) which is why 4H-SiC is attractive for vertical power devices. Similarly, the crystal growth is different on different planes (Figure 1.6) for growth rates and polytype replication (homogeneity) due to the variation in atomic packing density along different crystal directions.

1.2.2 EPITAXIAL GROWTH OF SILICON CARBIDE

It is important to grow high quality 4H-SiC epitaxial layers to exploit the exceptional material properties of 4H-SiC (Table 1.1) for fabricating high power and high voltage devices. The important aspects related to SiC epitaxial growth development are achieving polytype uniformity, wide range doping control, minimizing/eliminating the defects. Before discussing these aspects, the CVD growth technique used for SiC epi-layer growth is described here briefly.

Homo-epitaxial growth of SiC, growth of same polytype SiC epilayers as SiC substrates, can be done in three different techniques: liquid phase epitaxy(LPE), vapor phase epitaxy(VPE) and vapor-liquid-solid epitaxy(VLS). The vapor phase epitaxy can be further divided into chemical vapor deposition(CVD), sublimation epitaxy, and high temperature CVD(HTCVD).

Among these different techniques, CVD (Wijesundara & Azevedo, 2011) has shown considerable success and is widely used in industries. In CVD growth of SiC, carbon- and silicon-containing gaseous compounds are transported to a heated SiC substrate, typically above 1200°C, where the homo-epitaxial growth of SiC takes place

10

through a surface-induced chemical reaction. The actual growth process, when the growth reactor reaches the desired vacuum and temperature conditions, typically 1600°C and 300 Torr, is done in two steps: The first step is in-situ etching of SiC, and its purpose is to remove any subsurface damage and also to obtain the regular step structures. The second step is the actual growth step where the precursor and carrier gases are introduced into the growth reactor.

In SiC epitaxial growth using CVD technique, typically, propane(C_3H_8) is used as carbon precursor. Whereas for Si dopants, various gas precursors are available such as silane (SiH_4), dichlorosilane(DCS) (SiH_2Cl_2), tetrafluorosilane (TFS) (SiF_4). Silane has been successfully used as a Si precursor with high growth rates. But the high grow rates are achieved by using high gas flow rates causing homogenous nucleation in the gas phase due to high partial pressure of the precursor gases, thus results in poor surface quality (Pedersen et al., 2012).

Later, Chloride based precursors such as dichlorosilane(DCS), tetrachlorosilane($SiCl_4$) have been used to grow SiC epilayers by suppressing the Si droplet formation (Pedersen et al., 2012). Recently, high quality SiC epilayer growth is reported, by eliminating the Si droplet formation and suppress parasitic deposition, by using TFS gas precursor (Tawhid Rana, 2013). Parasitic deposition can occur, even at temperatures lower than growth temperature 1600°C, on the reactor walls due to dissociation of precursor gas molecule while the gas is flowing towards the sample surface and this causes depletion of precursor gases for actual growth and also necessitates the frequent replacement of reactor parts. The difference in the parasitic deposition for different precursor gases can be explained by considering the bond dissociation energy of the precursor molecules. The

11

bond dissociation energy for Si-F is 565 kJ/mole, which is much higher than the bond dissociation energy of Si-H (318 kJ/mole), Si-Cl (381 kJ/mole) etc., (T. Rana, Chandrashekhar, & Sudarshan, 2012). Therefore, the dissociation of TFS molecule, in a CVD growth reactor, is expected to occur much closer to the substrate surface, i.e. at the growth temperature, in comparison with silane and DCS. Additionally, TFS can also be used for growing graphene on SiC epilayers as will be discussed in chapter 2. In this present research work, TFS and propane gas precursors diluted are used to grow SiC epilayers, and these epilayers are later used as active layer for fabricating the SiC UV detectors. The details for the growth recipe and operation of the CVD reactor, for growing high quality SiC epilayers used in this work (chapters 2,3 and 4), are discussed in detail elsewhere (Tawhid Rana, 2013).

As mentioned before, controlling the polytype uniformity, doping type and density over a wide range, and reduction of defect density are key considerations for the development of SiC epitaxy.

Polytype uniformity

The polytype uniformity in SiC epitaxial growth is achieved by using a technique called step-controlled epitaxy (Matsunami & Kimoto, 1997). In this method, the epilayers use the step features on the off-axis substrates as a growth template, and therefore can be grown with high polytype uniformity.

As shown in Figure 1.7 (Kimoto & Cooper, 2014)., in case of on-axis {0001} substrates, the step density is very low, and therefore, large {0001} terraces exist The temperature is the key parameter affecting the polytype of the grown epilayers. As a result, growth of 3C-SiC may occur initially at low temperatures through two-dimensional

12

nucleation, In case of off-axis substrates, however, the step density is very high and terrace width is small. In this case (see Figure 1.7), the adatoms move towards the steps and kinks which determine the unique lattice sites, to grow laterally replicating the step feature of the off-axis substrate. The growth kinetics of SiC epitaxial growth is explained by Ellison (Ellison, 1999). Although step controlled epitaxy on off-axis substrates helps in obtaining epilayers with better polytype uniformity, the use of off-axis substrates has two major drawbacks in the form of material wastage and formation of BPD's (Kimoto & Cooper, 2014).in the epitaxial layers (see Table 1.1)
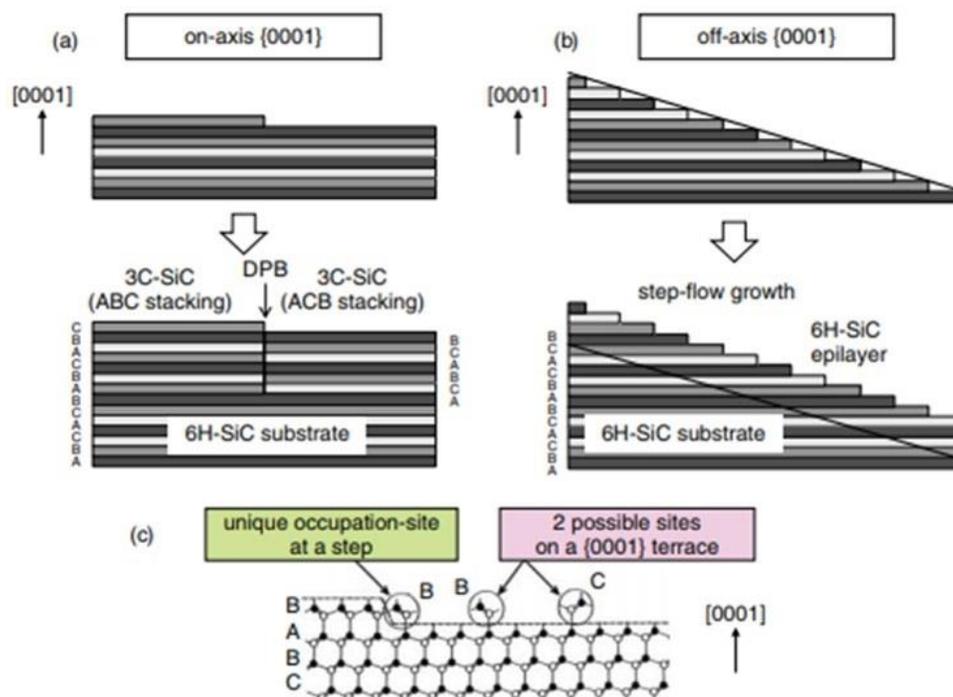
Figure 1.7 Schematic illustration of growth modes and stacking sequences of SiC layers grown on (a) on-axis 6H-SiC(0001) and (b) off-axis 6H-SiC(0001). (c) Bond configuration near an atomic step and on the (0001) terrace. (DPB: Double-Positioning Boundary).

Doping control

The dopants used to control the conductivity type (n or p) in SiC are believed to occupy specific sites, specifically nitrogen occupies the carbon site while aluminum occupies the

silicon site of the SiC lattice. The doping type and density of epitaxial SiC epilayers can be controlled by varying the gas flow ratio of C and Si precursors used during the CVD growth process. Under Si-rich (low C/Si ratio) conditions, the epilayers show n-type conductivity. Similarly, under C-rich (high C/Si ratio) conditions, the resultant epilayers show p-type conductivity. This difference in doping due to change in C/Si is ratio, key to achieve wide range of doping densities in a controlled manner, is explained by a concept called site-competition epitaxy (Larkin, Neudeck, Powell, & Matus, 1994).

According to the theory of site-competition epitaxy: there is a competition between nitrogen and carbon atoms to occupy carbon sites; and aluminum, boron and silicon atoms to occupy Si sites. As a consequence, under Si-rich (low C/Si ratio) conditions, the low carbon atom concentration on the growing surface promotes nitrogen incorporation and results in n-type doping. Similarly, the low Si atom coverage on the growing surface under C-rich (high C/Si ratio) conditions promotes incorporation of Al or B and results in p-type doping.

Defects in SiC

It is important to study the defects formed in SiC epilayers, extended defects or process induced defects, as they are detrimental for the performance of SiC devices. Some important defects in SiC epitaxy include micropipes(MP), threading screw dislocations (TSD), threading edge dislocations (TED), the basal plane dislocations (BPD) and stacking faults (SF) (N. Zhang, 2011). Figure 1.8 (Kimoto, 2015).shows the different types of defects observed in SiC epilayer. Some of these defects can be converetd into less harmful TSD and TED during SiC epitaxial growth. Various methods such as alkaline KOH etching

14
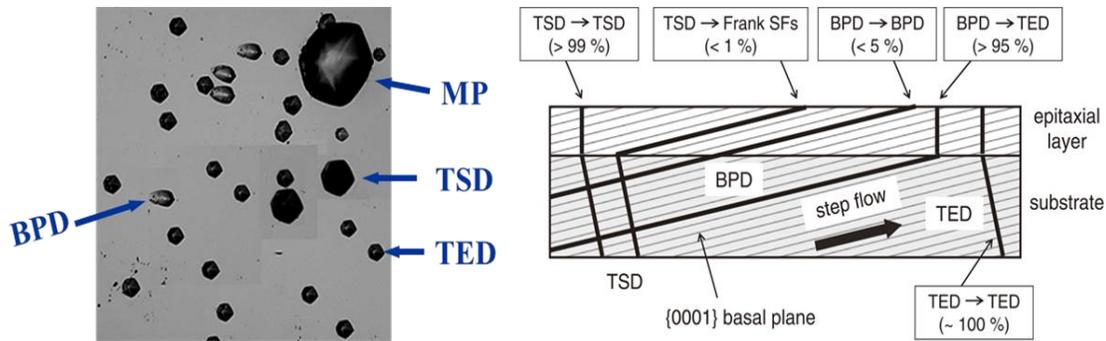
Figure 1.8 (a) Nomarski image of KOH etched epitaxial SiC layer showing various crystal defects in SiC. (b) Replication and conversion of dislocations in SiC epitaxial layers grown on off-axis substrate.

Table 1.2 Current understanding of effects of extended defects on SiC device performance and reliability.

Defect type \ Device type	SBD	MOSFET, JFET	PiN, BJT, Thyristor, IGBT
TSD (without pit)	No	No[a]	No[a], but causes local reduction of carrier lifetime
TED	No	No[a]	No[a], but causes local reduction of carrier lifetime
BPD (including interface dislocation, half-loop array)	No	No[a], but can cause degradation of body diode	Bipolar degradation (increase of on-resistance and leakage current)
In-grown SF	V_B reduction (20-50%)	V_B reduction (20-50%)	V_B reduction (20-50%)
Carrot, triangular defects	V_B reduction (30-70%)	V_B reduction (30-70%)	V_B reduction (30-70%)
Down-fall	V_B reduction (50-90%)	V_B reduction (50-90%)	V_B reduction (50-90%)

a) Impacts on gate-oxide reliability are still under consideration.
SBD: Schottky barrier diode, MOSFET: Metal oxide field effect transistor, JFET: Junction field effect transistor, PiN: PiN diode, BJT: Bipolar junction transistor, IGBT: Insulated gate bipolar transistor, V_B: breakdown voltage

15

have been reported (Z. Zhang & Sudarshan, 2005) that can effectively minimize the defect denisty in the SiC epilayers. Among these defects, BPDs and SF's are considered to be device killing defects (N. Zhang, 2011). Table 1.2 (Kimoto, 2015). summarizes the effect of various crystal defects on performance and reliability of SiC devices.

1.3 ULTRAVIOLET(UV) DETECTORS

Photodetectors are the devices that can generate an output signal in response to incident light. UV detectors are a special category of photodetectors which can produce an output signal when UV light is incident on them. The electromagnetic spectrum is divided into different spectral regions depending on the energy (or wavelength) of the radiation. Among these different spectral regions, the UV radiation which is spread from 10nm-400nm is particularly important due to various applications. UV light is produced by sun and also various artificial sources such as electric arcs, mercury vapor lamps etc. UV light has important applications including disinfection for viruses and bacteria, hygiene and infection control, UV fluorescence spectroscopy, sterilizing surgical equipment and air quality in operating rooms. A part of UV light emitted from sun gets absorbed (10-290nm) in different regions of the atmosphere including ozone, and only the radiation with wavelength above 290nm reaches the earth's surface (see Figure 1.9 (a)).

The UV radiation spectrum is further divided into four regions depending on the wavelength.

UV-A(320nm-400nm): This radiation stimulates photosynthesis, and is also responsible for synthesis of some vitamins and basic biochemical compounds. Over exposure may lead to ageing.

16

UV-B(280nm-320nm): This radiation consists of about 10% of the total UV radiation power density from the sun (i.e. 290nm-400nm) reaching the earth's surface (Figure 1.9(a)). UV-B exposure is dangerous for human beings as it can cause cancer, cataracts and burns etc. It has some health benefits such as it induces skin to synthesize vitamin D. The figure 1.9 (b) shows the optimal exposure limits for UV radiation.

UV-C(200nm-280nnm): This part of UV radiation emitted from sun is mostly absorbed by ozone layer. UV-C radiation is useful for applications such as disinfecting water, medical equipment etc.

Vacuum UV(10nm-200nm): This radiation is strongly absorbed by molecular oxygen present in air. One major application of this part of UV radiation is in extreme UV lithography (193nm) for integrated circuit (IC) manufacturing.

Figure 1.9(b), shows the safe exposure limits (maximum) corresponding to different UV wavelength bands (H. Chen, Liu, Hu, Al-Ghamdi, & Fang, 2015).
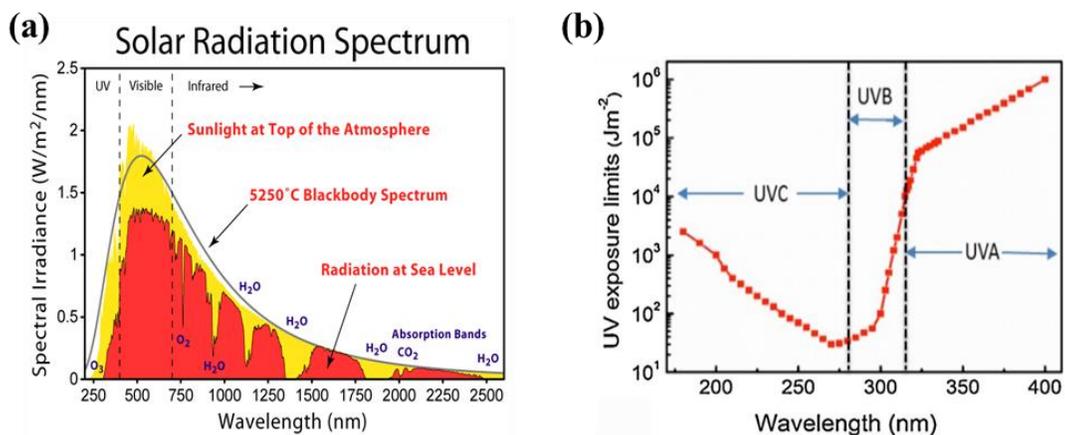
Figure 1.9 (a) Solar radiation spectrum. (b) A graph showing the maximum UV exposure limits at different UV wavelengths for safety purposes.

Further, the detection of the UV light is also important for various applications such as in defense for plume detection, flame sensing, and also as biological and chemical sensors (M. Razeghi & Rogalski, 1996). For instance, in flame sensing applications, the UV detectors can detect the UV radiation emitted at the time of ignition. The UV detectors can be categorized as either solar-blind or visible-blind UV detectors based on the long wavelength absorption cutoff($\lambda_{\text{cut-off}}$) of these detectors. Here the term "blind" refers to insensitiveness of the detector to photons of particular wavelengths. Solar-blind UV detectors are those UV detectors with $\lambda_{\text{cut-off}}$ below 280nm and visible-blind UV detectors are the UV detectors with $\lambda_{\text{cut-off}}$ below 400nm.

In general, the **photodetectors** are classified into two categories: photon detectors and thermal detectors (see figure 1.10) (M. Razeghi & Rogalski, 1996) depending on how they operate. In photon detectors an electrical output signal is produced as a consequence of absorption of incident light by the detector material. In thermal detectors, on the other hand, the incident photons cause a change in the temperature of the detector. These temperature changes of the detector are studied as a function of changes in some temperature dependent material property for e.g., such as changes in resistance with temperature.

Photoelectric detectors are commonly used UV detectors among different UV photon detectors.

Photoconductive detectors: In these detectors, the conductivity of the semiconductor material changes due to photogenerated current resulted from the absorption of the incoming photons. The conductivity changes as a function of intensity of incident light.

18

Photovoltaic detectors: In these devices, a voltage is generated under optical illumination. These are typically junction devices such as pn diode, pin diode, Schottky diode etc. where each region has a majority carrier type contributing to the conductivity.

Photo-emissive detectors: These detectors use photoelectric effect for their operation. When photons of sufficient energy strike the surface of these detectors, electrons will be emitted and are collected in the external circuit.
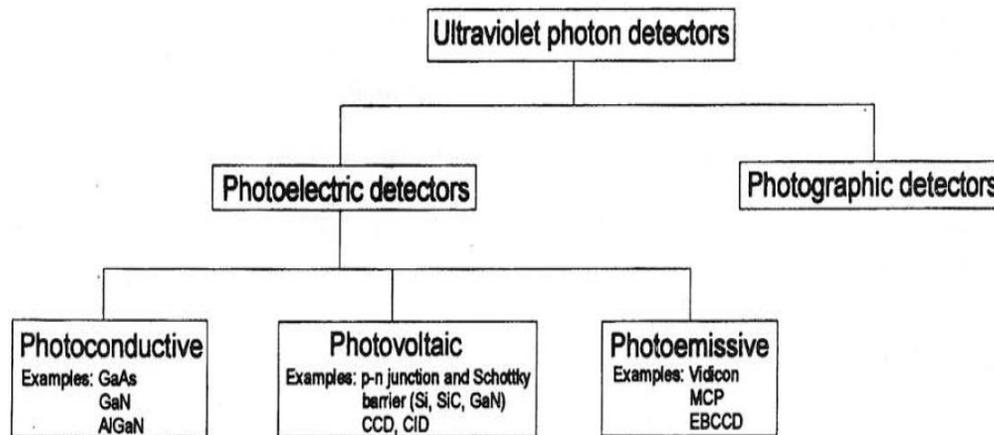
Figure 1.10 Classification of Ultraviolet photon detectors.

In addition to these basic types of photodetectors, there also exists phototransistors, which are similar to photodiodes with an additional gain resulting from the transistor action. These are particularly useful for detecting weak optical signals. Refer to (M. Razeghi & Rogalski, 1996), for more details on the basic operation principles, advantages and disadvantages of various kinds of photodetectors.

The basic performance metrics that are used to characterize and compare the performance of different photodetectors are described below.

19

Responsivity(*R*):

The responsivity(*R*) is defined as the number of amperes of photocurrent generated per watt of incident optical power. It is related to quantum efficiency(η) and gain(g) of the device as given by the equation:

$$R = \frac{q\lambda}{hc}\eta g \qquad (1.1)$$

where λ is the incident light wavelength, q is the electron charge, h is the Planck constant, c is speed of light. The quantum efficiency (η) can be defined as the ratio of flux of e-h pairs generated to the flux of photons incident on the photodetector.

Response time or Speed:

The response time(τ) or speed is the time required for an optical detector to respond to optical input. It is defined as the time taken by the photocurrent to reach 90% of its maximum value from 10% in steady state under illumination. The response time or speed values are therefore can be measured experimentally from the ON or OFF transient responses. Additionally, the bandwidth(B) of a photodetector is then calculated from the response time(τ) using the equation:

$$B = \frac{1}{2\pi\tau} \qquad (1.2)$$

Noise Equivalent Power(NEP) and specific detectivity(D*)

The ability of a photodetector to detect the incident radiation is limited by the noise generated by both incoming photons and also the current fluctuations generated by the detector itself. For photodetectors, in general, there are four main sources for noise, which includes thermal (or Johnson) noise, shot noise, 1/f (or flicker) noise and photon noise. Among these, photon noise or radiation noise is considered as external noise whereas

20

thermal noise, shot noise and flicker noise are considered as internal noises of the detector. Later, in chapters 4 and 5 of this dissertation, characterization of these internal noise parameters in our UV photodetector devices will be discussed.

Thermal noise is present in any resistive material, and noise current corresponding to thermal noise is given by the equation:

$$\langle i^2_{thermal} \rangle = \frac{4kT}{R} B \qquad \text{(Eq.1.3)}$$

where k is the Boltzmann's constant, T is absolute temperature, B is the bandwidth of the measurement system and R is the resistance of the material. This noise has its origin in electron density fluctuations due to temperature in a conducting material. Therefore, to reduce this thermal noise, the photodetectors need to be operated at low temperatures.

The shot noise is associated with the random nature, typically follows Poisson's distribution, of generation and collection of charge carriers in the photodetector. The shot noise in photodetectors is given by the equation:

$$\langle i^2_{shot} \rangle = 2eI_{dark}B \qquad \text{(Eq.1.4)}$$

Similarly, shot noise under illumination is given by the equation:

$$\langle i^2_{shot} \rangle = 2eI_{photo}B \qquad \text{(Eq.1.5)}$$

where e is the electron charge, I_{dark} is the dark current, I_{photo} is the photocurrent and B is photodetector bandwidth. Therefore, it is important to reduce the dark current in photodetectors to minimize the shot noise in photodetectors. Typically, the UV detectors based on WBG materials such as SiC and GaN have low shot noise compared to narrow

bandgap materials such as Si due to very low intrinsic carrier concentration(n_i) in WBG materials leading to low dark currents.

In case of flicker noise or 1/f noise, the noise current is inversely proportional to frequency (or bandwidth) of the photodetector. The origin for this flicker noise is not well understood and is still a debatable topic in the scientific community. Two popular models explained the flicker noise current are proposed by Hooge and McWhoretel. Hooge's model (Hooge, 1994) explains the 1/f noise by considering the fluctuations in the mobility of free carriers, and McWhoretel's model (McWhorter, 1957) uses fluctuations in the carrier density to explain the flicker noise. In general, $1/f$ noise appears to be associated with the presence of potential barriers at the contacts, surface trapping phenomena, and surface leakage currents. To minimize the effect of 1/f noise contribution, the photodetectors with high speed (<µs) are good for practical applications as these devices can operate at frequencies >100Hz

Typically, photodetectors differ in their operation principle, gain and readout electronics. Therefore, the noise in photodetectors cannot be compared directly by comparing their noise currents. For this purpose, we use a parameter called noise equivalent power(NEP) to compare the performance of the photodetectors. The NEP of a photodetector is the minimum detectable optical power, and is defined as the ratio of the noise current to responsivity given by the equation:

$$NEP = \frac{\sqrt{\langle i_n^2 \rangle}}{R} \qquad \text{(Eq.1.6)}$$

where $\langle i_n^2 \rangle$ is the total rms noise current and R is the responsivity.

Specific detectivity is another parameter that is used to compare the noise performance of photodetector devices with different areas. It is calculated by using the equation:

$$D^* = \frac{\sqrt{A \times B}}{NEP} \qquad \qquad \text{(Eq.1.7)}$$

where A is the active area of the photodetector, B is the detector bandwidth and NEP is the noise equivalent power.

1.4 WIDE BANDGAP SEMICONDUCTOR UV DETECTORS

Photomultiplier tubes (PMTs) have been used for a long time for UV detection since they offer high responsivities. But these PMT's are fragile, need large power supplies which makes these detector systems bulky and expensive, and thus prohibits their use in practical applications. Later solid-state UV detectors based on semiconductors, specifically Si, gained popularity due to their low weight and reliability. Although Si based UV detectors became popular for commercial applications, they are sensitive to visible light, and therefore required to be used with optical filters that block the visible light (Manijeh Razeghi, 2002). Also, the narrow bandgap $Si(E_g=1.1eV)$ UV detectors have disadvantages such as ageing, high dark current and also not suitable for operation in high temperature environments. Therefore, UV photodetectors based on wide bandgap semiconductors like 4H-SiC (E_g=3.26eV), GaN(E_g=3.4eV) are better choice for visible-blind UV detection, and can be operated in high temperature and harsh environment conditions due to high radiation and chemical hardness (E Monroy, Omnes, & Calle, 2003), (Wright & Horsfall, 2007) . A variety of devices structure such as pn diode, pin diode, Schottky diode, MSM diode, phototransistor etc. based on wide bandgap SiC and GaN semiconductor materials have

23

been reported in the literature for UV detection applications (E Monroy, Omn s, & Calle, 2003)

The $Al_xGa_{1-x}N$ material system has a direct bandgap that can be varied from E_g=3.4eV ($\lambda_{cut-off}$=365nm) to E_g=6.2eV ($\lambda_{cut-off}$= 200nm), by varying the Al mole fraction from x=0 to 1 (Yoshida, Misawa, & Gonda, 1982). As a result, as shown in Figure 1.11(Walker et al., 1996), the long wavelength absorption cutoff ($\lambda_{cut-off}$) in these material systems can be tuned between either 365nm and 200nm suitable for visible blind and solar-blind UV detection. The UV detectors fabricated using ultra-wide bandgap (UWBG) $Al_xGa_{1-x}N$ (x>0.4, i.e. E_g>4.3eV, $\lambda_{cut-off}$<290nm) become a good choice for solar-blind UV detector applications.
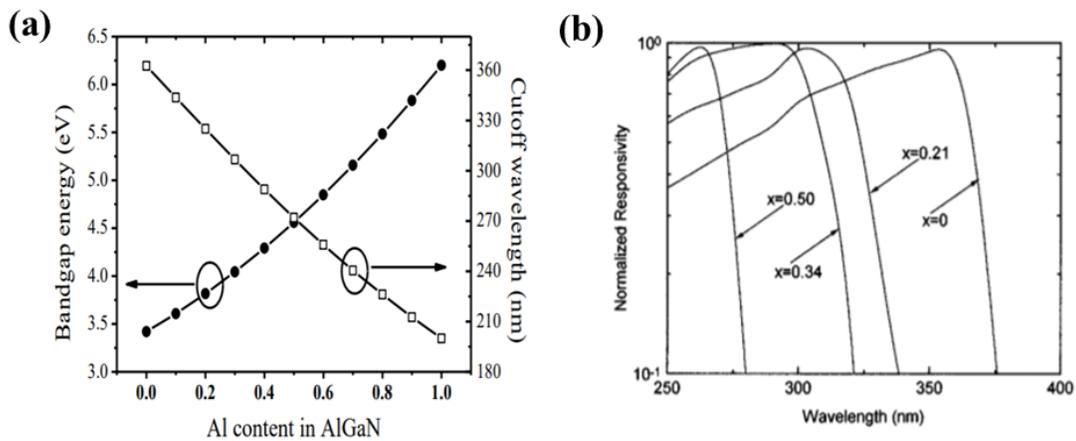
Figure 1.11 (a) Bandgap and cutoff wavelength of $Al_xGa_{1-x}N$ dependent on Al mole fraction(x). (b)Normalized spectral response of $Al_xGa_{1-x}N$ photoconductors with different Al mole fraction (x).

For a long time, the major limitation for SiC and GaN based UV detectors is their low UV responsivities due to reflection/absorption losses caused by metal electrodes used in these detectors. To solve this problem, several groups have used transparent metal

electrodes such as Ni/Au, Ti, Ti/W and ITO, for enhanced photo response in the UV region (E Monroy, Omnes, et al., 2003). These transparent metal electrodes although show improved performance still suffer from low UV transmittance which is under 80% (see table 1.2). More recently, few groups have successfully demonstrated SiC and GaN UV detectors by using high conductivity graphene as an electrode material. The high conductivity graphene is shown to be highly transmittance and negligible absorption in the UV wavelength regime, with >90% transmittance and 0.6% absorption per monolayer, (i.e.~0.3nm) from 200nm-400nm.

Table 1.3 Comparison of performance of different UV detectors by using different metal electrodes.

S.No.	Detector type	Electrode material	Transmittance	Responsivity(R)
1	4H-SiC Schottky (A. Sciuto et al., 2007)	Ni_2S	N/A.	160mA/w at 254nm
2	GaN MSM (Wang et al., 2006)	10nm thick TiW	75.1% at 300nm	~0.15A/W at 300nm
3	4H-SiC MSM (Yan Kuin Su et al., 2002)	ITO	>40% at 300nm	N/A.
4	GaN MSM (Y. K. Su et al., 2002)	ITO	>90%	~7A/W at 360nm
5	4H-SiC MSM (Kusdemir, Ozkendir, Firat, & Celebi, 2015)	Graphene	>90% (200-400nm)	~10mA/W at 254nm

25

Table 1.3 compares the optical transmittances of various metal contact electrodes used in SiC and GaN UV detectors. Graphene forms a Schottky junction with semiconductors such as Si, GaAs, 4H-SiC and GaN (Tongay, Schumann, & Hebard, 2009), (Tongay et al., 2012). Also, Schottky contact based UV detectors show superior photo-response compared to p-i-n UV detectors, in short UV wavelength regime, due to charge carrier generation near the strong built-in electric fields created near the top surface (Antonella Sciuto, Roccaforte, Franco, Raineri, & Bonanno, 2006). In this present research work, our primary goal is to avoid the losses caused by metal electrodes in conventional detectors, by using natively grown graphene as a transparent conducting electrode to improve the quantum efficiency and therefore the responsivity of 4H-SiC UV detectors (chapter 3and chapter 4).

On the other hand, $Al_xGa_{1-x}N$ detectors as mentioned before, are suitable for solar-blind DUV detection. Recently, high Al (x=0.65) content $Al_xGa_{1-x}N$ based MQW detectors (Sakib Muhtadi, Hwang, Coleman, Lunev, et al., 2017) and MESFET detectors (JEM, under review) with very high responsivity in DUV regime, are demonstrated at USC. Also, a high Al content(x=0.65) $Al_xGa_{1-x}N$ channel HEMT devices with high current handling capability suitable for high temperature operation are demonstrated (Sakib Muhtadi, Hwang, Coleman, Asif, et al., 2017). In this present work, these $Al_xGa_{1-x}N$ channel (x=0.65) based HEMT device structure are studied (chapter-5) for their application as a high responsivity solar-blind UV detector for DUV detection. Finally, the major goal for the present research work is to develop high performance visible blind ($\lambda_{cut-off}$<400nm) and solar-blind ($\lambda_{cut-off}$<280nm) UV detectors i.e. UV detectors with high responsivity, high speed and high detectivity.

26

CHAPTER 2

EPITAXIAL GRAPHENE GROWTH ON SIC

As explained in chapter 1, graphene can be used as a transparent electrode for improving the responsivities in SiC UV detectors. In this chapter, a brief introduction to graphene structure, material properties and applications is presented. Later, two major techniques for graphene growth, thermal sublimation of SiC and selective etching of Si from SiC using Tetrafluorosilane(TFS), developed at USC, will be discussed in detail. The motivation for this chapter is to provide a comparison of the EG/SiC junction properties grown using the abovementioned techniques, as it is important to understand the device characteristics of EG/SiC Schottky junction based phototransistors as will be discussed later in chapter 3 and chapter 4.

2.1 PROPERTIES AND APPLICATIONS OF GRAPHENE

Graphene is a single sheet of sp^2-bonded carbon atoms arranged in a honeycomb lattice with a lattice constant of 0.14nm. It is the basic building block of well-known carbon materials such as graphite, fullerene and carbon nanotubes (Figure 2.1). In a single layer graphene, the unit cell (one hexagon) consists of two carbon atoms (each atom shared by 3 neighboring unit cells)—the A and B sub lattices (Figure 2.2(a)). The band structure of graphene exhibits two bands intersecting at two inequivalent points, K and K', in the reciprocal space (see Figure 2.2) (Neto, Guinea, Peres, Novoselov, & Geim, 2009).

27
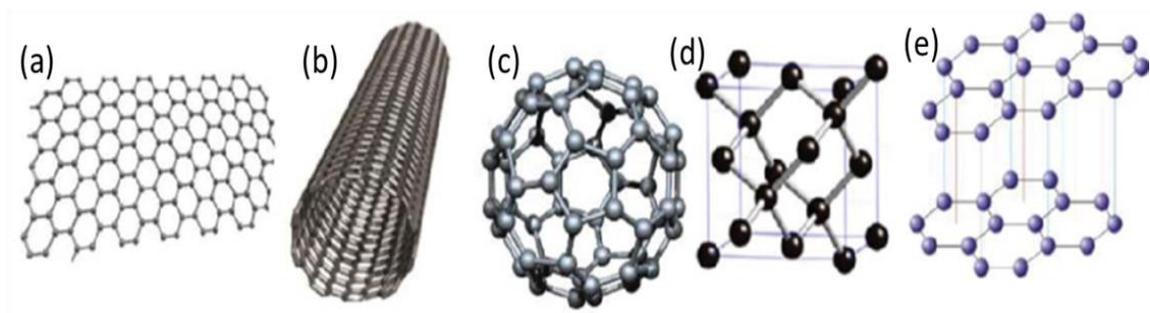
Figure 2.1 Structures of few important allotropes of carbon (a)graphene, (b)nanotube, (c)fullerene, (d)Diamond and (e)graphite.
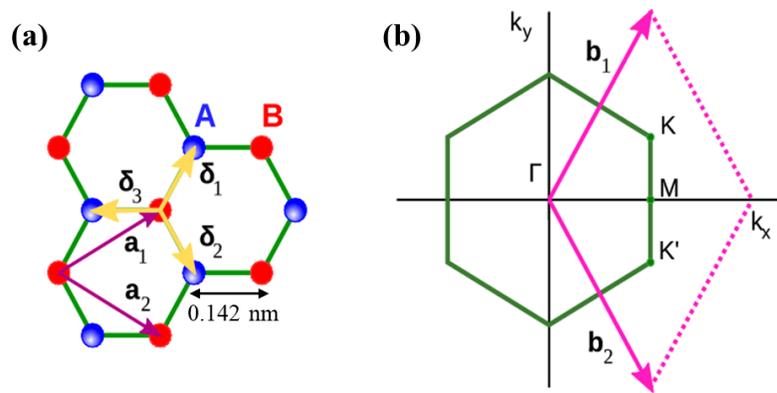
Figure 2.2 (a) Honeycomb lattice structure of graphene. The vectors δ_1, δ_2, and δ_3 are the vectors connect the nearest neighbor atoms separated by a distance a=0.14nm. The vectors a_1, a_2 are the basis vectors of a triangular bravais lattice. (b) The Brillouin zone of graphene with reciprocal lattice vectors b_1 and b_2. The points **K** and **K'** corresponds to the location of Dirac cones.

The unique physical, chemical properties of graphene are determined by its 2D crystalline nature and the resulting band structure. The dispersion relation or band structure can be obtained by considering the interaction of carbon atoms to its nearest and next nearest neighbor carbon atoms in the crystal. As seen in Figure 2.2(a), each carbon atom has 3 nearest and 6 next nearest neighbors and the interactions between these atoms defines the energy dispersion relationship. The energy dispersion relation is given as:

$$E(k) = \pm t\sqrt{3 + 2\cos(\sqrt{3}k_y a) + 4\cos\left(\frac{\sqrt{3}}{2}k_y a\right)\cos\left(\frac{3}{z}k_x a\right)} \quad (2.1)$$

28

,where k is the reciprocal lattice vector and t represents the interaction energy between the neighboring atoms. The interaction energy($t^{'}$) between the next nearest neighboring atoms is neglected in obtaining the above relation.

The positive term corresponds to the conduction band and the negative term corresponds to the valence band as shown in Figure 2.3(a) (Neto et al., 2009). Near the zero-energy point, also called as Dirac point, the dispersion relationship appears as linear (blown-up diagram in Figure 2.3(a)). It is important here to note that semiconductor materials typically show parabolic dispersion relationship. Further, the valence and conduction bands meet at such 6 Dirac points K and K$^{'}$ in the reciprocal lattice as shown in Figure 2.3(b) (Freitag, 2008).

As shown in Figure 2.2(b), the two points K and K' are referred to as the Dirac points as the electronic dispersion resembles that of relativistic Dirac electrons at these two points. The **K** and **K'** points are defined as:

$$\boldsymbol{K} = \left(\frac{2\pi}{3a}, \frac{2\pi}{3\sqrt{3}a}\right); \boldsymbol{K'} = \left(\frac{2\pi}{3a}, -\frac{2\pi}{3\sqrt{3}a}\right) \tag{2.2}$$

The linear dispersion relationship near these K and K$^{'}$ points and within ± 1 eV of the Dirac point is given by:

$$E(k) = \pm h v_F |k| = v_F \sqrt{k_x^2 + k_y^2} \tag{2.3}$$

,here v_F is called the Fermi velocity and is given by the equation:

$$v_F = \frac{3at}{2\hbar} \approx 0.9 \text{ x } 10^6 \text{ m/s} \tag{2.4}$$

Due to this linear dispersion relationship, the electrons and holes in graphene move with v_F, and therefore called as Dirac fermions. Since the valence band and conduction band are degenerate at the Dirac points, graphene is considered as zero bandgap semiconductor.

Therefore, opening the band gap in this single layer graphene is important for the realization of semiconductor devices based on graphene.
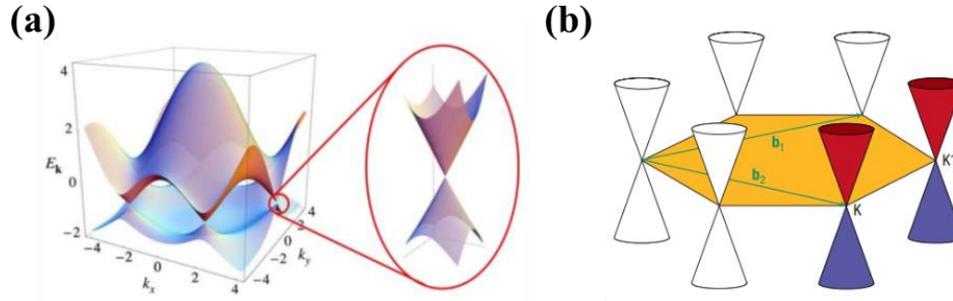
Figure 2.3 (a) Energy bands in monolayer graphene showing the conduction (upper one) and the valence band (lower one). The blown-up diagram shows linear relationship close to Dirac point where conduction band and valance band meet. (b) Low-energy electronic structure of graphene showing 6 Dirac points such points of contact. The vectors **b₁** and **b₂** correspond to the reciprocal lattice vectors and two distinct corners of Brillouin zone are shown as K and K'.

Graphene has exceptional material properties such as high carrier mobility$>2x10^5$ $cm^2V^{-1}s^{-1}$ (Bolotin et al., 2008), high optical transmission$>90\%$ (Bonaccorso, Sun, Hasan, & Ferrari, 2010), very high thermal conductivity $\sim5x10^3$ $Wcm^{-1}K^{-1}$ (Balandin et al., 2008) high Young's modulus 1500GPa (Lee, Wei, Kysar, & Hone, 2008) (for mechanical strength) etc. In addition to its high optical transmission in UV-visible regime, graphene also shows very low 1/f noise and thermal noise (Rumyantsev, Liu, Stillman, Shur, & Balandin, 2010) which makes it suitable for photodetector applications. Another interesting property of graphene is band gap tuning via applied electric field, molecular doping etc. (Singh, Uddin, Sudarshan, & Koley, 2014). Graphene due to its exceptional material properties has wide variety of applications such as in photodetectors, high speed transistors, chemical and biological sensors displays, batteries, hydrogen storage, solar cells etc. Figure 2.4 shows the applications of graphene in various fields (Iyechika, 2010).

30
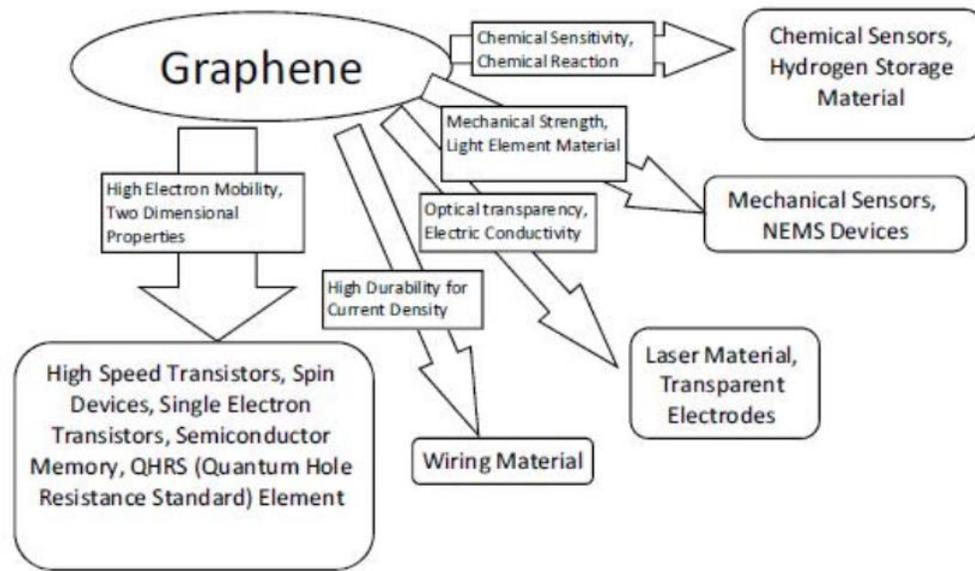
Figure 2.4 Properties of graphene and its applications in various fields.

2.2 GRAPHENE GROWTH TECHNIQUES

The properties of graphene were studied theoretically for the first time P. R. Wallace in 1947 (Wallace, 1947), and he predicted the electronic structure and linear dispersion($E = \hbar k v_F$, v_F is fermi velocity) in graphene. But, AK Geim and K.S. Novoselov, demonstrated the isolation of single layer graphene using mechanical exfoliation technique for the first time in 2004 (Kostya S Novoselov et al., 2004). Graphene is the first 2D crystalline material (i.e. one atom thick) isolated in nature. Since the first demonstration of obtaining single layer graphene by Geim and Novoselov, graphene has attracted much interest due to its unique materials properties and technological applications. Although, high quality graphene is obtained by mechanical exfoliation method, the practical use of this technique is limited as large area graphene growth is not possible which is important for wafer scale manufacturing. Later, many techniques have been developed to grow graphene that includes chemical vapor deposition (Kim et al., 2009), thermal sublimation technique

31

(Emtsev, Speck, Seyller, Ley, & Riley, 2008), reduction of graphene oxide (Pei & Cheng, 2012), liquid phase exfoliation (Blake et al., 2008) etc. Among these techniques, CVD and thermal sublimation became popular as these techniques allow to grow large area graphene suitable for wafer scale manufacturing (K. S. Novoselov et al., 2012).
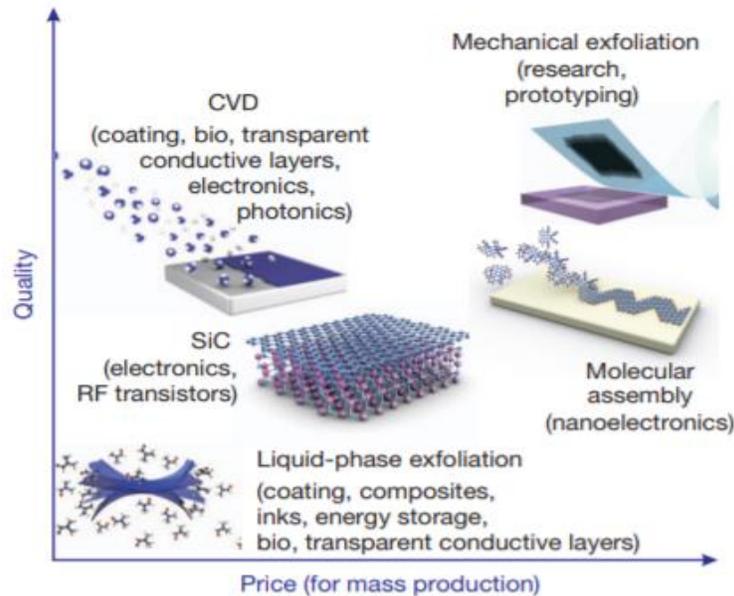
Figure 2.5 Comparison of quality and production costs of graphene grown using different growth methods (K. S. Novoselov et al., 2012).

Several research groups have reported graphene growth by using CVD process, on transition metals such as Ni (Mattevi, Kim, & Chhowalla, 2011), Ir (Coraux, N'Diaye, Busse, & Michely, 2008) and Ru (Sutter, Flege, & Sutter, 2008). For device applications, graphene grown on transition metals in CVD method need to be transferred onto semiconducting substrates. Two popular methods for the transfer of CVD graphene grown on metals is thermal release tape method and PMMA method (G. Deokar, 2015, Carbon). The transfer process of graphene onto semiconductors, however, introduces defects in the transferred graphene layer (Lupina et al., 2015), thus making the CVD transferred graphene

32

inferior for device applications. Therefore, it is important to grow graphene directly on semiconducting substrates such as SiC for mass producing graphene for various device applications, particularly for electronic and optoelectronic device applications. The Figure 2.5 shows the price and the quality of graphene obtained by using different techniques (K. S. Novoselov et al., 2012).

2.3 EPITAXIAL GRAPHENE GROWTH BY THERMAL SUBLIMATION OF SIC

In this technique the SiC substrate is heated to high temperature ~1300-1600°C either in vacuum or inert environment such as Ar. At this high substrate temperature, the Si atoms desorb from the surface as the vapor pressure of Si higher than that of carbon at the surface, and this leads the formation of a C-rich layer on the SiC surface (reaction1 in Table 5.1):

$$SiC(s) \rightarrow Si(g) + C(s) \tag{2.5}$$

The growth process can be divided into three basic steps, (i) Si desorption (ii) C rearrangement by diffusion and (iii) nucleation of C atoms (K. S. Novoselov et al., 2012). Among these three steps, Si desorption is the controlling step for the growth process. The figure below shows the recipe (Biplob K. Daas, 2012) for graphene growth process by using thermal sublimation of SiC in vacuum. The 2-3 ML thick EG obtained using this recipe is used for fabricating EG/SiC phototransistors devices in chapter 3 is grown using this recipe.

33
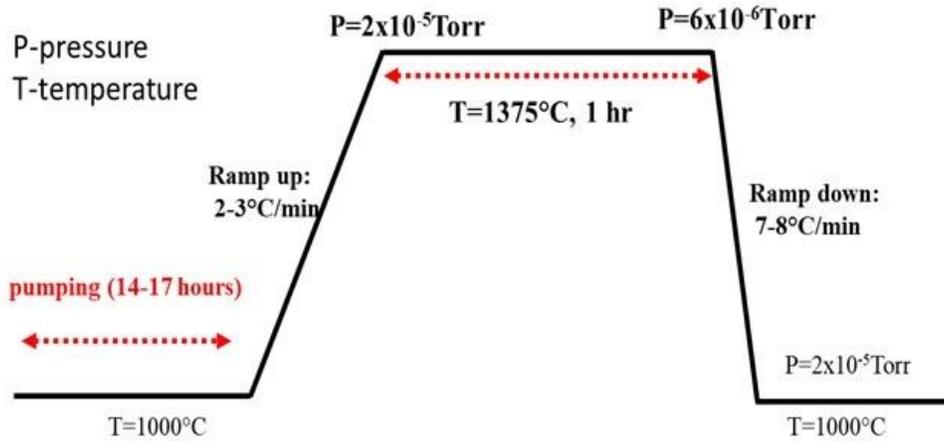
Figure 2.6 Recipe for EG growth using thermal sublimation technique.

When a single crystal graphene layer is formed, growth of subsequent graphene layers is not possible as the out-diffusion of Si atoms through graphene layer is not permitted due to large size of Si atoms when compared to C atoms in the graphene layer at the top (Figure 2.7 (a)) (B. K. Daas et al., 2012). After the first graphene layer is formed at the top, the formation of subsequent graphene layers has to happen by the evaporation or removal of Si atoms from the SiC surface underneath this graphene layer. It is explained (Shetu et al., 2013), by using BCF theory, that Si atoms diffuses laterally through defects and grain boundaries present in the graphene layers already grown at the top (Figure 2.7 (b)) (Shetu et al., 2013). The growth of multi-layer graphene takes place in bottom up scheme.

The EG thickness can be controlled by changing the temperature and time, as well as the choice of SiC substrate orientation (Dresselhaus & Dresselhaus, 2002). The sublimation growth of graphene is studied both on polar (Si-face and C-face) and non-polar faces (a and m planes) of 6H-SiC (Shetu et al., 2013). It was shown that graphene growth on Si-face is slow and is limited to 3-4 ML whereas on C-face the graphene growth is faster

34

with thicknesses >30ML (Shetu et al., 2013) (Luxmi, Srivastava, He, & Feenstra, 2008). Additionally, the surface morphology of graphene layers grown on Si-face is better, as seen by AFM, compared to graphene layers grown on C-face (Luxmi et al., 2008). Therefore, epitaxial graphene growth on SiC is mostly done on Si face.
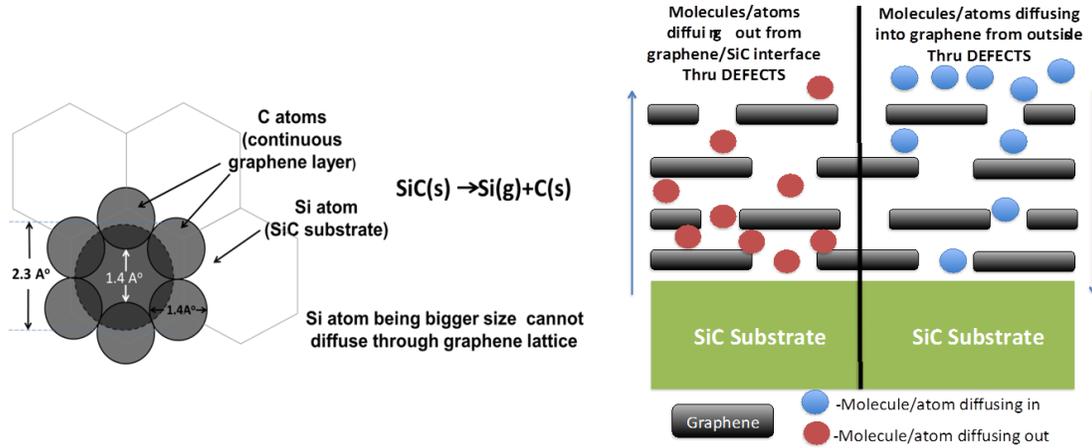
Figure 2.7 (a) The silicon atom has a much larger diameter than the atomic gap in a graphene layer. Si-loss can only occur through defects. (b) Schematic of defects in graphene, and how they mediate molecular in-diffusion for doping and Si-adatom out-diffusion for growth of EG.

In case of EG growth on Si-face, the first layer carbon atoms formed is covalently bonded with the Si atoms on SiC(0001) (or Si-face), which has a $(6\sqrt{3} \times 6\sqrt{3})$ R30° periodicity with respect to the hexagonal SiC (0001) surface, so that it preserves the σ but lacks the π bonds of graphene (Emtsev et al., 2008). This carbon layer formed during the early stage of graphene growth is also called as zero-layer graphene or the buffer layer (Figure 2.8(a)) since it does not exhibit the electronic properties of graphene.

Further, this buffer layer introduces donor states that effectively creates n-type doping in the graphene layers grown above it (Emtsev et al., 2008). Additionally, this buffer layer is known to be detrimental for the charge carrier mobility in the graphene

35

layers on top of it. Unpaired electrons of the buffer layer (that derive from an unpassivated SiC surface band) lead to a series of partially occupied localized states that pin the Fermi level of the graphene over-layer, such that the Dirac point (E_D) and the Fermi level (E_F) no longer coincide (Emtsev et al., 2008): $\Delta = E_F - E_D > 0$. This is the origin of the observed *n* doping.
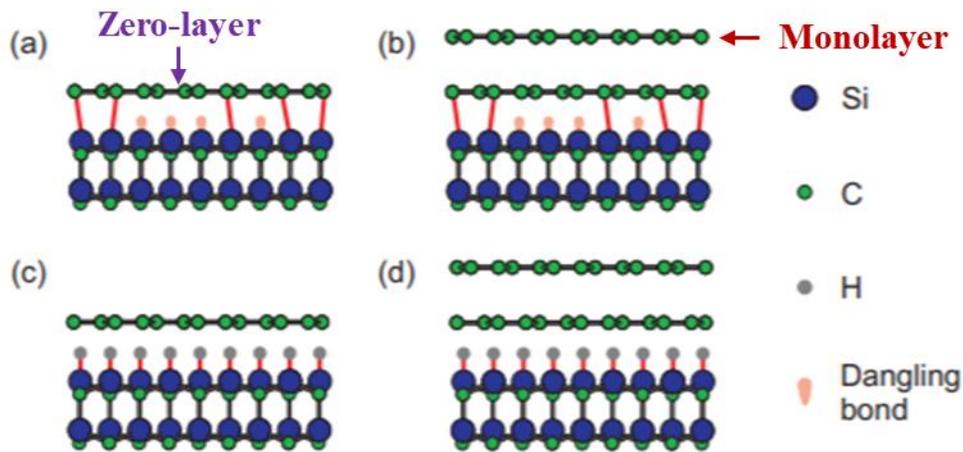
Figure 2.8 Side view models for (a) the $(6\sqrt{3}\times6\sqrt{3})R30°$ reconstruction of SiC(0001) ("zero-layer") and (b) epitaxial monolayer graphene. After hydrogen intercalation (c) the zero-layer and (d) monolayer graphene are decoupled from the SiC substrate (Riedl, Coletti, Iwasaki, Zakharov, & Starke, 2009).

Figure 2.9 shows the graphene/SiC Schottky junctions formed when graphene is grown on both p-type and n-type SiC epi-layers. As shown, the fermi-level of graphene is pinned to the conduction band of SiC (Varchon et al., 2007). The reason for this fermi-level pinning is explained by the dangling bonds present at the zero-layer graphene and SiC interface. Further, as shown in Figure 2.8(c) and(d), the fermi-level can be unpinned by saturating the dangling bonds present on SiC surface using different techniques such as H-intercalation (Riedl et al., 2009). Because of H-intercalation, the dangling bonds no longer exists at this interface and the fermi-level is now becomes unpinned. The buffer

36

layer, therefore, now becomes an additional, free standing, graphene monolayer as shown in Figures 2.8(c) and 2.8(d).
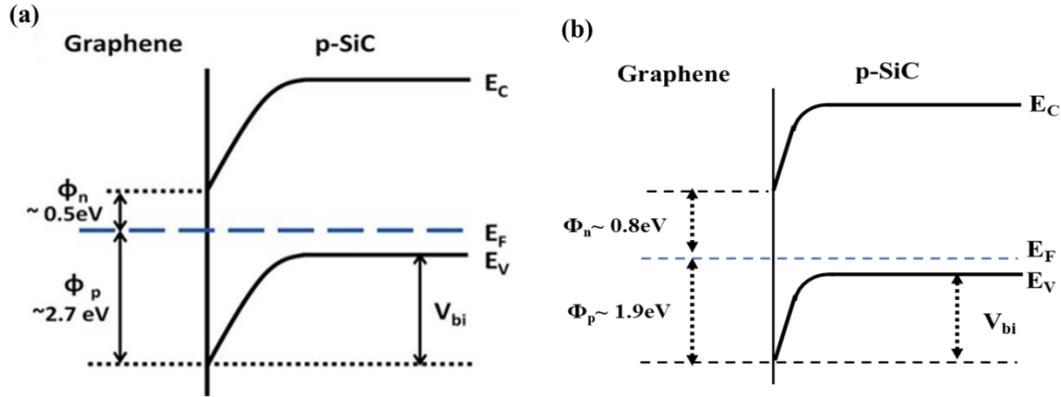
Figure 2.9 (a)Band diagrams for EG/p-Schottky junction before H-intercalation. As shown here, the graphene fermi-level is pinned to the conduction band edge of SiC (Anderson et al., 2015). (b) Band diagram of EG/p-SiC Schottky junction after H-intercalation. The fermi-level is now shifted by 0.3eV and therefore V_{bi} is also reduced. In this case, the EG fermi-level is not pinned to p-SiC conduction band.

2.4 GRAPHENE GROWTH BY SELECTIVE ETCHING OF SI USING TFS

The time required for EG growth using thermal sublimation is relatively high, as the process is limited by the slow evaporation of Si liquid droplets formed at >1400°C, making this method inefficient for practical applications. Additionally, this method is not suitable for growing thick graphene layers for applications such as in hydrogen storage (Luo et al., 2009), emission sensing (Biplob K. Daas et al., 2012) etc. To address this issue, a novel technique for EG growth on SiC by using TFS gas was developed recently at USC (Tawhid Rana et al., 2015).

37

As explained in chapter 1, the first step in SiC epilayer growth, using step controlled epitaxy, is etching SiC substrate to remove subsurface damage due to polishing. Although H_2 is routinely used for SiC etching step, this etching process is rather slow compared to SiC etching using both H_2 and TFS. This TFS can also be used to grow EG graphene as described below.

Table 2.1 Gibbs free energy (kcal/mol) for SiC dissociation and SiF_4 reactions (Tawhid Rana et al., 2015).

S.No.	Reaction	Gibbs Free Energy (in kcal/mol)		
	Dissociation and evaporation reactions for thermal sublimation growth	1800K (~1527°C)	1900K (~1627°C)	2000K (~1727°C)
1	$SiC(s) \rightarrow Si(g) + C(s)$	58.19	54.60	51.183
1a	$SiC(s) \rightarrow Si(l) + C(s)$	12.90	12.00	11.116
1b	$Si(l) \rightarrow Si(g)$	45.29	42.59	39.904
	SiF$_4$ reactions for graphene growth by Si selective etching			
2	$Si(l) + SiF_4(g) \rightarrow 2SiF_2(g)$	19.69	15.93	12.22
3	$C(s) + 1/4\ SiF_4 \rightarrow CF + 1/4\ Si(g)$	107.83	103.65	99.52
4	$C(s) + 1/2\ SiF_4 \rightarrow CF_2 + 1/2\ Si(g)$	128.23	124.16	120.19
5	$4C(s) + 3SiF_4 \rightarrow 4CF_3 + 3Si(g)$	184.63	180.62	176.69
6	$C(s) + SiF_4 \rightarrow CF_4 + Si(g)$	211.04	206.36	204.56
7	$2C(s) + 1/2SiF_4 \rightarrow C_2F_2 + 1/2Si(g)$	175.24	171.05	175.24

The novel EG growth technique using TFS precursor described here is basically an extension to thermal sublimation technique. In this technique, similar to thermal sublimation, when the SiC substrate is heated to a temperature >1400°C, the Si(l) droplets (step 1) are formed due to much high partial pressure of Si atoms. Now, when these Si(l)

38

droplets see a TFS gas molecule near the SiC surface, they can easily react with TFS

molecules to form SiF_2 gas (reaction 2 in Table 2.1), and these SiF_2 molecules can be easily

taken out from the growth reactor (as shown in steps II and III in Figure 2.10). Finally, the

C atoms on the surface rearranges themselves to form the graphene layer (step IV in Figure

2.10). Additionally, at 1600°C, the liquid Si droplets reacts readily with TFS gas (reaction

2 in Table 2.1) as much less energy is required (Gibbs free energy, $\Delta G=19.69$ kcal/mole)

for this reaction. Therefore, the reaction between liquid Si droplets and TFS gas is

thermodynamically more favorable when compared to evaporation of Si droplets which

requires high energy (Gibbs free energy ~45.29 kcal/mole). Also, the reaction of SiF_4

molecules with C atoms in SiC is less favorable due to high Gibbs free energy (211

kcal/mole) associated with these reactions. (reactions 3-7 in table 2.1).
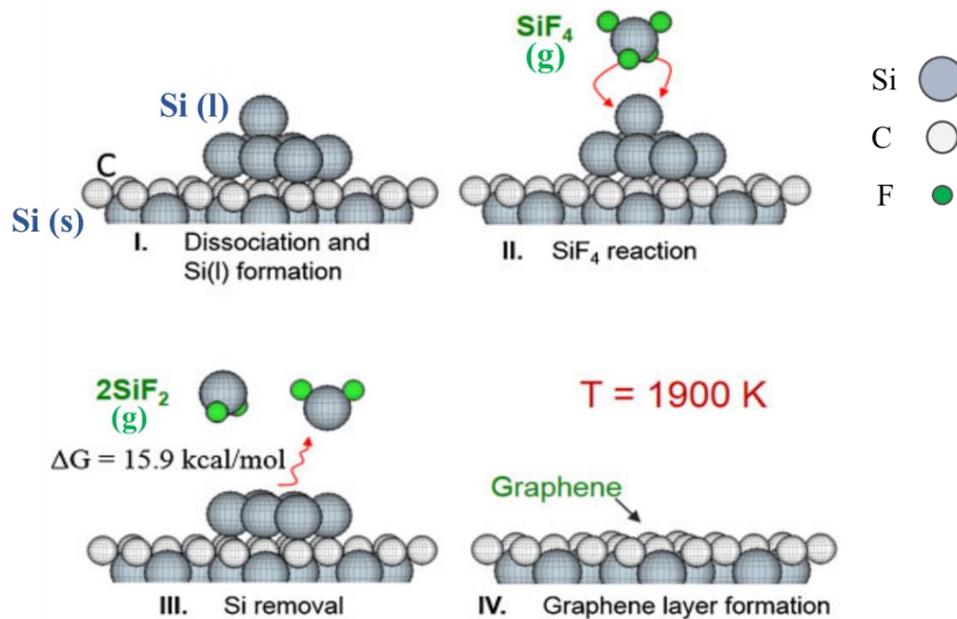
Figure 2.10. Reaction steps involved in epitaxial graphene growth using SiF_4. Dissociation
and Si(l) formation at temperatures >1400°C. II), III) Si(l) droplets are removed efficiently
by SiF_4 as SiF_2 gas. IV) Residual C atoms on the surface forms single layer of graphene
(Tawhid Rana et al., 2015).

39

In this study (Tawhid Rana et al., 2015), graphene layers were grown on SiC by varying the growth duration. From the Raman analysis of these samples, it was shown that graphene thickness can be varied as a function of growth duration (Figure 2.11) (Tawhid Rana et al., 2015) indicating the potential for thick-film growth. Also, the graphene peaks present in samples treated with Ar and TFS at 1400°C, gave much better quality of graphene as indicated by lower D/G ratio (<0.2).
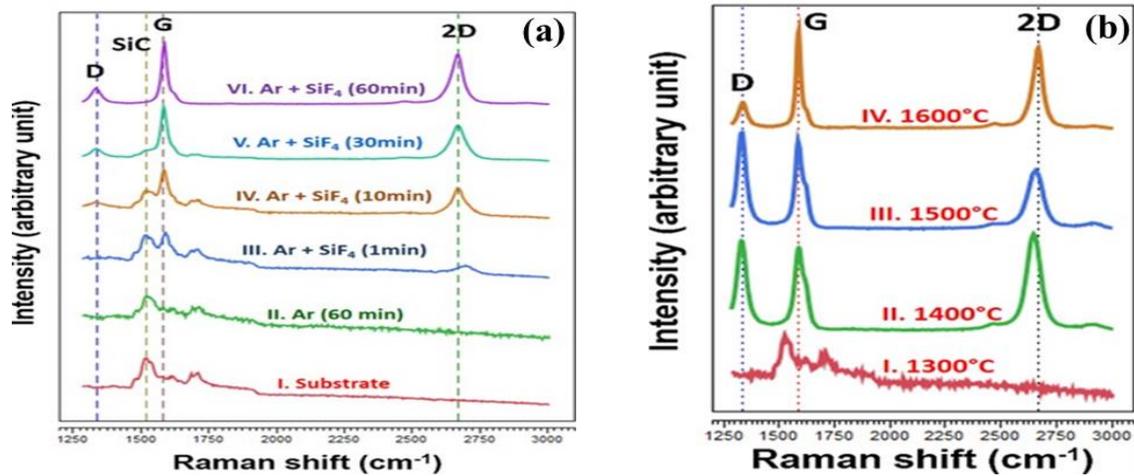
Figure 2.11 (a) Comparison of Raman analysis (without substrate subtraction) of surface treatment of 4H-SiC substrate for:I. substrate surface before treatment, II. surface treated for 60 min at 10 slm of Ar flow rate without SiF4. Surface treated for III. 1 min at 10 slm of Ar flow rate with addition of 10 sccm of SiF4 flow rate and subsequently for similar conditions with SiF4: IV. 10 min, V. 30 and 60 min. (b) Raman analysis of epitaxial graphene at various temperatures for a duration of 60 min at Ar and SiF4 flow rates of 10 slm and 10 sccm respectively while keeping the growth pressure at 300 Torr; I. no observable G-peak at a growth temperature of 1300 °C. II=III. A sharp elevation of G-peak, D-peak, and 2D-peak was observed at 1400 °C. IV. Lowest intensity of D-peak was observed at 1600 °C compared to layer grown at 1400 and 1500 °C. (Tawhid Rana et al., 2015).

Although, the increase in G peak intensity is a clear indication of thick film growth the actual thickness is not calculated, by XPS or FTIR, in the previous study. The measurement of graphene thickness is critical for practical applications such as in optical

detection where optical absorption by graphene increases with thickness. Further, electrical characteristics of the EG/SiC Schottky barrier junction such as ideality factor, barrier height etc. are not studied. The understanding of these electrical properties is key to use EG/SiC Schottky junction devices for practical applications such as in UV detection. The next section discusses the variation in thickness of EG grown on SiC, using TFS precursor, with time as measured by XPS. Also, EG/n-SiC Schottky diode fabrication and characterization is discussed to understand the electrical characteristics of the Schottky junction.

2.4.1 GRAPHENE GROWTH BY SELECTIVE ETCHING OF SI USING TFS: EFFECT OF COOLING RATE ON THE EG QUALITY AND EG/SIC INTERFACE ELECTRICAL PROPERTIES

As mentioned above, previous work by Rana (Tawhid Rana et al., 2015) was the first study for the development of controllable epitaxial graphene growth using TFS. Recently (Balachandran, 2017), EG growth on SiC using TFS is studied by varying the temperature during the reactor cooling process after the EG growth. The main purpose of this study is to understand the effect of cooling rate (thermal stress) on the morphology of EG and interface properties of EG/SiC Schottky junctions, that will affect the EG/SiC device properties (chapter 4).

Experimental details

For this study, nitrogen doped ($\sim 10^{19} cm^{-3}$), chemical-mechanical polished (CMP), commercial 4H-SiC substrates with various off cuts ($\sim 0°$, $4°$ and $8°$) as well as epilayers(n-type) grown on $8°$ 4H-SiC substrates were used. Samples were cleaned by standard RCA

cleaning method. All the graphene epitaxial growths were performed on the Si-face of the substrates/epilayers in a vertical hot-wall CVD reactor which is also used for SiC epilayer
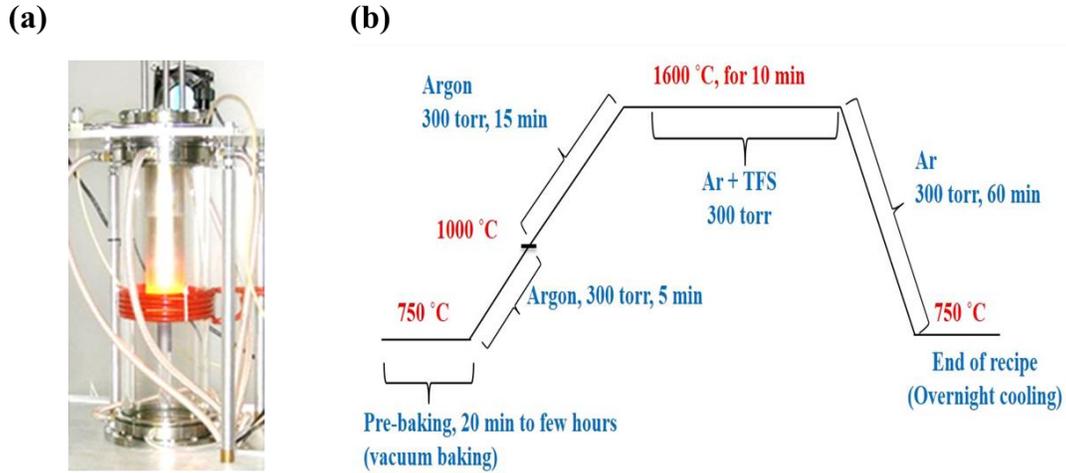
Figure 2.12 (a) The CVD growth reactor for EG growth on SiC, and (b) Process recipe for EG growth on SiC using TFS gas precursor. (A cooling rate of 14°C/min (or 60 minutes) is shown here for the temperature ramp down from 1600°C to 750°C). No surface pre-etching is done prior to the EG growth.

growth (Figure 2.12 (a)). The substrate was initially baked at 750°C in vacuum to remove any unwanted background impurities present inside the reactor. Then 6 slm Ar carrier gas flow was initiated to attain the growth pressure (300 torr). The temperature is ramped up to 1600°C from 750°C in ~20 minutes, at which point SiF_4 (Tetrafluorosilane or TFS) flow (60sccm) was initiated for the graphene growth for a duration of 10 min. Note that, no H_2 pre-etching was performed prior to the graphene growth step. Finally, the temperature was ramped down from the growth temperature to 750°C while flowing 6 slm Ar gas to maintain the 300 Torr pressure during the ramp down. Three different growth experiments were performed where the ramp down rate is different in each experiment. The ramp down rates used for these experiments were ~56°C/min (15 min), ~28°C/min (30 min) and

42

~14°C/min (60 min). Figures 2.12(a) and 2.12(b) show the growth reactor and process recipe used for the EG growth in this present study.

Characterization results of epitaxial graphene/4H-SiC

The characterization results of EG/SiC samples grown at different cooling rate are discussed below.

Atomic force microscopy (AFM) study:

The tapping mode atomic force microscopy (AFM) is used to study the surface morphology of graphene grown in these experiments. AFM height and phase images (5µm×5µm sizes) were recorded at different positions on the graphene layers. The surface roughness values, obtained from height images (Figure 2.13) for EG grown on different offcuts is found to vary for different cooling rates. The surface roughness for EG grown on on-axis substrates does not show obvious dependence on the cooling rates. For EG grown on 8° substrates, the best surface morphology is seen for the slowest cooling rate (14°C/min). On the other hand, the AFM phase images (Figure 2.14) of EG the grown on different offcuts for different cooling rates show interesting features. It is seen that the EG growth on on-axis substrates exhibit uniform phase images (thick graphene growth seen only at the step edges) irrespective of the cooling rates. For EG grown on 4° and 8° offcuts, the AFM phase images shown thick graphene nucleation, termed as '*cracking*' at random areas on the surface at different ramp down rates. The cracking phenomenon is attributed to mismatch in the thermal conductivity of EG and underlying SiC epi-layer and substrate. This cracking is observed to be uniform at the step edges for the slowest ramp down rate (14°C/min) for both 4° and 8° substrates and 8° epilayers.

43
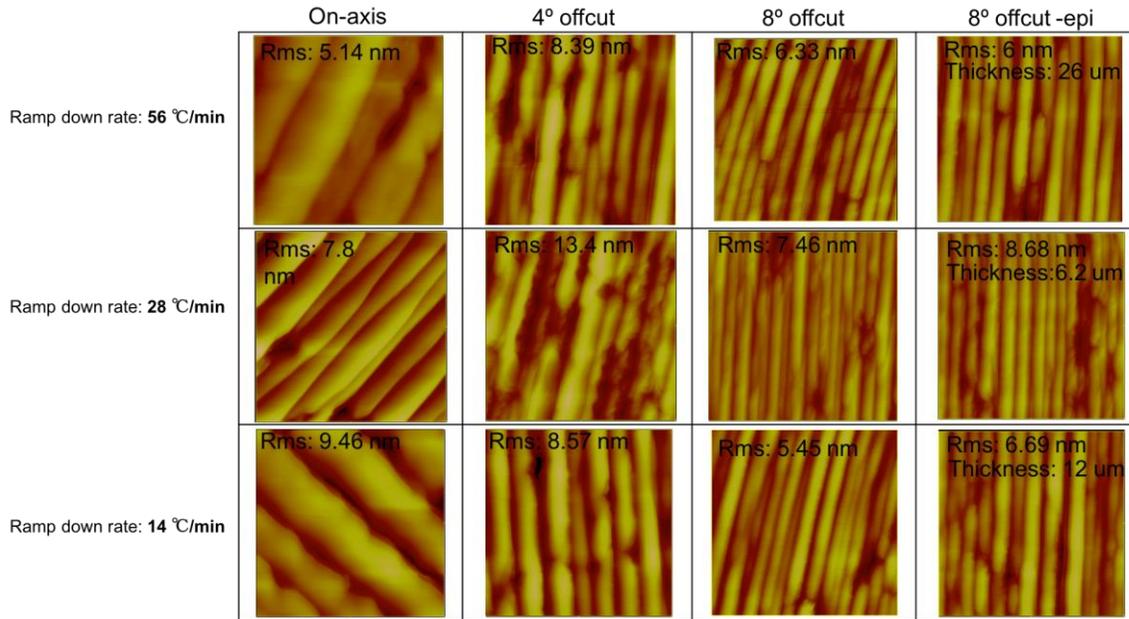
Figure 2.13 AFM height images (5 x 5 μm^2) of epitaxial graphene films grown on different offcuts of 4H-SiC substrates.
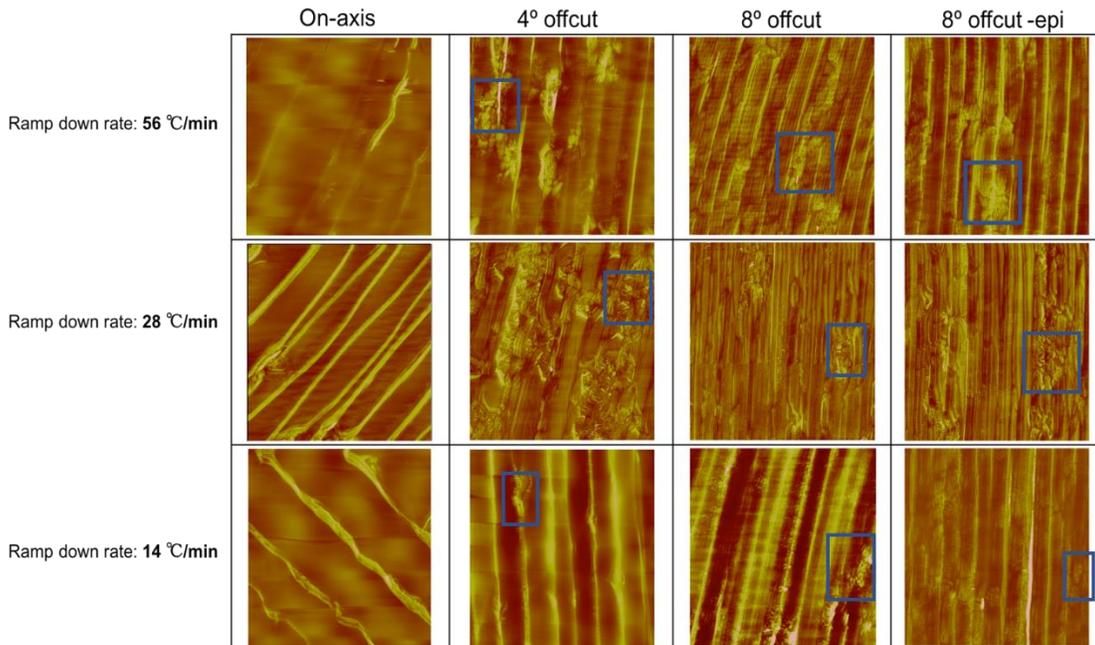
Figure 2.14 AFM phase images (5 x 5 μm^2) of epitaxial graphene films grown on different offcuts of 4H-SiC substrates. As shown the regions with cracks are marked in boxes.

Table 2.2 Summary of AFM phase image study (Figure 2.13) of EG grown on different off-cut substrates for different temperature ramp down rates.

Ramp down rate \ Sample type	On-axis	4° offcut	8° offcut	8° offcut-epilayer
56°C/min	No	Yes	Yes	Yes
28°C/min	No	Yes	Mild	Mild
14°C/min	No	May be	Very mild	No

The cracking phenomenon observed in the EG grown on off-oriented surfaces can be related to the increased kink density on the stepped surfaces (Robinson et al., 2009) which also contributes to the increase in EG surface roughness. As will be discussed later, the effect of crack densities seen for different ramp down rates can be correlated to the interface properties, by studying the electrical properties, such as the barrier height and ideality factor of the EG/SiC Schottky diodes.

Raman spectroscopy study

The Raman spectra of the graphene layers grown for all the ramp down rates are recorded using a Horiba micro Raman setup with laser excitation wavelength at 450nm and a spot size of ~2µm. These Raman maps (Figure 2.15(a)) show the peaks at 1350cm^{-1}, 1580cm^{-1} and 2700 cm^{-1}, typically observed in EG grown on SiC (Ni et al., 2008), corresponding to D, G and 2D peaks respectively. The D/G ratio indicates the presence of defects in the graphene layers and the closer the D/G ratio to 0 the better is the quality of graphene (Terrones et al., 2010)**.** These defects may be a result of surface dislocations, the corrugation, the vacancies and the interaction of graphene with substrate (Cançado et al., 2011). In general, this D peak is not observed in graphene obtained using mechanical exfoliation technique (Ni et al., 2008). Figures 2.15 (b) and 2.15(c) show the D/G ratio

45

and the 2D peak widths for all these samples plotted as a function of cooling rate. It is clear from Figure 2.14 (c), the D/G ratio for all the samples is <0.2, indicating better graphene quality and similar to D/G values reported previously by T.Rana (Tawhid Rana et al., 2015).
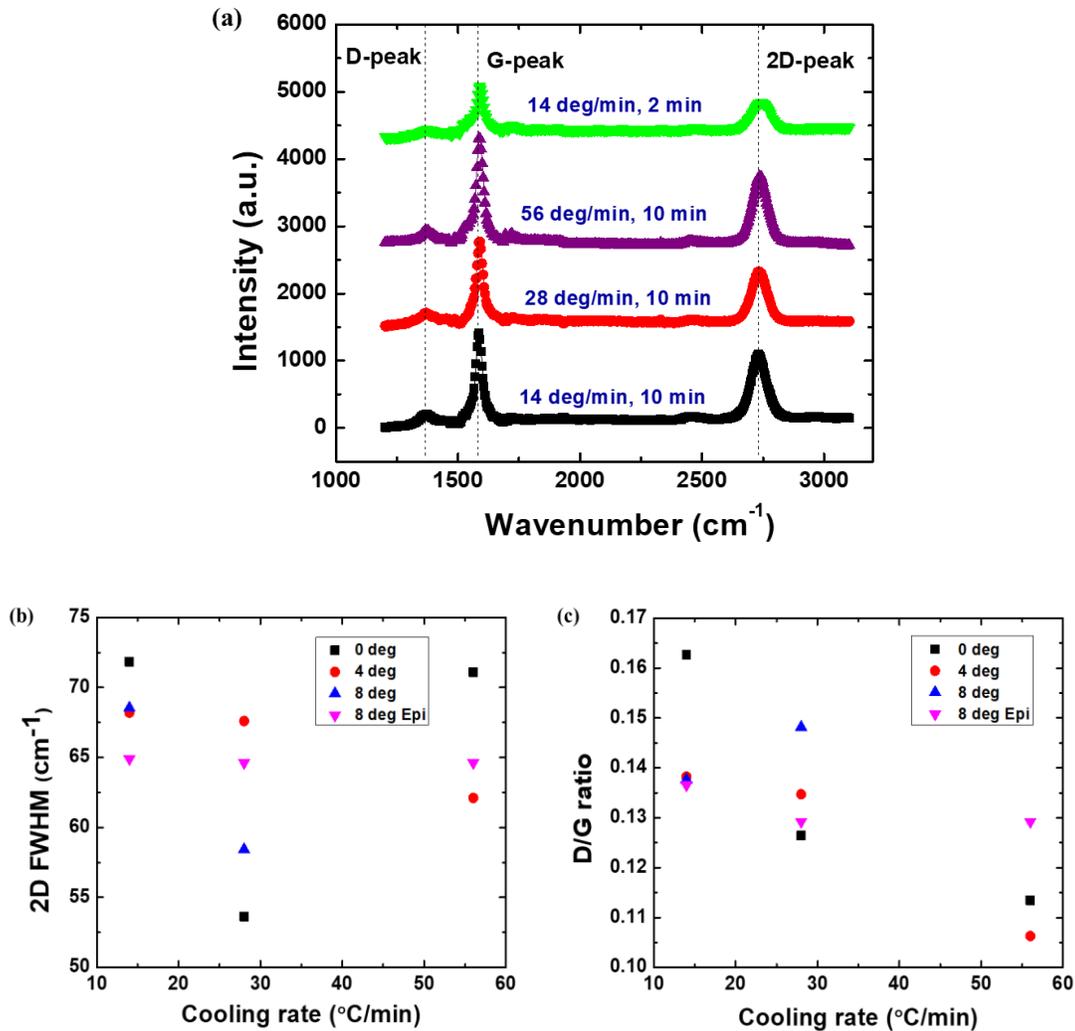
Figure 2.15 (a) Raman spectrum of EG samples grown on SiC for different growth times and cooling rates. (b) Peak intensity ratio(I_D/I_G) of D and G peaksand and (b)2D peak width of EG layers grown for different cooling rates on different offcut substrates and epi-layers at 1600°C.

46

The 2D peak in EG Raman spectrum is an indicator of the stacking order of the material. The Raman spectra of all graphene samples showed a symmetric 2D peak that could fit well with a single Lorentzian instead of split-peak seen for Bernal stacked graphene/graphite (Terrones et al., 2010). Ideal Bernal stacked graphite has a split asymmetric 2D peak, with each sub-peak corresponding to AB stacking responsible for graphene's linear electron dispersion. This shows that these films are not AB Bernal-stacked as seen usually with Si-face epitaxial graphene obtained by thermal sublimation, but instead have turbostratic, or mixed stacking (Garlow et al., 2016).

Further, the full-width at half-maxima(FWHM) of the 2D peaks of these graphene layers (Figure 2.15(b)) are in the range of 53-73 cm^{-1} indicating mobility values in the range of 10^2-10^3cm^2/V-s (Robinson et al., 2009). Also, the mobility values calculated using Hall measurement data on the TFS grown graphene layers is 700cm^2/V-s which is in excellent agreement with the mobility values from FWHM of 2D peak (Robinson et al., 2009).

X-ray Photoelectron Spectroscopy (XPS) study

X-ray photoelectron spectrum measurements were done to estimate the thickness of the graphene layers (Cumpson, 2000). The details for XPS measurement and thickness calculations of the EG layers from the XPS results can be found elsewhere (Balachandran, 2017).

The thicknesses of EG grown on 4° offcut substrates estimated using XPS measurement data, for different ramp down rates, are shown in Figure 2.16. It is clear from these results that thicker graphen layers can be grown efficiently for small growth duration (10 minutes), compared to 60 minutes in sublimation, by using TFS to remove Si(l)

47

droplets efficiently. In a similar EG growth experiment using TFS, the thickness of EG is estimated as 2-3ML, using XPS analysis (not shown here), for 2 minutes growth (cooling rate=14°C/min). These results indicates that EG thickness varies linearly with growth duration using TFS precursor. It can be concluded that a typical growth rate of 1.5 ML/min is possible for EG grown on SiC using TFS in Ar ambient at 1600°C.

(a) 13.9 ML (b)14.9 ML (c) 11.15 ML
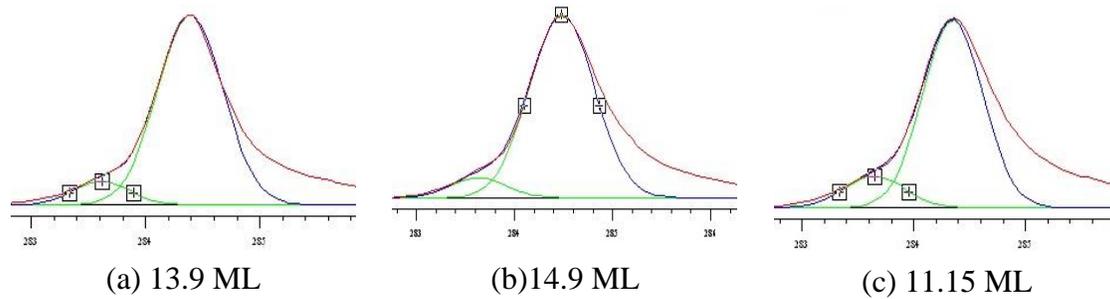
Figure 2.16 XPS data (Gaussian curve fitted) and thicknesses of EG grown on 4° offcut substrates for 10 minutes growth duration (a) 14°C/min, (b) 28°C/min and (c) 56°C/min ramp down rates.

EG/n-SiC Schottky diodes fabrication and electrical characterization results

To study the electrical properties of the epiaxial graphene/SiC inetrface, Schottky diodes fabricated using the graphene/n-SiC epilayer samples, grown on 8° off-cut n^+-SiC, substrates from each ramp down experiment. The thicknesses and doping of the epilayers used in this study for 14°C/min, 28°C/min and 56°C/min ramp down rates are 26 µm and 1.6×10^{14} cm^{-3}, 6.2 µm and 2×10^{15} cm^{-3}, and 12 µm and 4.5×10^{14}, respectively.

The fabrication process flow is schematically given in Figure 2.17. The mask pattern is transferred onto the EG layer by exposing the photoresist coated EG sample under 365nm UV light exposure using mask aligner and subsequent development in buffered KOH developer solution. Later, graphene mesa patterns are formed by etching the EG using O_2 plasma in a reactive ion etching (RIE) chamber. Here photoresist as a mask

48

for the EG mesa pattern and is removed after RIE process by dissolving it in acetone solution.
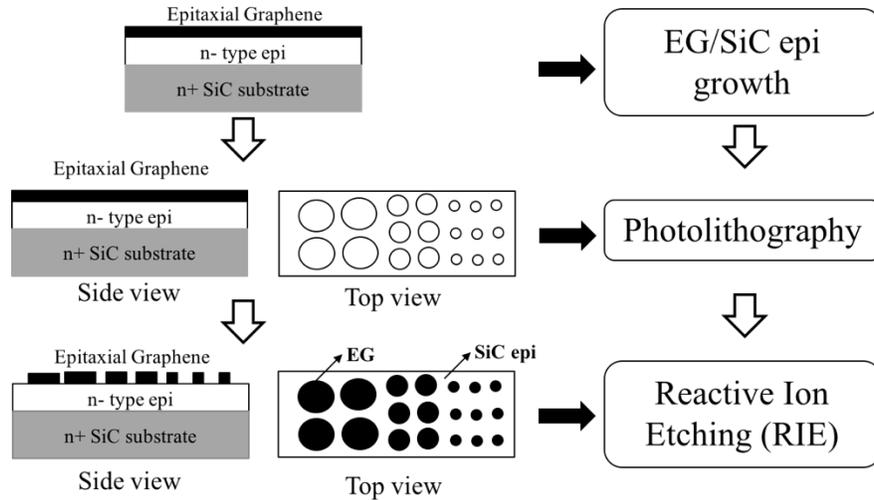
Figure 2.17 Fabrication process steps for EG/SiC vertical schottky diodes.

Current – Voltage characteristics of EG/n-SiC Schottky diodes

The Current-voltage (I-V) characteristics are measured for the EG/SiC Schottky diodes corresponding to three cooling rates. From these I-V test results (Figure 2.18(a)), the diode ideality factor(η), leakage current(I_0) and resistances (series and shunt) are calculated for all the devices (3 different size diodes, with EG mesa diameters 120µm, 180µm and 250µm) present on the Schottky diodes. The ideality factors (shown in Figure 2.18(b)) for the devices corresponding to slow and medium cooling rates is η=1.1 indicating better Schottky diode behavior compared to devices corresponding to fast cooling rate for which the ideality factor is η=1.3. The poor ideality factor in case of devices fabricated using EG grown in fast cooling rate experiment are can be attributed to thermal stress due to "cracks" formed at the EG and SiC interface causing the non-uniformity in the EG-SiC interface.

49
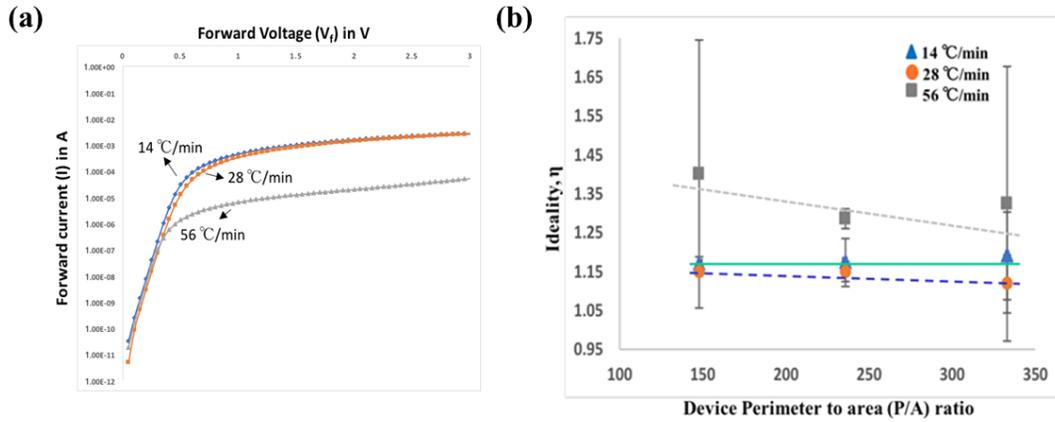
Figure 2.18 (a) Forward I-V characteristics, and (b) average ideality values for EG/n-SiC Schottky diodes at different ramp down rates with three different areas (each data point represents an average of 28 devices for the respective areas of the device.

The barrier heights for the EG/SiC Schottky junction were calculated using the leakage current densities of the diodes for different cooling rates (Figure 2.19) from thermionic emission equation given below:

$$\text{Schottky barrier height, } \Phi_B = \frac{kT}{q}\ln\left(\frac{J_0}{A^*T^2}\right) \qquad (2.6)$$

where, Richardson's constant, $A^* = 143$ A/cm^{2}K^2 for 4H-SiC, T= 300K, J_0 = leakage current density (A/cm^2) and $\frac{kT}{q}$ is the thermal voltage at 300K = 0.0259eV.

Figure 2.18 shows the calculated barrier heights as a function of perimeter area ratio of the devices. From this figure, it is clear that the variation in barrier height Φ_B values for different P/A ratios is more in case of the EG/SiC devices corresponding to the fast cooling rate. The barrier heights for devices corresponding to medium and slow cooling rates, on the other hand, showed little variation with perimeter/area ratio, indicating that slower cooling rates indeed helped in minimizing the thermal stress at the EG/SiC interface, during the temperature down step in the last stage of the growth process.

50
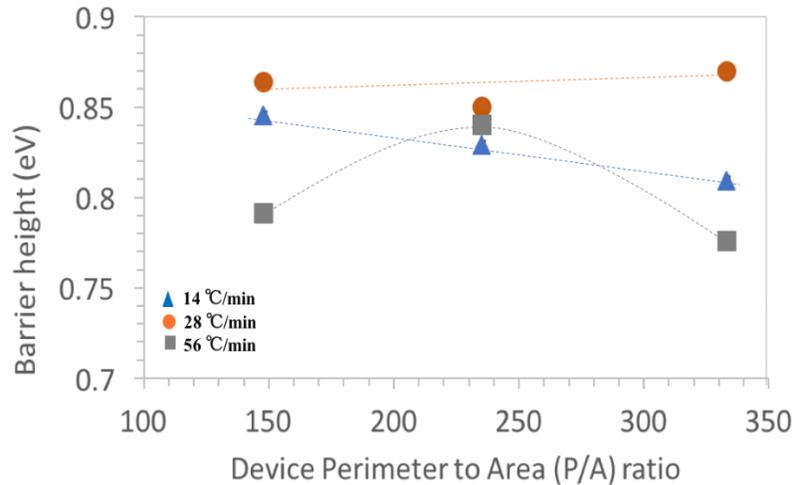
Figure 2.19 Schottky barrier height (Φ_B) of EG/n-SiC Shottky junctions obtained for an average of 28 devices for different P/A of the devices (trend lines shown are guide to the eyes).

2.5 SUMMARY

The graphene growth methods mainly thermal sublimation growth and EG growth using selective etching of SiC using TFS are reviewed. It is confirmed from the XPS measurements that EG thicnkess increases linearly with time(1-1.5ML/minute) in the TFS growth method. The TFS accelerated growth of EG has significant advantage in terms of cycle time compared to thermal sublimation as higher EG growth rates are observed using the TFS growth technique. The graphene layers grown using TFS showed better quality as indicated by low D/G peak ratio observed in the Raman spectral studies. Additionally, the barrier height of EG/n-SiC Schottky diode fabricated using TFS grown EG is significantly large compared to barrier heights of EG/n-SiC Schottky junction formed by thermal sublimation method (0.8eV for TFS growth vs 0.5eV for sublimation). Finally, the high quality EG layers grown using this controllable EG growth technique can be used in optoelectronic devices such as in photodetectors.

51

CHAPTER 3

EPITAXIAL GRAPHENE/4H-SIC HETEROJUNCTION BASED BIPOLAR PHOTOTRANSISTORS FOR UV DETECTION[1,2,3]

3.1 INTRODUCTION

UV photodetectors have a wide variety of applications in defense for plume detection, flame sensing, and also as biological and chemical sensors (M. Razeghi & Rogalski, 1996). Solid state UV detectors based on Si, SiC, GaN, AlGaN, InGaAs and GaAs are popular due to their reliability and light weight. Although Si based UV detectors are popular for commercial applications, they are sensitive to visible light and therefore need to be used with optical filters that block the visible light. Therefore, UV photodetectors based on wide bandgap semiconductors like 4H-SiC (E_g=3.26Ev for 4H-SiC) are a better choice for visible-blind UV detection, and can be operated in high temperature and harsh environment conditions due to high radiation and chemical hardness. In the past, many research groups reported SiC UV detectors based on Schottky, MSM and p-i-n structures (E. Monroy, Omnès, & Calle, 2003), (Manijeh Razeghi, 2002).

---

[1]V. S. N. Chava, S. U. Omar, G. Brown, S. S. Shetu, J. Andrews, T.S.Sudarshan, MVS Chandrashekhar, Appl. Phys. Lett. **2016**, 108 (4), 043502. Reprinted here with permission of publisher.
[2]V. S. N. Chava, B. G. Barker, K. M. Daniels, A. B. Greytak, MVS Chandrashekhar, SENSORS, IEEE, **2016** (pp. 1-3). Reprinted here with permission of publisher.
[3]Barker, B. G.; Chava, V. S. N.; Daniels, K. M.; Chandrashekhar, M. V. S.; Greytak, A. B. 2D Mater. **2017**, 5 (1). Reprinted here with permission of publisher.

Traditional UV detectors with metal contact electrodes, however, suffer from low UV responsivities(R), due to the reflection/absorption losses caused by the metal electrodes. Later, UV detectors with improved responsivities(R) are developed by using semi-transparent metal contacts (A. Sciuto et al., 2007), where the semi-transparent contacts can transmit more than 70% of the UV light incident on the device.

Graphene forms a Schottky junction with semiconductors such as Si, GaAs, SiC etc. (Tongay et al., 2009). Further, Epitaxial graphene(EG)/SiC Schottky junction devices are of particular interest due to the advancement in the growth technology of both epitaxial graphene (Tawhid Rana et al., 2015) and 4H-SiC (Haizheng Song, Tawhid Rana, M.V.S. Chandrashekhar, Sabih U. Omar, 2013). Additionally, the EG grown on top of SiC, which is 2-3 atomic layers thick (absorption ~0.6%/monolayer on SiC, 1ML=0.34nm, (Dawlaty et al., 2008)), can be used as a transparent metal contact for SiC UV detectors, and therefore does not strongly absorb UV photons(λ:10nm-400nm) which would otherwise be absorbed in the surface layer of a pn junction, typically ~100nm thick. Moreover, as explained in chapter 2, graphene grown on p-SiC by thermal sublimation forms a Schottky junction with a large barrier height ~2.7eV (Coletti et al., 2013). As Schottky devices are typically majority carrier devices they offer advantages like fast switching time due to fast recombination in the metal, and minimal series resistance in the emitter, as has been shown in bipolar mode Schottky devices (Y.Mizushima, 1984). Moreover, the large Schottky barrier height to p-SiC (which is ~2.7 eV) in our device would result in reduced reverse leakage current (Schoen, Woodall, Cooper, & Melloch, 1998), potentially breaking the tradeoffs in speed and leakage current between unipolar and bipolar devices in certain

53

applications. In this chapter, the performance characteristics of an EG/p-SiC/ n$^+$-SiC vertical bipolar junction UV phototransistor are discussed.

3.2 EG/SiC HETEROJUNCTION BIPOLAR PHOTOTRANSISTOR

3.2.1 EXPERIMENTAL DETAILS

As shown in Figure 3.1, a vertical bipolar transistor is fabricated with an EG emitter, p-SiC base, and n$^+$ -SiC collector layers. Epitaxial growth of p-SiC on commercially available 4^0 off-cut n$^+$-SiC (0001) substrate is done in a CVD growth reactor by using Propane and Dichlorosilane(DCS) gas precursors. A high C/Si ratio of 1.2 is maintained in the source gas mixture during the CVD growth process. The pressure and temperature are maintained at 300 Torr and 1600^0 C respectively. The epi-layer is characterized by using mercury probe capacitance-voltage measurements and Fourier Transform Infrared Reflectance(FTIR) techniques for calculating the doping and thickness. The epi-layer thicknesses (i.e., the base width, W_B) as measured by FTIR was ~30 μm (Macmillan, Henry, & Janzeni, 1998). The net carrier concentration(N_A-N_D) for the p-epilayer, as measured by mercury probe C-V method (Haizheng Song, Tawhid Rana, M.V.S. Chandrashekhar, Sabih U. Omar, 2013)**,** is found to be $3x10^{14}$ cm^{-3}. The epitaxial graphene (EG) was grown by thermal sublimation of the p-SiC epi-layer surface in vacuum at 1350^0 C, and the growth process is described in greater detail in chapter 2. The presence of graphene was confirmed by the Raman spectra obtained using a Horiba JY spectrometer with an excitation line of 631 nm. The D/G ratio was estimated to be <0.06. The XPS measurements showed EG thicknesses of 2-3 monolayer in similar growth conditions (B. K. Daas et al., 2012). The 250 μm diameter circular graphene mesa structures were defined

using an O_2 plasma reactive ion etching (RIE) through a photoresist mask. An RF-sputtered Ti(40nm)/Au(20nm) film was used to form a large area ohmic contact on the back of the SiC substrate. Note that the base p-SiC epilayer is not mesa isolated as it is difficult to etch large depths of SiC selectively using the RIE system.

As show in Figure 3.1, the device has an EG/p-SiC Schottky junction at the top and p-SiC/n^+-SiC p-n junction at the back. The reason why this device is called a bipolar junction transistor(BJT), however, will become clear later (see section 3.2.2) when the device current-voltage (I_c-V_{CE}) characteristics under UV illumination are discussed. In general, a BJT is said to be operated in forward active mode, when the emitter-base(E-B) junction is forward biased and the base-collector(B-C) junction is reverse biased. Similarly, the present EG/SiC device acts as a BJT in forward active mode when the graphene/p-SiC (emitter-base) junction is forward biased and the p-SiC/n^+-SiC (base-collector) junction is reverse biased under UV illumination. Here after, we call the forward active mode of operation as *Schottky Emitter (SE)* mode (Figure 3.2(b)), and the device in SE mode as *Schottky Emitter phototransistor(SEPT)*.
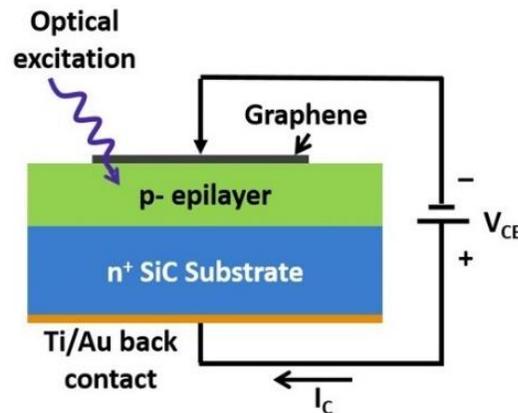
Figure 3.1 Schematic of EG/p-SiC/n^+-SiC vertical bipolar UV phototransistor (SEPT) operated in Schottky Emitter(SE) mode.

55

For phototransistor operation, the graphene emitter was held at a negative bias with respect to the n^+-SiC emitter layer by directly contacting the graphene layer with a tungsten probe, and this makes the EG/p-SiC Schottky junction forward biased (Figure 3.1). Here, the base (p-SiC) is floating and the base photocurrent was provided by optical excitation from an Omnicure S1000 Hg-vapor lamp with variable intensity as the illumination source in a microscope with 10x objective. The UV light intensity of this lamp is further attenuated by placing a SiC wafer at the inlet, along with an additional aperture to limit the spot size to <200 µm i.e., to confine it to the limits of the device. The lamp spectrum provided three excitation lines at 312nm, 334nm and dominant 365nm wavelengths which are above the bandgap for SiC. The UV power incident on the device is varied by changing the intensity of the output power of the Hg-vapor lamp. The optical power incident on the device under study was measured using a calibrated Si photodiode sensor PM100D from Thorlabs.

3.2.2 RESULTS AND DISCUSSION

Figure 3.2(a) shows the typical *collector current* (I_c) vs collector-emitter voltage (V_{CE}) characteristics for the EG/p-SiC/n^+-SiC SEPT measured at different UV illumination powers. Figure 3.2(b) shows the *photocurrent* $(I_c)_{ph}$ vs bias voltage(V_{CE}), where $(I_c)_{ph}$ is obtained by subtracting the dark current from the collector current at each UV power. In our present study, the UV illumination is varied from 0.43 µW to 7.87 µW, corresponding to the measured short circuit current (I_C at V_{CE}=0V) values 43.5 pA to 50.4 pA. The relatively large dark current is attributed to the lack of mesa isolation between the p-SiC base and n^+-SiC collector, as it is difficult to etch large depths of SiC selectively, 30 µm in this situation ensures adequate absorption of the 365 nm UV light. Also, it is clear, from Figure 3.2(b), that the collector photocurrent $(I_c)_{ph}$ increases with the UV light power.

56
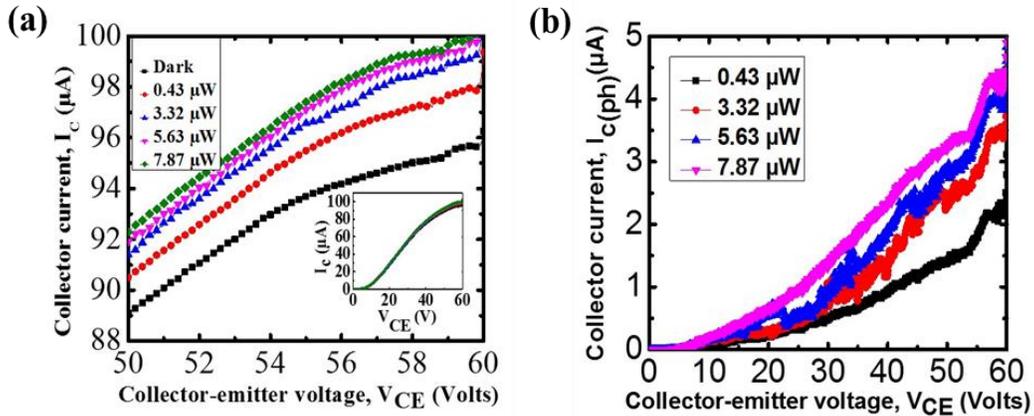
Figure 3.2 (a) Current-voltage characteristics and (b) photocurrent-voltage characteristics of a typical EG/ p- SiC/n$^+$- SiC SEPT under various UV light illumination levels. (Inset in Figure 3.2(a) shows full range of measured current-voltage (I_c vs V_{CE}) characteristics).

Now let us consider the carrier transport in the device, under an applied bias voltage (V_{CE}), in dark and also under illumination. As shown in Figure 3.2(a), in dark condition, the collector current(I_C) increases with an increase in the emitter-collector bias voltage (V_{CE}). This increase in I_C with applied V_{CE} can be explained by considering the EG/p-SiC Schottky junction. When the applied V_{CE} increases, the forward bias voltage at EG/p-SiC Schottky junction also increases. As a result, the barrier at the EG/p-SiC gets lowered with an increase in forward bias voltage at this junction, and in this situation a number of holes that can overcome the Schottky barrier to reach the EG emitter region is more compared to the number of holes that can overcome the barrier in equilibrium condition (see Figure 3.3). This increase in hole injection is clearly visible in Figure 3.3(a), where I_C increases at V_{CE} ~2.7V, which is the Schottky barrier height for holes in p-SiC. Figure 3.3 shows the energy band diagram of the device in equilibrium (Figure 3.3(a)) and under illumination (Figure 3.3(b)).

57
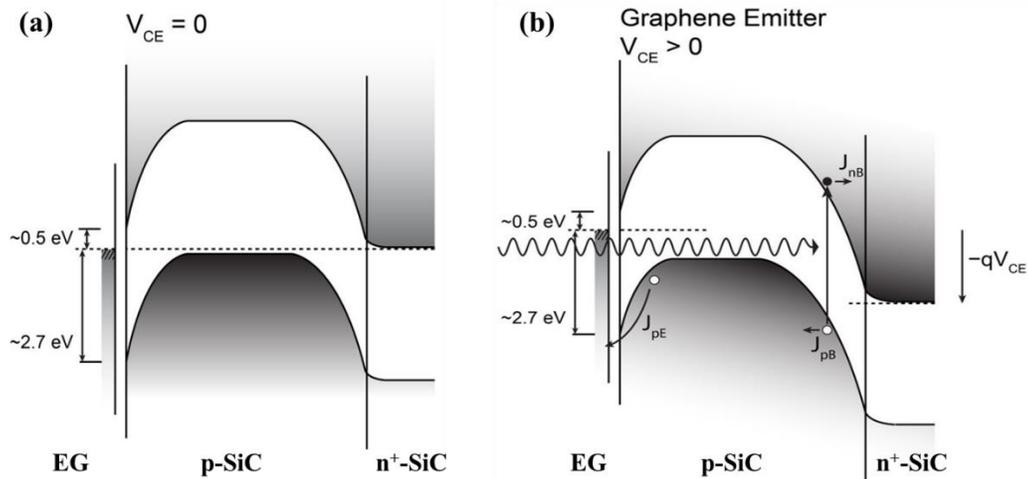
Figure 3.3 Energy band diagram of the EG/p-SiC/n$^+$-SiC Schottky emitter bipolar phototransistor (SEPT) (a) in equilibrium (b) under UV illumination and applied bias (V$_{CE}$).

Also, from Figure 3.2(b), it is clear that the collector photocurrent (I$_c$)$_{ph}$ increases with the UV light power. Now, when the device is illuminated with a UV lamp, the incident UV light is transmitted through the highly transparent EG at the top (see the band diagram in Figure 3.3(b)), and gets absorbed in the base (p-SiC epilayer) and collector (n$^+$-SiC substrate) layers. Therefore, electron-hole (e-h) pairs are generated in the SiC base and collector layers as a result of UV photon absorption. Further, due to the applied reverse bias voltage (V$_{CE}$) at the p-SiC/n$^+$-SiC (base-collector) junction, the optically generated holes are swept into the base(p-SiC) region and electrons are swept into the collector (n$^+$-SiC substrate) region. In this case, the photogenerated carriers (both electrons and holes) within a diffusion length distance from the B-C depletion region edges are swept by the electric field at this junction. These holes in the base region, however, see a large potential barrier (~2.7eV) near the EG/p-SiC interface and therefore contributes to very little (I$_c$)$_{ph}$. These holes also contribute to the base current and therefore, the base current in the device is varied by changing the UV illumination power. This variation in collector current with

58

incident UV power (or base photocurrent) is similar to variation in the collector current with injected base current observed in a conventional npn transistor.

In this SEPT, the optically generated carriers are multiplied by the transistor common emitter gain and thus enhances the collector current depending on how this gain changes. Optical gain (h_{FE}) (Sze & Ng, 2006) is given by:

$$h_{FE} = \frac{(I_C)_{ph}}{I_b} \qquad \text{(Eq.3.1)}$$

where $(I_c)_{ph}$ is the measured collector current after subtracting the dark current and I_b is the base current. The subtraction of unity in Equation 3.2 accounts for the photogenerated current, which should not be double counted. In a conventional BJT, the gain (or collector current) is controlled by varying the current injected into the base terminal. As already mentioned the present device is open base phototransistor and therefore the base current is varied by varying the UV illumination power. Therefore, the collector current is controlled by the UV illumination power (or base current) which is clearly seen in Figure 3.3(b). The base photocurrent (I_b or I_{ph}) (Sze & Ng, 2006), generated by the absorption of incident UV photons in the base region, is calculated by:

$$I_b = I_{Ph} = P_{Opt} \frac{1 - \exp(-\alpha_{abs} W_b)}{E_{Ph}} \qquad \text{(Eq. 3.2)}$$

Here P_{opt} is the incident UV power, W_b is the neutral base width, α_{abs} is the absorption coefficient, approximately ~80cm^{-1} (Sridhara, Devaty, & Choyke, 1998) for 365nm wavelength photons in 4H-SiC, E_{ph} is the energy of UV photons corresponding to 365nm. We assumed the reflectance of our device is the same as that of the Si photodiode, therefore the measured P_{opt} by Si photodiode represents the number of UV photons passing through

59

the device. All calculations are done by assuming the UV light as a monochromatic UV radiation since the 365nm line is dominant in the UV lamp spectrum.

Figure 3.4 shows the variation in current gain calculated using Equation 3.1 and Equation 3.2, with UV power at V_{CE}=60V. A maximum current gain of 113 is estimated when the illumination level is set to be 0.43 µW. The current gain values decreased steadily by increasing the incident UV power.
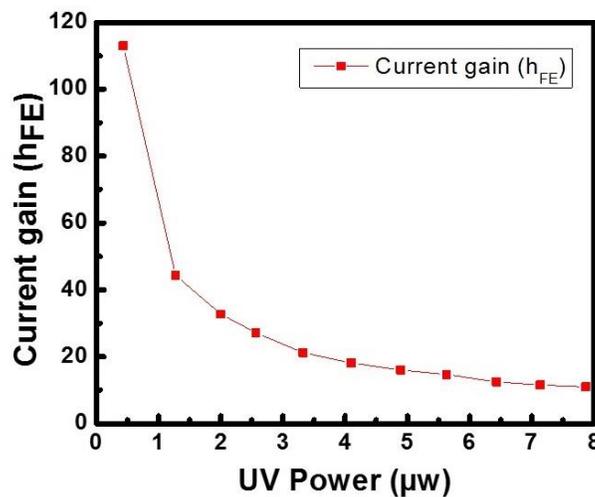
Figure 3.4 Variation of current gain (h_{FE}) of SEPT with incident UV illumination power at V_{CE}=60 V.

Here after, we explain the transistor action in the present SEPT device as an equivalent of conventional npn transistor. Using the npn transistor analogy, the hole injection across the EG/p-SiC Schottky junction is considered in the following discussion to be equivalent to electron injection from the n-emitter in an npn transistor. In reality, the carrier transport at EG/p-SiC occurs only by thermionic emission of majority carrier holes from p-SiC into EG. Remember, there is a barrier of 0.5eV for electrons in EG where the fermi-level is pinned to the conduction band edge of p-SiC (Figure 3.3) and this barrier will not change, similar to the fixed barrier height for carriers in the metal side in case of a

60

Schottky diode devices, with the applied bias voltage(V_{CE}). Thus, as the photo current $(I_c)_{ph}$ increases, the total number of injected electrons and holes in the base also increase, leading to faster recombination of carriers in the base, which is proportional to the np product (Sze & Ng, 2006). This suggests that base recombination is the limiting mechanism of the gain in this device, similar to that observed in GaN heterojunction bipolar devices (Yang, Nohava, Krishnankutty, Torreano, Mcpherson, et al., 1998). The device characteristics of other devices fabricated on the same substrate with same dimensions also found to show similar I-V characteristics and the gain values are also in the same range.

Further below, we exclude the possibility of gain from avalanche processes, as well as persistent photoconductivity, only leaving bipolar gain as a possibility. In general, the gain in photodetector can occur by any of three mechanisms namely i) photoconductive (Yang, Nohava, Krishnankutty, Torreano, Mcpherson, et al., 1998), ii) avalanche (Joe.C. Campbell, Dentai, Qua, & Ferguson, 1983) and iii) bipolar gain (Kunihiro Suzuki, 1991) depending on the device structure and applied bias. Below, it is confirmed that the current gain is due to bipolar gain (transistor action) alone by excluding the possibility of photoconductive and avalanche gain.

The transit time($\tau_{transit}$) of electrons at low injection in the base region by using the diffusion equation (Kunihiro Suzuki, 1991):

$$\tau_{transit} = \frac{W_B^2}{2D_n} \qquad \text{(Eq.3.3)}$$

At V_{CE}=60V, the transit time ($\tau_{transit}$) is estimated to be 180ns, using the above Equation 3.3. Also, the lower bound for the recombination time, $\tau_{recombination}$, of electrons diffusing from base to collector is estimated by assuming the recombination velocity of electrons at

61

the p-SiC/n$^+$-SiC BC junction terminal as >10^{5}cm/s as measured by Kimoto (Kimoto, Hiyoshi, Hayashi, & Suda, 2010), and $\tau_{recombination}$ value is estimated to be <30ns for a 30µm base. Therefore, since $\tau_{recombination}$< $\tau_{transit}$, the carrier recombines as soon as it makes one pass through the long 30µm base. Thus, we can exclude the possibility of photoconductive gain here.

In avalanche photodetectors, the photocurrent and dark current are increased by a multiplication factor M (Joe.C. Campbell et al., 1983) given by the equation:

$$M = \frac{1}{1-\left(\frac{V_{CB}}{V_B}\right)^n}$$ (Eq.3.4)

Here, V_{CB} is the collector-base voltage, V_B is the breakdown voltage of the B-C junction and n is an empirical factor that depends on semiconductor type, doping and wavelength. For 4H-SiC, V_B is calculated (Baliga, 2008) using:

$$V_B = 3 \ X \ 10^{15} X (N_D)^{-3/4}$$ (Eq.3.5)

The breakdown voltage (V_B) for the p-SiC/n$^+$-SiC (B-C) junction is estimated to be ~10^4 V corresponding to a doping N_D=3x10^{14} cm^{-3} in the p-SiC base. A multiplication factor of M=1 is estimated by using Equation 3.5. Since here V_{CB}<<V_B, we do not expect avalanche breakdown at the p-SiC/n$^+$-SiC (B-C) junction in our device. Typically, in devices that show avalanche breakdown, the current increases sharply (by few orders) for a small change in applied bias voltage near the breakdown. From the I_c vs V_{CE} (as shown in Figure. 3.2), no such sharp increase in the collector current is observed with the applied bias voltage (V_{CE}), and therefore the possibility of the avalanche gain is excluded in these device structures.

The analysis below is for an npn transistor whose action is similar to the SEPT device considered in our present study. From the measured collector current, the peak value of electron concentration at the edge of base-collector depletion region (see Figure 3.3(b)) is estimated to be 5×10^{13} cm^{-3} (from eq. 3.6) by assuming that the concentration of electrons at the back edge of the collector is zero (recombination velocity $>10^5$ cm/s at the back interface (Kimoto et al., 2010). For the estimation of the electron concentration in the base-collector depletion region edges (no recombination in the depletion region), we used Fick's law of diffusion in the neutral base region:

$$qD_n \frac{dn}{dx} = I_n \qquad \text{(Eq.3.6)}$$

Here D_n is the diffusion coefficient of electrons and q is the charge of the electron known. Since epi layer (base) doping is 3×10^{14} cm^{-3} $> 5 \times 10^{13}$ cm^{-3}, indicating low injection level. This low injection level is valid for the highest collector current obtained for 7.87μW illumination at 60V. Hence even at the maximum UV power illumination used in this study, we have low-level injection condition.

The responsivity(R) of the SEPT device at 365nm at zero bias voltage(V_{CE}=0V), calculated as the ratio of $(I_c)_{ph}$ and incident UV power, is 0.25 mA/W for 0.43 μW UV illumination. The responsivity(R) is increased with an increase in the bias voltage (V_{CE}) and reached a maximum value of 7.1 A/W at V_{CE}=60V. It should be noted that the UV responsivity(R_{365nm}) of the present device is better than the recently reported EG/SiC UV detector (Anderson et al., 2015) and graphene/SiC MSM photodetector (Kusdemir et al., 2015) which showed a maximum responsivity of 0.2 A/W at 310 nm and 2 mA/W at 365 nm in the respective order. Further, similar to the current gain, the responsivity(R_{365nm}) at

63

V_{CE}=60V also decreased with an increase in the incident UV power and therefore can be attributed to the recombination in the base region as discussed previously for the case of current gain.

Table 3.1 Comparison of near UV(365nm) responsivities of SEPT with previously reported UV detectors.

S. No.	UV detector type	R at 365nm (in A/W)
1	EG/SiC SEPT (this work)	7.1
2	EG/SiC PN diode	0.2 at 310nm
3	EG/SiC MSM*	2×10^{-3}
4	4H-SiC PiN diode	1×10^{-3}
5	4H-SiC APD**	1×10^{-2}
6	GaN PiN diode	1.5×10^{-3}
7	GaN PN diode	0.1

*MSM: Metal- Semiconductor-Metal, **APD-Avalanche Photodiode
References cited here in Table 3.1:
2- (Anderson et al., 2015), 3- (Kusdemir et al., 2015), 4-(X. Chen, Zhu, Cai, & Wu, 2007),
5- (Zhu, Chen, Cai, & Wu, 2009), 6- (Zhu et al., 2009), 7- (Eva Monroy et al., 1998)

Table 3.1, shows a comparison of ultraviolet responsivities of SEPT with previous works. From this table, it is clear that SEPT shows better responsivity compared to other devices in the near UV regime.

3.3 HYDROGEN INTERCALATION STUDY

3.3.1 INTRODUCTION

In section 3.2, it is demonstrated that vertical EG/p-SiC/n$^+$-SiC devices, when operated in Schottky emitter mode, show high current gain (113) and high responsivity (7.1 A/W) under 365 nm UV illumination. Further, the high gain and responsivity in these device structures is attributed to minority carrier (electron) injection from EG into p-SiC.

As discussed in chapter 2, when Epitaxial graphene (EG) layer is grown on SiC (0001), there is a carbon (buffer) layer formed at the interface of EG/SiC junction, and also the fermi level of EG is pinned to SiC conduction band due to dangling bonds presented at the EG/SiC interface (fig. 2.8). Further, the fermi-level of EG is located at 0.3 eV above the Dirac point(E_D) (Coletti et al., 2013). On the other hand, the EG fermi level can be unpinned by passivating the dangling bonds, present at the buffer layer (also called "zero-layer" graphene) and p-SiC interface, by hydrogen intercalation process (Riedl et al., 2009). Further, as a result of H-intercalation process, the fermi-level of epitaxial graphene shifts below the Dirac point by 0.5 eV (E_D) (Coletti et al., 2013). Therefore, it is of interest to understand how the fermi-level shift influences the carrier injection efficiency, and thus gain of the present EG/SiC SEPT device. In this section, the effect of hydrogen intercalation process on the I-V and gain characteristics of the SEPT devices are discussed (Chava, Chandrashekhar, Daniels, Barker, & Greytak, 2016).

3.3.2 EXPERIMENTAL DETAILS

The sample consisting of EG/p-SiC/n$^+$-SiC vertical BJT devices is placed in an Aixtron horizontal hot-wall reactor where the sample was ramped to 1400°C, in 60 slm of Ar flow

at 200 mbar to prevent additional growth of EG and promote the desorption of water and other molecules possibly on the EG surface after being exposed to air. The sample was then cooled to 1050°C prior to introducing H_2 into the reaction chamber. For the H-intercalation step, the H_2 gas flow is fixed at 80 slm while maintaining a pressure of 900 mbar for 60 minutes (Coletti et al., 2013). This process results in hydrogen passivation of the Si dangling bonds present at the top of the p-SiC(0001) epilayer, eliminating the covalent bonding between the epilayer and the first carbon layer, $6\sqrt{3}$ buffer layer, which now becomes quasi-freestanding EG forming an additional monolayer of EG. The polarization field from the hexagonal epilayer gives rise to a p-type charge density of ~1×10^{13} cm^{-2} in the quasi-freestanding EG, from ~5×10^{12}cm^{-2} n-type observed prior to intercalation (Riedl et al., 2009).

3.3.3 RESULTS AND DISCUSSION

It is previously reported (Coletti et al., 2013) that the hydrogen intercalation process converts buffer layer present at the EG and SiC interface into an additional graphene layer. The conversion of buffer layer into an additional graphene is confirmed by studying the 2D peaks widths of epitaxial graphene (EG) characterized using Raman spectroscopy, as shown below in Fig.3.5. As shown in fig 3.5(a), the Raman map of EG in the EG/SiC device before H-intercalation indicates the presence of 2-3 ML graphene (see side color scale in fig. 3.5(a)). The Raman map of the same EG layer after intercalation (fig. 3.5(b)) indicates the presence of a 3-4 monolayer graphene. The presence of an additional graphene layer in H-intercalated graphene is due to conversion of interface buffer layer into a free-standing graphene layer.

2D Peak Width   2D Peak Width
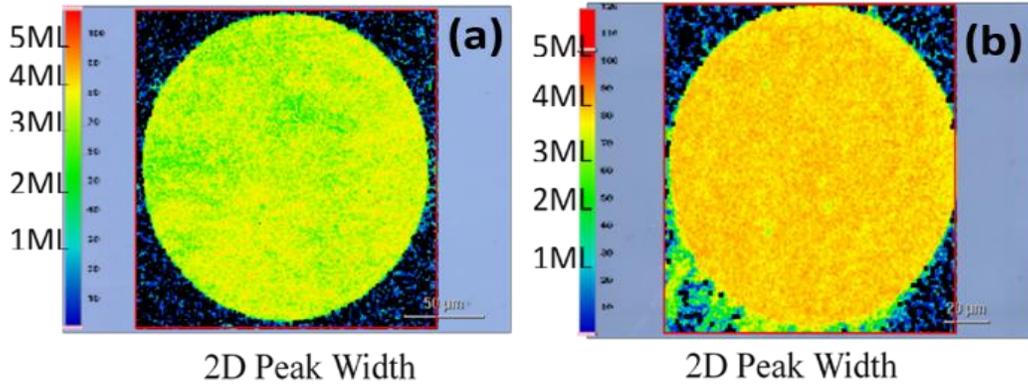
Figure 3.5 Measured 2D peak width of epitaxial graphene (EG) using Raman spectral measurements (a) before and (b) after H-intercalation. (See the side color scales for the thickness corresponding to each map).
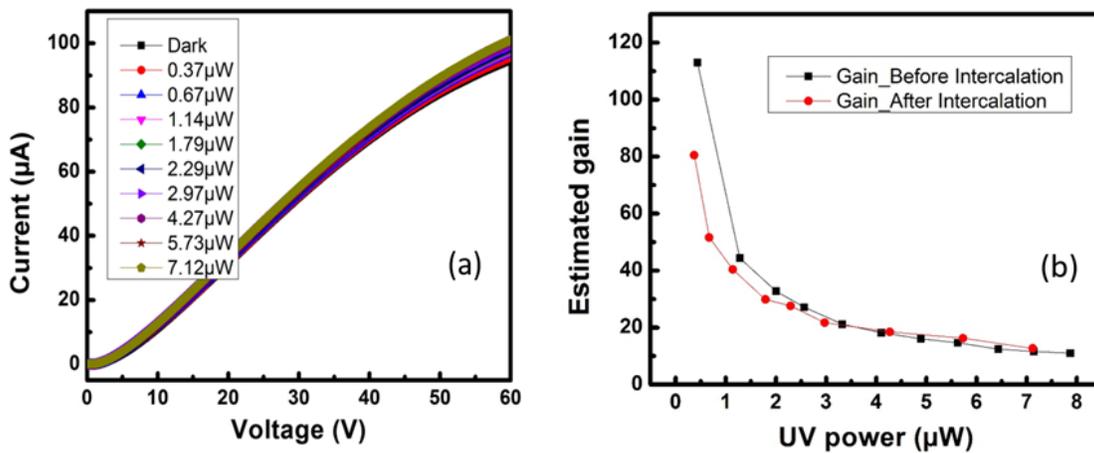
Figure 3.6 (a) Current(I_C)-Voltage (V_{CE}) characteristics of the device after intercalation under UV light (365 nm) (Also shown is the laser power in mW) (b) Comparison of estimated gain vs UV power before and after hydrogen intercalation.

The I-V characteristics of the H-intercalated EG/SiC device are recorded, by using the S1000 UV lamp, for different UV powers as described in section 3.2.2. Figure 3.6(a), shows the I_C-V_{CE} characteristics of the device measured after H-intercalation. From these I_C-V_{CE} curves, it is clear that after H- intercalation also, the collector current has increased with collector-emitter bias voltage (V_{CE}). The corresponding photocurrent gain values are

67

estimated, as the ratio of collector photocurrent to base current (see Equation 3.1), as explained in the previous section 3.2.2. The variation in estimated photocurrent gain with incident UV power is plotted is shown in Figure 3.6(b), for comparing the current gain before and after H-intercalation. As shown, for H-intercalated device, the estimated gain is decreased with increase in the incident UV power, which is consistent with the gain trend observed before H-intercalation. However, the gain at each UV power has decreased after H-intercalation. Since the gain in the SEPT is a consequence of minority carrier injection, this reduction in gain for H-intercalated devices can be attributed to reduced minority injection efficiency at the EG/SiC junction. This can be explained by considering the fermi-level shift due to H-intercalation step. As mentioned before, Fermi-level(E_F) in EG shifts below the Dirac point(E_D) due to hydrogen intercalation and thus lowering the barrier for holes that are being injected into the EG emitter region, thereby reducing the injection efficiency (see eq. below) and hence gain of the device.

$$\gamma = \frac{J_{\min}}{J_{\min} + J_{\maj}} \qquad (Eq.3.7)$$

3.4 PHOTORESPONSE MEASUREMENTS UNDER VISIBLE LIGHT(444NM) ILLUMINATION AND SPCM STUDY

In addition to the UV responsivity at 365nm (R_{365nm}) as discussed in section 3.2, another important metric for the comparison of UV detectors performance is the UV-Visible rejection ratio. The UV-Visible rejection ratio($R_{UV}:R_{Vis}$) is defined as the ratio of estimated responsivities under UV and visible light illuminations. In this section, the device characteristics under visible light (444nm here) are measured, and then compared with the characteristics under 365nm for estimating the UV-Visible rejection ratio.

68

For this purpose, the I-V characteristics of SEPT devices are measured by using a sub-bandgap visible light(444nm) source. Additionally, Scanning Photocurrent Microscopy (SPCM) with sub-bandgap excitation (444 nm) is used to map the spatial extent of the photocurrent response and examine the influence of localized polytypes on the sensitivity to sub-bandgap light. In this SPCM measurement technique, the local excitation spot is raster-scanned to identify spatial variations in photocurrents, which can be used to identify localized defects and examine characteristic length scales for carrier transport devices (Mueller, Xia, Freitag, Tsang, & Avouris, 2009). The spatial resolution of SPCM allows for clear representation of polytype heterojunctions, should they exist, and allows for us to discriminate between localized and homogenous origins of sub-bandgap response. By choosing to illuminate at 444 nm, we can resolve SiC polytypes that
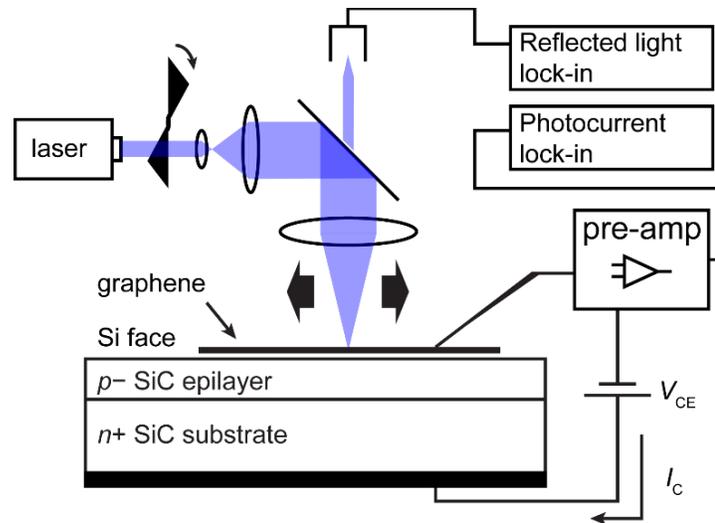
Figure 3.7 Schematic of SPCM setup for analysis of EG/SiC SEPT device. Voltage is applied through a tungsten probe arm contacted to the graphene surface. A pre-amplifier and lock-in amplifier are used to isolate the photocurrent signal at the frequency of the chopped laser light. The reflected laser signal is also captured and is used to map the physical features of the device.

exist in the visible absorption range, such as 8H-SiC (E_g=2.86eV).

The schematic of the measurement setup is shown in Figure 3.7. To form the SPCM images, a mechanically chopped, focused laser spot is scanned over the sample. Dual lock-in amplifiers allow for simultaneous recording and mapping of the resulting photocurrent and the specularly reflected laser beam, enabling good registry of SPCM maps with structural features. The photocurrent measured through the lock-in amplifier represents only the photocurrent that occurs at the same frequency as the scanned laser beam.

First, the measurement I_C-V_{CE} characteristics of the device are measured in SE mode (or graphene emitter), by focusing a visible blue laser (444nm) on to a fixed location(spot I_C-V_{CE}) in the graphene mesa region. The laser power is varied between 0.38mW and 3.8mW. The corresponding I-V test results are shown in Figure 3.8. As can be seen in Figure 3.8, there exists a non-zero photocurrent in addition to the dark current, due to blue photon absorption, in this device SE mode. Also, the photocurrent due to blue light is increased with an increase in laser power, indicating the device behavior is similar to that when illuminated by 365nm ultraviolet light.

Also, the UV-Visible rejection ratio, which is calculated as the ratio of responsivity of the device under UV light to the responsivity of the device under blue light, is estimated to be about 4.5×10^3 at V_{CE}=60V. This high UV-Visible rejection is comparable to the previously reported values and thus demonstrates these device structures could be a potential alternative to conventional metal electrode based SiC UV-detectors.
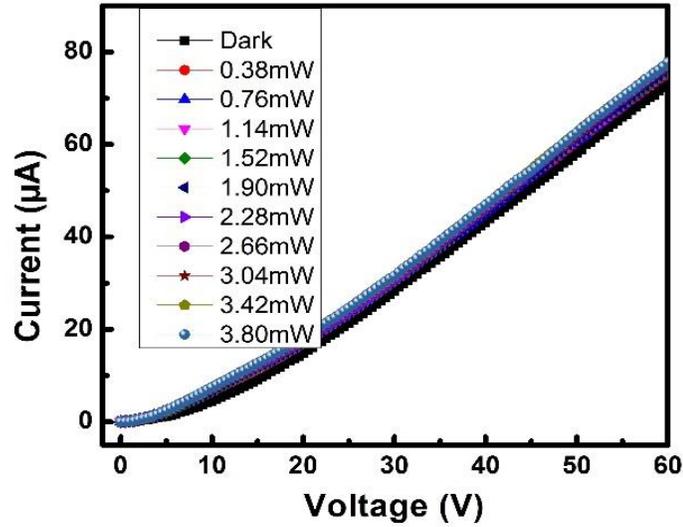
Figure 3.8 Current(I_C)-Voltage (V_{CE}) characteristics of SEPT under blue laser light (444 nm) illumination. The incident laser powers are also indicated.

There are several possible origins of sub-bandgap response, including heteropolytype junctions, donor-acceptor pair (DAP) absorption, and internal photoemission. The Franz-Keldysh effect can lead to sub-bandgap absorption but is not expected to play a large role here due to the modest electric field and indirect bandgap. SiC exists in several polytypes with varying band gaps. In this particular device, 4H-SiC (3.23 eV) is used to absorb UV light. Stacking faults in SiC manifest as other polytypes with smaller bandgaps, specifically 3C- (2.40 eV), 6H- (3.0 eV), or 8H-SiC (2.86 eV) (Mueller et al., 2009) which could lead to a spatially dependent visible response within the device area. A more homogenous contribution to sub-bandgap photocurrent is expected within the area of the EG contact from the other effects mentioned. Due to the large dopant ionization energies in SiC, DAP states have been shown to lead to luminescence and photoconductivity in the visible region (Mueller et al., 2009), (Mueller et al., 2009).

71

Thermal equilibrium between DAPs and band-edge states could give rise to carriers with a sufficient effective mobility to explain the transistor action.
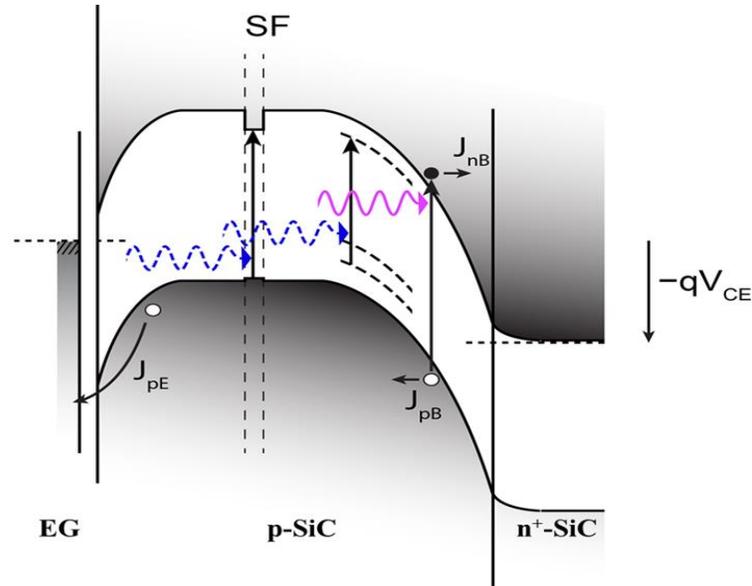
Figure 3.9 Band structure of the device in graphene emitter(SE) mode showing visible (dotted blue arrows) and UV (solid violet arrow) absorption mechanisms. Donor-acceptor pairs (DAP) create sub-bandgap states (dotted black lines) that also absorb visible light. Visible light can also be absorbed by stacking faults (SF) that shrink the bandgap, allowing longer wavelengths of light to be absorbed. UV absorption can also occur at SFs or DAP states, alongside bandgap absorption.

The homogeneous response under 444nm illumination, also described later by using SPCM maps, is attributed to absorption by DAP as shown in the band diagram below. In addition to the estimation of responsivity from spot I-V measurements under 444nm, photocurrent maps of the devices are recorded by raster scanning the laser beam, as described previously, across the selected area of the chip. Figures 3.10 and 3.11 show the SPCM image, as well as spot current-voltage (I-V_{CE}) curves, recorded for the same EG/SiC BJT device discussed in section 3.2.2, under 444 nm excitation. In this particular device (another 250µm diameter EG device on the same chip), the circular EG electrode has been

www.manaraa.com

scribed to form two separate semi-circular devices, as can be seen in the specular reflection map (Figure 3.10(a)). The SEPT devices generally display a large dark current at positive V_{CE} (graphene emitter mode), likely because the SiC *p-n* junction, which is at reverse bias
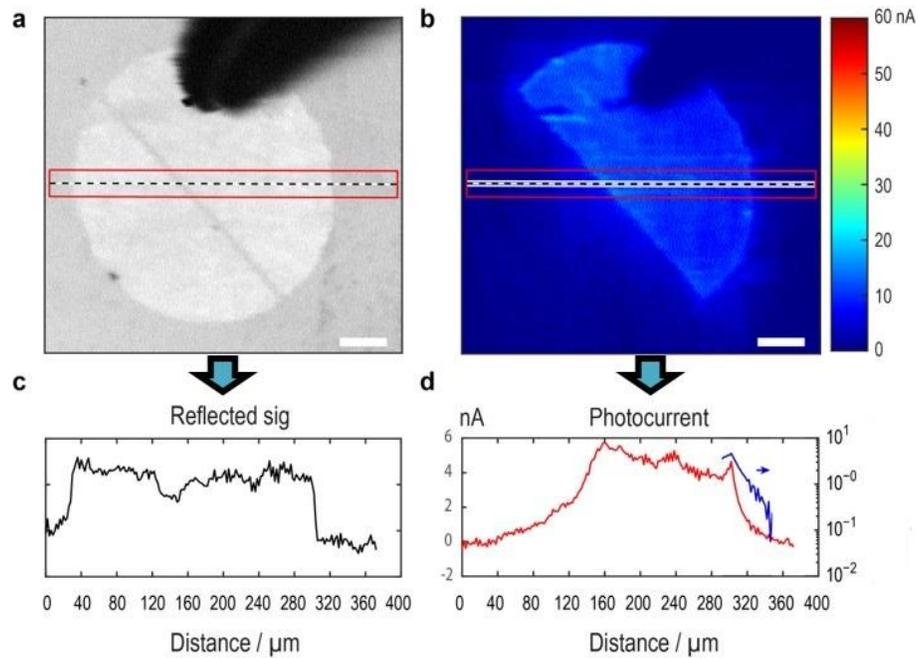
Figure 3.10 Simultaneously recorded reflected light(a) and AC photocurrent(b) maps of the EG/SiC phototransistor device in graphene collector (SC) mode under 444nm (sub-bandgap) excitation (V_{CE}=−10V, 2.24mW, chopped at 284Hz). The circular graphene electrode has been scribed to form two separate devices; photocurrent is only detected from the device contacted by the tungsten probe arm (dark shape at the top of images). Scale bars, 50μm. Signal profiles of the reflected light(c) and photocurrent(d) images along the lines indicated in (a,b). Signals are averaged in the orthogonal direction within the width indicated by the red boxes. Blue trace in d shows the near-exponential decay of the falling edge signal in the photocurrent profile.

in this condition, is poorly rectifying because it is not mesa isolated. In contrast, very little dark current ($\ll$ 1 nA) is observed at V_{CE} < 0 (graphene collector mode), suggesting a high degree of rectification at the EG/p-SiC Schottky junction.

Figure 3.11 shows the band diagrams for the device operation in EG emitter(a) and EG Collector(b) modes. Notably, a non-zero photocurrent is detected under 444 nm

73

illumination in both modes (Figures 3.10(c) and 3.10(d)), indicating that 444nm radiation is capable of exciting a base current. However, the maximum responsivity under 444nm is much smaller, by a factor of ~10^3, compared to maximum responsivity estimated under UV illumination previously (section 3.2.2). The photocurrent in graphene emitter mode is more than 100 times larger than for graphene collector, a contrast that is also observed under UV illumination of this and similar devices, suggesting a common carrier transport process for photocurrent appearing under visible and UV excitation.
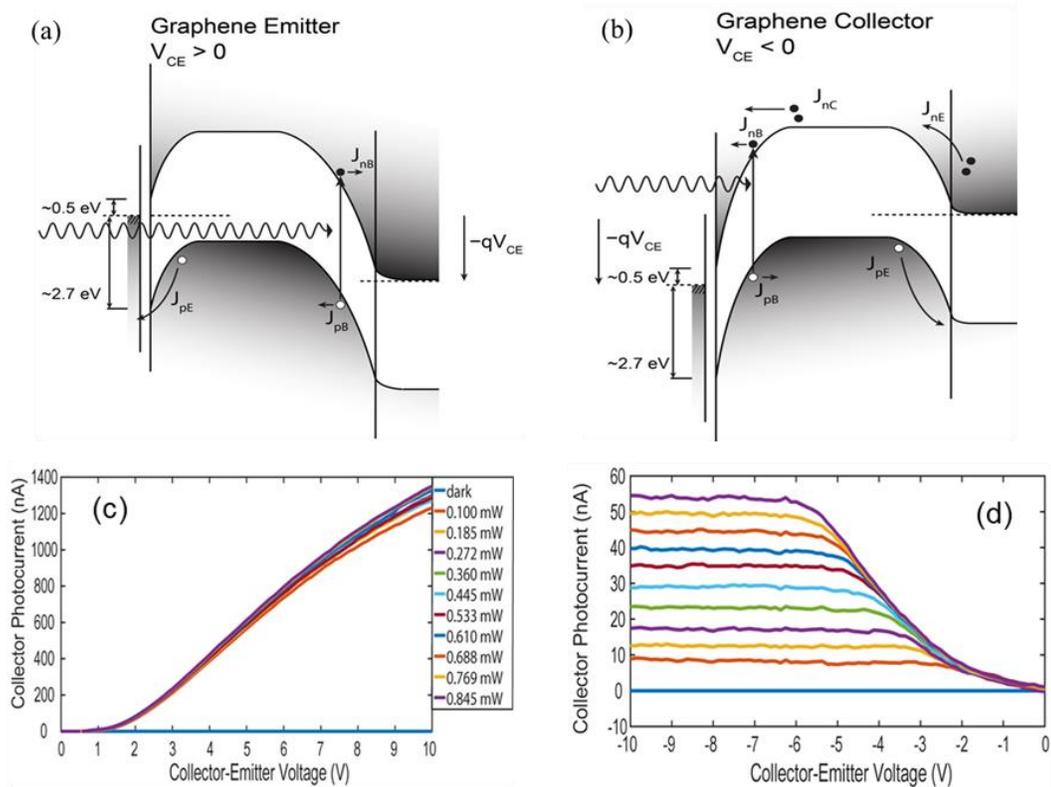
Figure 3.11 (a) Band diagram for EG/SiC phototransistor device operation in *graphene emitter mode* (V_{CE}>0). Electron-hole pairs are generated by light absorption. (b) Band diagram for EG/SiC phototransistor device operation in *graphene collector* mode (V_{CE}<0). I_c-V_{CE} characteristics of the device shown in Figure 3.10, measured in graphene emitter or SE(c), and graphene collector or SC(d) modes.

74

Figure 3.10(b) shows a representative SPCM map of this device recorded at $V_{CE} = -10V$ (graphene collector). The response is clearly seen to be strongly localized to the graphene electrode that is directly contacted by the probe arm. The fact that photocurrent is only collected from one of two devices in close proximity confirms the role of EG as a transparent and conductive emitter (or collector) contact in the device architecture. The high in-plane conductivity of the EG layer is illustrated by a flat response within the contiguous region. A similar pattern is observed in graphene emitter mode; however, the very low dark current and low gain in graphene collector mode results in detailed functional SPCM images. The edge of the EG region results in a sharp cutoff in the reflected signal of the device as seen in the profile plotted in Figure 3.10(c). In contrast, the edge of the corresponding photocurrent signal (Figure 3.10(d)) shows a measurable roll-off with distance with an approximately exponential profile. The logarithmic slope suggests a decay constant of about 10 µm.

In graphene-collector (SC) mode, a much smaller photocurrent is detected than for graphene-emitter, both under UV excitation and at 444 nm. Notably, the photocurrent signal profile (Figure 3.10(d)) shows that photocurrent generation is localized to the portion of the device connected to the probe arm, confirming the role of the EG/p-SiC junction in the function of the SEPT device. However, the large difference in responsivity between graphene collector and graphene emitter modes suggests that carrier transport may be strongly limited by recombination at the EG/p-SiC interface. In a bipolar phototransistor, the majority of base current generation occurs at the base-collector interface, as this region is depleted and possesses the largest electric field. Consequently, surface recombination is expected to much more strongly influence the gain in graphene-collector mode. Surface

75

recombination will also tend to limit lateral transport of electrons in the base over distances larger than the depletion width W_D (in graphene-collector mode) or base width W_B (in graphene-emitter mode). Consistent with this picture, the photocurrent response is more strongly localized in graphene-collector than in graphene-emitter mode.

Figure 3.12 shows the SPCM image of a different devices from the same chip. As shown here, in addition to the uniform blue response as seen in the other device, an additional AC photocurrent response localized in a triangular shape is observed both in SE and SC modes. However, there is no such feature observed in the reflected light image for this device. It is important to note that this localized response is not significantly high when
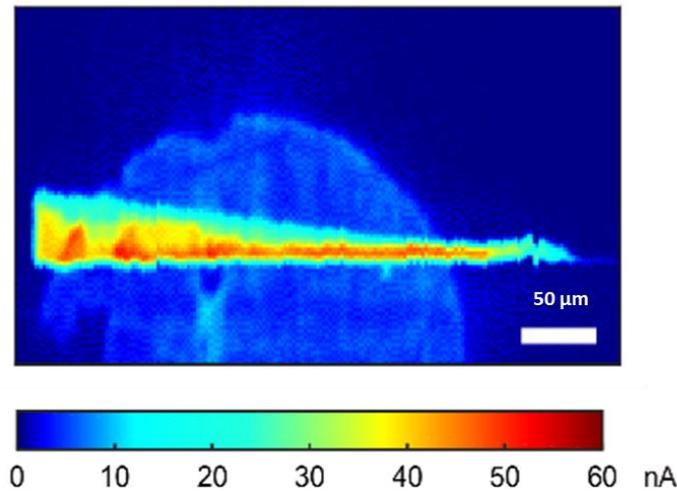
Figure 3.12 AC photocurrent map of a different device on the same chip, measured in SC mode, showing an enhanced blue response locally in addition to the absorption due to DAP observed across the scanned region.

compared to visible light response, resulting in high visible-rejection ratio. Further, the localized nature of the feature and the flat background makes it look prominent in the SPCM map. A triangular feature like stacking fault(SF)s are generally formed when a BPD propagates from the substrate into the epilayer during the growth. In general, BPDs can

76

nucleate as either 3C-SiC (E_g=2.36eV) or 8H-SiC(E_g=2.86eV) polytypes during the epitaxial growth process.

Since a blue laser light(444nm) is used here in this study, the local feature observed in photo-response map could be attributed to absorption by 8H-SiC stacking fault. Also, the stacking fault feature is elongated in the down-step direction supporting our assumption that this is a stacking fault. Finally, the stacking fault feature length(L) is calculated as the projection of epi-layer onto the surface, using the equation below (Kimoto & Cooper, 2014):

$$L \approx \frac{d_{epi}}{\tan \theta} \qquad \text{(Eq.3.8)}$$

,where, d_{epi} is the thickness of the epilayer which is 30µm, and θ is the substrate off-cut angle which is 4 degree. The stacking fault length obtained using these values is 400µm which agrees well with the length observed in the SPCM map confirming the presence of 8H-SiC stacking fault in the epi-layer. Therefore, the enhanced blue photo-response is attributed to 8H-SiC stacking fault present in the active area of the device. This sub-bandgap absorption due to SF is also shown in the band-diagram in Figure 3.9.

3.5 SUMMARY

In summary, vertical heterojunction bipolar phototransistors are fabricated with EG/ p-SiC/ n^+-SiC as emitter, base and collector layers in the respective order. The current-voltage characteristics of this device is tested under UV light for its application in UV detectors. From these I-V characteristics, gain values are estimated for different UV illumination powers at 365nm. The highest gain value is found to be 113 and also responsivity values as high as 7.1 A/W are observed under 0.43 µW illumination at V_{CE}=60

V bias voltage. We argue that the gain in this bipolar phototransistor device is a result of a two carrier transport across the EG/SiC junction, contrary to the general assumption that as a Schottky junction, it is expected to show thermionic emission due to majority carriers. Later the graphene/SiC interface is intercalated using H2 gas and characterized to study the effect of H-intercalation on the device behavior. It is confirmed from the I-v test results, the gain and hence responsivity of the H-intercalated devices are less compared to the device with as grown graphene. This reduction in gain (or responsivity) is attributed to reduction in minority carrier injection efficiency caused by barrier height increase due to fermi-level shift in EG after H-intercalation. A UV-Visible rejection ratio$>10^3$ is estimated for these devices by studying the device I_C-V_{CE} characteristics under blue laser light illumination. Sub bandgap response is confirmed by SPCM maps and is attributed to blue photon absorption by DAP present in 4H-SiC.

Since the EG/SiC UV detector operates as a bipolar phototransistor, high gain values can be achieved even at low bias values by optimizing the epi-layer thickness and doping. The thinner SiC epilayer (base) in this device structure will lead to enhanced base transport factor and gain. Also, the dark current can also be reduced significantly by mesa isolating the base.

CHAPTER 4

HIGH DETECTIVITY VISIBLE-BLIND TETRAFLUOROSILANE (SIF$_4$) GROWN EPITAXIAL GRAPHENE/SIC SCHOTTKY CONTACT BIPOLAR PHOTOTRANSISTOR[1]

4.1 INTRODUCTION

In chapter 3, high responsivity UV detectors based on EG/SiC bipolar junction transistors were demonstrated by using transparent EG window at the top to minimize the reflection/absorption losses caused by metal electrodes in conventional UV detectors. This device, in Schottky Emitter(SE) mode of operation, showed a high responsivity(R)=7.1A/W at 365nm due to EG/p-SiC Schottky injection leading to high bipolar gain. However, this device suffered from large dark current due to lack of mesa isolation at the p-SiC/n$^+$-SiC (base/collector) junction. Moreover, this device did not show appreciable gain in the Schottky collector (SC) mode (Barker, Chava, Daniels, Chandrashekhar, & Greytak, 2017). The large dark current in these devices will result in high noise equivalent power (NEP) and low detectivity etc., and therefore are impractical for post-Si UV detection applications.

In this chapter 4, a new device with a vertical device (EG/p-SiC/n$^+$-SiC) structure, similar to the BJT structure discussed in chapter 3, is used to study its UV detection characteristics. A thinner p-SiC base (13μm) epilayer is used in these new BJT devices to improve the base transport factor and thus current gain. Remember in EG/SiC BJT, as discussed in chapter 3, the bipolar gain is a consequence of equivalence of electron injection from EG into p-SiC base layer in forward active mode of operation (Chava, Omar, et al., 2016). Additionally, EG is grown using a new SiC homoepitaxy-compatible (Tawhid Rana et al., 2015) SiF$_4$ gas precursor. In this growth technique, as discussed in chapter 2, graphene layers can be grown on SiC in a controlled manner. As described in chapter 1, the UV responsivity(R), UV-Visible rejection ratio, speed, NEP and specific detectivity(D^*) are the important figures of merit for UV photodetectors. In this chapter, comprehensive characterization of this new TFS grown EG/SiC phototransistor including spectral responsivity, speed, noise equivalent power (NEP) and detectivity will be discussed, and these performance metrics are compared with other visible-blind UV detector devices reported in the literature.

4.2 DEVICE FABRICATION AND CHARACTERIZATION

For the phototransistor device fabrication, the 13µm thick p-SiC base epilayer is grown on 8° offcut n$^+$-4H-SiC (0001) substrate by CVD reactor using dichlorosilane(DCS) and propane in hydrogen ambient at 300 Torr and 1600^{0}C at a C/Si ratio of 1.9 (Song, Chandrashekhar, & Sudarshan, 2014), giving a growth rate of ~26 µm/hr for 30 mins, producing a 13 µm thick film as determined by Fourier transform infrared reflectance (FTIR). The resultant doping of the epilayer, due to site-competition epitaxy(Larkin et al., 1994), was found to be p-type 3.7×10^{14} cm^{-3} by Hg-probe capacitance-voltage (C-V)

80

measurement. This thickness was based on our previous work (Chava, Omar, et al., 2016), where ~10μm diffusion length was measured in the 30μm base(Barker et al., 2017). Thus to improve the base transport factor, and hence, the current gain, a thinner layer was used, although this always comes at the expense of lower light absorption for long wavelengths (~30μm for λ=365nm, as in (Chava, Omar, et al., 2016), (Barker et al., 2017). To achieve reasonable absorption in the range 250-400nm (Sridhara, Eperjesi, Devaty, & Choyke, 1999), while maintaining adequate current gain, the 10μm base thickness range was chosen, with the resultant 13μm obtained for our standard 30min growth.

The EG top electrode layer is then grown on the SiC base at 1600^0C and 300 Torr, in the same reactor, using SiF_4 precursor in Argon for 10 minutes using a chemically accelerated Si-removal process developed at our lab(Tawhid Rana et al., 2015). From FTIR and X-ray photoelectron spectroscopy (B. K. Daas, Daniels, Sudarshan, & Chandrashekhar, 2011), the thickness of the EG is estimated to be ≈ 15 monolayers for these growth conditions. Circular graphene regions of diameter 250 µm are defined for the device, using photolithography followed by O_2 plasma reactive-ion etching (RIE).

Figure 4.1 shows the schematic and band diagrams of the vertical bipolar phototransistor device using EG/p-SiC/n$^+$-SiC layers. As shown in this figure 4.1, the device is operated in two different modes, namely Schottky emitter (SE) and Schottky collector (SC) based on the polarity of the bias applied at the top EG layer. The device is said to operate in SE mode, when the EG/p-SiC junction is forward biased and the p-SiC/n$^+$-SiC junction is reverse biased (Fig. 4.1(b)). On the other hand, the device is said to operate in SC mode when the EG/p-SiC junction is reverse biased and the p-SiC/n$^+$-SiC junction is forward biased (Figure 4.1(c)). When light is incident on the device from top
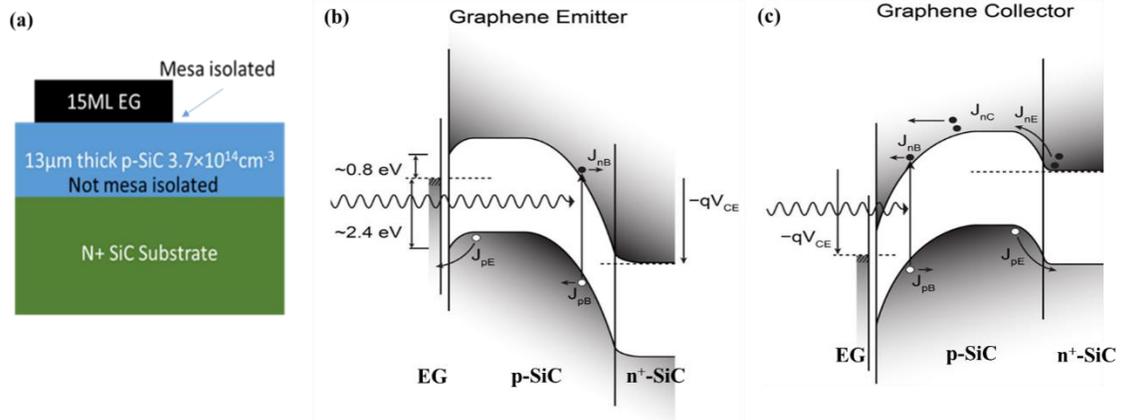
Figure 4.1 (a)Schematic of EG/p-SiC/n$^+$-SiC bipolar phototransistor device structure. Energy band diagram showing the phototransistor device operation in Schottky Emitter(SE)(b) and Schottky Collector(SC)(c) modes under light illumination.

i.e. from EG side, the incident light photons will be absorbed by the SiC epi layers and substrates. Therefore, e-h pairs will be created in these layers due to the photon absorption by SiC. These e-h pairs will be separated by the electric fields in the base-collector depletion regions in SE and SC modes. Also, as discussed in chapter 3, this device is expected to show a bipolar gain due to minority carrier injection from EG to p-SiC in SE mode. Similarly, in SC mode, the device can show a bipolar gain due to carrier injection from n$^+$-SiC substrate in to p-SiC base epilayer. It is important to note that the EG is mesa isolated resulting in smaller junction area for the EG/p-SiC Schottky junction compared to the p-SiC/n$^+$-SiC junction which forms a large area p-n junction as the p-SiC (base) epilayer is not mesa isolated. Later, in this present chapter 4, we will discuss the effects of the B-C junction area on the current-voltage characteristics of the device current(I_c) in both modes. As discussed in chapter 2, we note that the Schottky barrier height for the EG to n-SiC is 0.8eV, as measured by C-V on EG/n-SiC Schottky test structures (Balachandran, 2017),

82

and is higher than the 0.5eV barrier height reported for thermally grown EG/SiC junctions (Coletti et al., 2010), (Coletti et al., 2013).

4.3 SPECTRAL RESPONSE AND SPCM STUDY

The current-voltage (I_C-V_{CE}) characteristics of the device are measured in the dark and under light for both SC and SE modes, by illuminating the device using a monochromatic light. A monochromatic light source (10nm bandpass) is used to vary the wavelength of incident light for these measurements. The action spectra (or spectral response) are reconstructed using the measured I_C-V_{CE} characteristics at each wavelength where the responsivity is calculated for each wavelength as discussed in chapter 3. The band diagrams for the device operation in SE and SC modes are shown in figures 4.1(b) and 4.1(c) in the respective order.

As shown in Figures 4.2(a) and 4.2(b), a dark current of 230pA and 670nA is observed at V_{CE}=20V in SC and SE modes respectively. The significantly larger dark current in SE-mode is due to the absence of mesa isolation at the 10μm deep *backside* SiC p-n junction, which is 1cm^2, compared to the ~4.9×10^{-4}cm^2 area of the graphene/SiC Schottky top junction (Figure 4.1), leading to a corresponding increase in leakage area. However, the dark current in the SE-mode devices, 670nA, was still 3 orders of magnitude lower than the 100μA observed in our previous devices (Chava, Omar, et al., 2016). This decrease in dark current is attributed to smaller thickness of the epi-layer and also significant optimization of our SiC epitaxy which has led to defect reduction in our epilayers (Balachandran, 2017). Mesa-isolation of the base p-SiC epilayer should

83

significantly reduce the leakage (dark) current at the SiC pn junction (B-C junction) in SE-mode to values comparable to SiC pn diodes (Table 4.1).

Clear bipolar phototransistor action is seen in both SC and SE-modes (Yang, Nohava, Krishnankutty, Torreano, McPherson, et al., 1998). In SE-mode, the current increases starting at $V_{CE}=2V$, in agreement with the 2.4eV EG/ p-SiC Schottky barrier estimated above (Figure 4.1). For SC-mode, the bipolar behavior is seen until $V_{CE}\sim10V$ (Figure 4.2(a)) beyond which the photocurrent increases sharply due to avalanche effects from electric field concentration at the reverse-biased EG/SiC Schottky barrier periphery (Baliga, 2008). In SE-mode, the B-C is a large area junction and there is no periphery due to the lack of mesa-isolation, so avalanche breakdown at the device periphery is not seen. Further, as explained in chapter 3, the avalanche breakdown for SiC B-C junction may not happen at low bias voltages$<10^2V$ ($V_{CE}=20V$ here). This assertion is clearly supported by scanning photocurrent microscopy (SPCM) maps at 444nm (Figure 4.2(a)) (Barker et al., 2017), where 'hot-spots' are seen in SC-mode at the periphery that increase in prominence at higher V_{CE}, in concurrence with the sharp current increase in the photocurrent, whereas similar features are not observed in SE-mode. The uniform ring/halo at the device edge in SE-mode is due to non-specular scattering at that edge, leading to greater photocurrent in the non-mesa isolated SiC pn junction collector. It is evident, however, that the hot-spots seen in SC-mode are not visible in SE-mode, showing that sharp increase in current in SC-mode at $V_{CE}>10V$ is due to avalanche from the device periphery. This avalanche effect may be minimized by using field-plate techniques (Baliga, 2008), although careful engineering may allow it to be exploited as in avalanche photodiodes (J.C. Campbell, 2007).

84

In the SE-mode I-V curves under illumination (Figure 4.2(b)), a small hump is seen near ~0.7V, which is attributed to the presence of a Schottky barrier height from the edge, in addition to the larger one from the bulk (Figure. 4.1). As the emitter-base junction turns on, the influence of the parasitic smaller barrier is eventually overwhelmed by the bulk owing to the much larger area associated with the higher barrier. This could be due to independent contributions from bulk and periphery of the graphene contact, in analogy to SC- mode results where edge and bulk clearly give independent contributions.
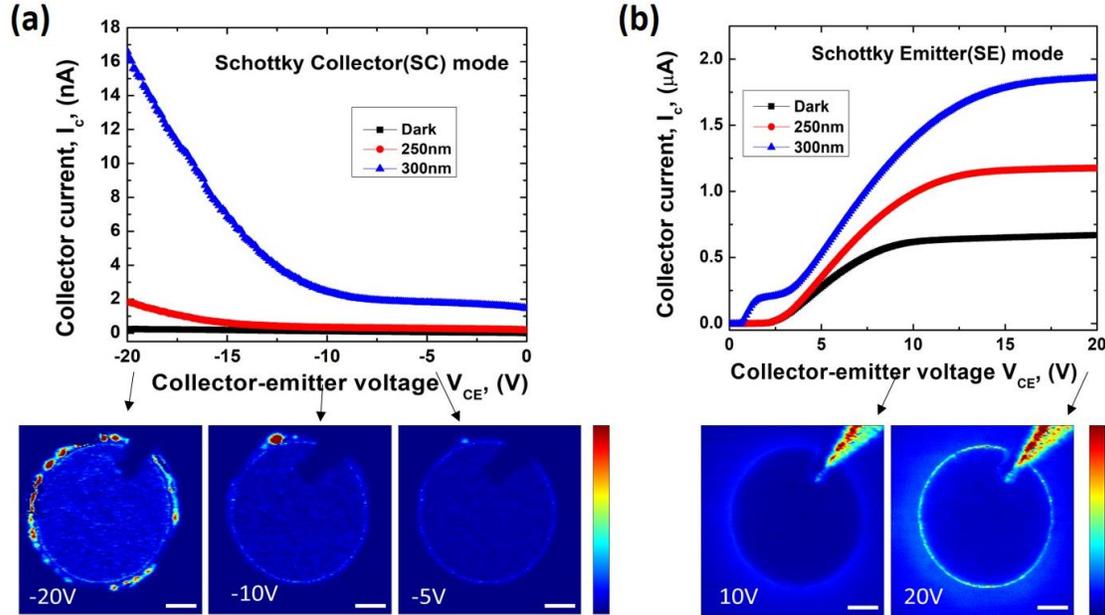
Figure 4.2 Experimentally measured *dark and light (250nm and 300nm)* current-voltage(I_C-V_{CE}) characteristics of the device in *SE*(a) and *SC*(b) modes. The corresponding *scanning photo-current maps (SPCM)* of these devices measured at different bias(V_{CE}) voltages) under 444nm laser illuminations are also shown. (For SPCM maps, the scale bar (in white) is 50 µm and the current scale is shown in color on the right, with a maximum value of 400pA).

Larger absolute photocurrents(I_c) are seen in SE-mode, again due to the absence of mesa-isolation in SE-mode, since the circular spot size of the light from the spectrometer

85

is ~1cm^2. This means that in the SE-mode, the e-h pair collection area is $>>4.9\times10^{-4}$cm^2 area of the graphene/SiC junction, whereas it will be comparable to this area in SC-mode, leading to the apparent large difference in photocurrents, despite the similar responsivities. *R(λ)*, reported in Figure 4.3. *R(λ)* is defined as the ratio of the observed photocurrent (difference of current under illumination and in the dark) to the optical power incident on the device. *R(λ)* was measured under wide area illumination by comparison to a calibrated Si photodiode. To account for the difference in collection area discussed above, the absolute responsivity, *R*, was calibrated to measurements performed with 365nm illumination through a microscope focused to an area < the device area. The *R(λ)* values are higher than expected from 100% quantum efficiency (dashed line in Figure. 4.3) for above bandgap (~390nm for SiC) light illumination, indicating current gain in both SE and SC-modes. Note that, the spectral responsivity($R(λ)$) corresponding to 100% quantum efficiency (η=1) is commonly used as a reference to compare the spectral responsivities of different photodetectors, and it is independent of the bandgap of the semiconductor material and is calculated by Equation. 4.1. A peak R(250nm)=25 A/W is observed in SE-mode which corresponds to current gain *g* >120, as given by (E Monroy, Omnes, et al., 2003);

$$R(\lambda) = \frac{\lambda\eta}{hc}qg = \frac{\lambda(nm)}{1.24\times10^3}g \qquad \text{(Eq.4.1)}$$

where, *R* is the measured responsivity (in A/W), λ is the incident light wavelength, h is Planck's constant, c is the light velocity, q is the electron charge, where a quantum efficiency, η=1 is assume to estimate a lower bound on *g* in the final expression in Equation 4.1. In SC-mode, a peak *R*(270nm)=17 A/W is measured, corresponding to *g*>78 although as discussed above, this is due to a combination of bipolar gain, and avalanche gain from

86

the device periphery at V_{CE}=20V. At V_{CE}<10V, avalanche gain from the periphery is effectively suppressed, and R is also reduced, leading to bipolar current gain, g~10. In SC-mode, the short absorption lengths in SiC (Sridhara et al., 1999) ($\approx$1μm at 270nm) for short wavelength photons results in lower R due to the recombination of the photogenerated carriers (X. Chen et al., 2007) at the EG/SiC Schottky collector junction. In a long-base bipolar device, where minority carrier injection efficiency ~1 is assumed, and that g is limited by base transit, the recombination time, τ_{rec} is estimated from (Sze & Ng, 2006):

$$g \approx \frac{2D_n\tau_{rec}}{W_{QNR}^2} \qquad \text{(Eq.4.2)}$$

, where W_{QNR} is the quasi-neutral region width at a given voltage from the difference in the base-width and the depletion region at the collector side, and D_n=23cm^2/Vs is the diffusivity of electrons in SiC(Kimoto & Cooper, 2014). This leads to τ_{rec}~20ns in both SE and SC-modes. In SC-mode, the recombination velocity, S at the EG/SiC interface is estimated from W_{QNR}/ $\tau_{rec}$$\approx$10^{5}cm/s at V_{CE}=10V, which is in excellent agreement with that estimated for sub-bandgap illumination previously (Barker et al., 2017) in chapter 3.

The UV-visible rejection ratio, R(270nm)/R(400nm) is better in SC-mode ~5.6$\times$10^3 compared to ~12.3 in SE-mode. The poor visible rejection in SE-mode is attributed to absorption of sub-bandgap light by donor acceptor pairs (DAP) (Barker et al., 2017) present in the highly doped n$^+$-SiC substrate, but not in the low-doped p-SiC, since the collection region in this mode spans the n$^+$-substrate unlike the SC-mode. The contribution of stacking faults to the sub-bandgap response in SE-mode is excluded, shown in our previous devices (Barker et al., 2017), as the SPCM maps show no evidence of this (Figure 4.2). The $R(\lambda)$ and UV-visible rejection values are compared with other wide bandgap

photodetectors in Table 4.1, where the present EG/SiC phototransistor device compares well. Here, it is also important to note that the high responsivity is achieved in the present devices at relatively low bias voltages 20V compared to high voltages (>100V) for the avalanche photodiodes (Bai, Guo, McIntosh, Liu, & Campbell, 2007).

Figure 4.3 A plot for the comparison of spectral responsivity from 250-450nm for the TFS grown EG/SiC(13µm thick) heterojunction phototransistor device in SE and SC modes of operation at V_{CE}=20V.

4.4 TRANSIENT RESPONSE AND DARK NOISE MEASUREMENTS

The response times and dark noise spectrum were measured using a virtual-ground transimpedance current pre-amplifier to convert the dark and photo-induced currents to a voltage. This output voltage signal was visualized on an oscilloscope in the time domain for the turn ON/OFF transient response times, and was converted into the frequency domain using the Fast Fourier Transform (FFT) function for the noise power current density ($S_n(f)$) measured as a function of frequency in the dark. The response times were measured at 320nm (largest absolute photocurrent) by mechanically chopping the light,

88

and fitting the resultant output with exponential decay/growth functions for response times (Figure 4.4). The photocurrent rise and decay responses under 320nm illumination are fitted using the equations:

$$y = y_0 + A_1*exp(x/t_1) + A_2*exp(x/t_2) \qquad \text{(Eq.4.3)}$$

$$y = y_0 + A_1*exp(-(x-x_0)/t_1) + A_2*exp(-(x-x_0)/t_2) \qquad \text{(Eq.4.4)}$$

where, t_1 and t_2 represents the slow and fast time constants related to active and non-active areas of the device.

Figure 4.4 Turn ON and OFF transients of the EG/SiC phototransistor device measured in SE(a) and SC(b) modes under 320nm illumination.

In SC-mode, ON/OFF response times of 10ms/47ms are extracted, whereas in SE-mode, ON/OFF response times of 46ms/730ms are extracted. These values are significantly slower than the τ_{rec}=20ns estimated above, likely due to RC delays, as also seen at low collector currents in Si bipolar phototransistors (Kostov, Gaberl, & Zimmermann, 2013). This assertion is supported by the fact that the response time is slower in SE-mode, where the collector is a much larger area, leading to a large collector capacitance compared to SC-mode. Mesa-isolation of the base-collector SiC pn junction is expected to improve the response time in SE-mode. Faster response times should also be observable at higher light levels.

Figure 4.5 Experimentally measured noise spectrum of the device at V_{CE}=20V in Schottky Emitter (SE) mode in the frequency range of 1-100Hz.

Figure 4.5 shows the measured noise power density $S_n(f)$ (in A^2/Hz) in SE mode at V_{CE}=20V, along with the noise floor at this preamplifier gain setting. As shown in Figure 4.5, the noise power density decreases linearly with frequency, indicating 1/f flicker noise

90

in SE mode, and reaches the measurement limit at frequencies >1kHz. We do not observe a crossover to a shot-noise limited regime in our measurements. Typically Shot noise is dominant noise source at low temperatures and high frequencies. In SC-mode, on the other hand, the dark current was only 230pA. The noise power density in SC was measured to be $<10^{-28}A^2$/Hz, the noise threshold at the corresponding pre-amplifier setting, and a 1/f regime was unmeasurable with our measurement setup.

The dark noise spectral density is, therefore, estimated for the shot noise using $S_n(f)=2eI_c(dark)$ (Osinsky, Gangopadhyay, Yang, et al., 1998) for the SC-mode. At $V_{CE}=20V$, white noise density $S_n(f)\approx6\times10^{-29}A^2$/Hz, is used for estimation of the noise equivalent power (NEP) below. The NEP is defined as the minimum optical power that can be detected by at the given noise level. From the measured current noise power density spectrum, $S_n(f)$ (Figure 4.5), NEP, is extracted. For a bandwidth of B, the total square noise current is given by:

$$< i_n^2 > = \int_0^B S_n(f)df = \int_0^1 S_n(1)df + \int_1^B S_n(f)df \qquad \text{(Eq.4.5)}$$

, where we assume that the value at 1Hz is assumed to be flat until 0Hz in the first integral on the RHS as is commonly done (Osinsky, Gangopadhyay, Lim, et al., 1998), (Gundimeda et al., 2017)'(Q. Chen et al., 1997). The noise equivalent power (NEP) is then estimated using the equation:

$$NEP = \frac{\sqrt{\langle i_n^2 \rangle}}{R} \qquad \text{(Eq.4.6)}$$

where R is the responsivity (in A/W) of the device. Here, the highest value of R (see Figure 4.3) is used for the estimation of NEP in both SE and SC modes.

91

Specific detectivity(D^*) is another figure of merit for the photodetector. It is obtained by normalizing the NEP with the detector area and the bandwidth. From the NEP, the specific detectivity (D*) is calculated using the equation:

$$D^* = \frac{\sqrt{A \times B}}{NEP}$$ (Eq.4.7)

where A is the device area in cm^2, B is the bandwidth of the photodetector in Hz. Given that the response time is 47ms in the SC-mode, a bandwidth of 20Hz is assumed, giving NEP=2.3fW and $D^*= 4.4 \times 10^{13}$ Jones. Similarly, since the response time in the SE-mode is 730ms, a 1Hz bandwidth is assumed, giving NEP= 3.3×10^{-12} W and $D^*=9.5 \times 10^9$ Jones.

These values compare favorably with other visible-blind detectors (Table 4.1). Mesa-isolation of the base-collector SiC pn junction should reduce the active device area to $\sim 4.9 \times 10^{-4} A/cm^2$, leading to a reduction of dark current to <270pA from 670nA assuming the same leakage current density, pushing the NEP to <2fW. The response time should also improve as discussed above, with a corresponding increase in B, and consequently, the specific detectivity (D^*)

4.5 SUMMARY

In summary, vertical bipolar EG/SiC bipolar device structures similar to that discussed in chapter 3 are fabricated. The p-SiC epilayer used in this device structure is thinner (13µm) compared to 30 µm thick epilayer previously used. Also, the EG used for the present devices is grown by selective etching of Si from SiC epi-layer by using TFS gas precursor. These TFS grown EG/SiC UV phototransistor devices are characterized for spectral responsivity, response speed, NEP and specific detectivity(D^*).

Table 4.1 Comparison of the TFS grown EG/SiC phototransistor performance metrics with previously reported ultraviolet detectors.

Device type	Voltage (V)	Dark current	Responsivity (R) at 270nm (A/W)	Visible rejection (R_{270} : R_{400})	Response time	NEP(W)	Specific Detectivity, D* (Jones)
EG/SiC BJT (SC mode)	20	230pA	17	5.6×10^3	10ms(On) 47ms(Off)	2.3×10^{-15}	4.4×10^{13} (BW=20Hz)
	10	100pA	2.2	2.2×10^2	N/A	1.1×10^{-14}	8.6×10^{12} (BW=20Hz)
	5	55pA	1.1	4×10^2	N/A	1.7×10^{-14}	5.8×10^{12} (BW=20Hz)
EG/SiC BJT (SE mode)	20	670nA	25	12.3	46ms(On) 730ms(Off)	3.3×10^{-12}	9.5×10^9 (BW=1Hz)
SiC pin diode[1]	20	<0.5pA	0.13	$>10^4$	N/A	N/A	N/A
SiC Schottky[2]	5	8pA	~0.09	$>10^3$	N/A	N/A	N/A
SiC APD[3]	144	5pA	93(at 280nm)	N/A	N/A	20×10^{-15}	6.4×10^{13} (BW=1KHz)
GaN Schottky[4]	1.5	34nA	~0.07	$>10^2$	150ns	3.7×10^{-9}	N/A
AlGaN Schottky[5]	1.35	7nA	~0.07	N/A	1.6 µs	6.6×10^{-9}	N/A
AlGaN photodiode[6]	0.5	0.1pA	~0.01	2.6×10^3	<0.4µs	N/A	N/A

[1] (X. Chen et al., 2007), [2] (Mazzillo et al., 2009), [3] (Bai et al., 2007), [4] (Osinsky, Gangopadhyay, Yang, et al., 1998) [5] (Osinsky, Gangopadhyay, Lim, et al., 1998), [6] (Sakib Muhtadi, Hwang, Coleman, Lunev, et al., 2017)

The device performance of the visible-blind EG/SiC phototransistor is compared in SE and SC modes. UV-visible rejection ratio (R_{270}:R_{400}) >10^3 is achieved, with responsivity ~17-25A/W at low voltages (V_{CE}=20V). This responsivity is shown to arise from both bipolar gain as well as avalanche from the device periphery in SC-mode. The UV-visible rejection ratio in SE mode, however, is compromised by DAP present in the SiC substrate. The response times of these devices are relatively slow, 10ms-730ms, compared to low responsivity photodiodes. Finally, the NEP=2.3fW and D^*=4.4×10^{13}Jones indicates excellent performance of these devices both in SE and SC modes and comparable to the state-of-the-art.

94

CHAPTER 5

HIGH RESPONSIVITY $Al_{0.85}Ga_{0.15}N/Al_{0.65}Ga_{0.35}N$ HIGH ELECTRON MOBILITY TRANSISTORS (HEMT'S) FOR SOLAR-BLIND UV DETECTION[5]

5.1 INTRODUCTION

As explained in chapter 1, the UV radiation can be classified into different regions according to the wavelength. These include UV-A(315-400nm), UV-B(280-315nm), UV-C (200-280nm) and vacuum UV(10-200nm). Further, the long wavelength cut-off(λ_{cutoff}) for photon absorption in optical detectors is determined primarily by the bandgap of the semiconductor materials used to fabricate them. For instance, WBG materials 4H-SiC(E_g=3.26eV) and GaN(E_g=3.4eV) have absorption cut-offs at 388nm and 365nm (both in UV-A region), in the respective order, and therefore these material systems are suitable for visible-blind UV detectors. Visible-blind UV detectors are the detectors that generates a photocurrent by absorbing photons of wavelengths only below 400nm (i.e. UV photons). Similarly, there exists another category of photodetectors called as solar-blind UV detectors with absorption cut-off below 290nm, i.e, these detectors generate a photocurrent only by the absorption of photons of wavelengths <290nm.

---

[5] Venkata S. N. Chava, S. Muhtadi, S. Hwang, A. Coleman, F. Asif, G. Simin, MVS Chandrashekhar, and A. Khan. To be submitted to Applied Physics Express.

There are emerging applications that require high responsivity UV detectors with solar blindness i.e. only responsive to light with wavelength <290nm (H. Chen et al., 2015). These include furnace gas control systems, as well as aerospace and harsh environment detection systems that require the sensing of the UV emission from plumes,or for flame detection for firefighters, in the presence of large amounts of visible and IR radiation. In the parlance of healthcare[1], one must be able to distinguish UVA light (relatively harmless λ>315nm) from UVB and UVC light (cancer causing, used in water disinfection to kill bacteria λ<315nm).

The key metric used to describe photo detectors is responsivity, $R(\lambda)$ i.e. number of amperes of electrical photocurrent, I_{ph}, in response to each Watt of incident optical power, P_{opt} at a given wavelength, λ (Sakib Muhtadi, Hwang, Coleman, Lunev, et al., 2017):

$$R(\lambda) = \frac{I_{ph}(\lambda)}{P_{opt}} = \frac{I(\lambda) - I(dark)}{P_{opt}}$$ (Eq.5.1)

Currently, the most commonly used photodetectors at UVC wavelengths are traditional narrow-gap semiconductors such as Si-photodiodes, which suffer from $R<0.3$A/W, and require expensive filters to achieve solar-blindness. On the other hand, for high-end applications, photomultiplier tubes (PMT) offer high responsivity, but require high voltage >1000V, necessitating bulky, expensive power supplies. While $R(\lambda)$ is the most commonly used metric to quantify photodetector performance, with the understanding that higher gain gives better sensitivity, this is not always sufficient. For example, large dark currents in a transistor on-state gives large shot noise power(explained later in this chapter), compromising the sensitivity of the device(Colace, Ferrara, Assanto, Fulgoni, & Nash, 2007). The more complete metric is the noise equivalent power (NEP), which is the lowest detectable P_{opt} in the device, i.e. the P_{opt} which becomes equal to the noise power in the

96

device. Thus, in the presence of large dark current, high $R(\lambda)$ devices may have large NEP, defeating the purpose of the high gain. Dark current must be minimized while maximizing $R(\lambda)$ simultaneously. In addition, these high gain, low NEP devices must also give fast response times, which presents a fundamental tradeoff in engineering the gain and bandwidth (B) of these detectors.

Photodetectors based on wide bandgap semiconductors (bandgap $E_g>3.2eV$ i.e**.** $\lambda_{cutoff}<1241/E_g=387nm$) such as SiC(E Monroy, Omnes, et al., 2003) and GaN(E Monroy, Omnes, et al., 2003) can provide intrinsic visible-blindness, but require filters to achieve true solar blindness. In chapter 4, SiC photodetectors (Chava et al., 2017) were demonstrated with $R>10A/W$, and NEP as low as 2.3fW at 20Hz. Further, these devices have response times in the milli-second (ms) range. While this is fast enough for imaging applications at 24Hz, these devices are still slower than the micro-second (μs) response times offered by photodiodes, or PMT's.

Therefore, it is important to design and fabricate semiconductor UV detectors that are suitable for solar-blind UV detection. As explained, the absorption cut-off is determined by the bandgap of absorbing semiconductor material. Only ultra-wide bandgap(UWBG) semiconductors ($E_g>4.3eV$, $\lambda_{cutoff}<290nm$) such as $Al_xGa_{1-x}N$ (x>0.5) or Ga_2O_3 provide intrinsic solar blindness. Among these two material systems, $Al_xGa_{1-x}N$ based UV detectors have been successfully demonstrated by several groups for solar-blind UV detection. As discussed in chapter 1 (Figure 1.11), by increasing the Al mole fraction (from x=0 to 1) in $Al_xGa_{1-x}N$ UV detectors, the absorption cut-off wavelength can be shifted from 365nm(x=0) to 200nm(x=1) in the UV spectrum. Further, due to their direct

97

bandgap they offer spectral selectivity (have sharp cut-off wavelength) compared to other WBG such as SiC which is an indirect bandgap semiconductor.

Recently, $Al_xGa_{1-x}N$ field effect transistor (FET) detectors with $R(\lambda) > 10^5$ A/W (Yoshikawa et al., 2016) (S. Muhtadi et al., 2017) have been demonstrated with solar rejection ratios $> 10^3$, while fast response $< 1\mu s$ has been demonstrated in $Al_xGa_{1-x}N$ photodiodes[2], with NEP as low as 6nW at bandwidth (B)=100kHz (Osinsky, Gangopadhyay, Lim, et al., 1998). The $Al_xGa_{1-x}N$ Metal-Semiconductor-Metal (MSM) detectors with Al fraction x>0.5 have shown high photosensitivity of 10^6 A/W and a rejection ratio of 10^6 (Yoshikawa et al., 2017). Also, recently few research groups have shown high temperature operation of $Al_xGa_{1-x}N$ channel HEMT devices that are suitable for high power and RF applications. These UWBG transistors also provide high temperature operation up to 300°C demonstrated with little loss of current handling (Sakib Muhtadi, Hwang, Coleman, Asif, et al., 2017), (Neudeck et al., 2002), ideal for harsh environment applications where short wavelength ((as low as λ=200nm) or deep UV (DUV) detection is needed. These promising results open up the potential for high Al content $Al_xGa_{1-x}N$ (x>0.5) based photodetectors, where high $R(\lambda)$ and low NEP might be achievable simultaneously. The challenges for $Al_xGa_{1-x}N$ x>0.5 technology for solar-blind detection are in materials growth and contact formation (Sakib Muhtadi, Hwang, Coleman, Asif, et al., 2017), (Baca et al., 2016), (Bajaj, Akyol, Krishnamoorthy, Zhang, & Rajan, 2016), which are currently being investigated (Yoshikawa et al., 2017).

As discussed in chapter 1, the Al mole fraction is key to controlling the absorption spectrum (or spectral response) of $Al_xGa_{1-x}N$ based UV detectors. In this present study, the potential for $Al_xGa_{1-x}N$ high electron mobility transistors (HEMT's) is discussed as high-

performance UV photodetectors. In these HEMT devices, a highly conductive 2 dimensional electron gas(2DEG) induced at the interface between $Al_{0.85}Ga_{0.15}N$ / $Al_{0.65}Ga_{0.35}N$ interface acts as channel. Using an x=0.65 for channel and x=0.85 for barrier, a polarization doped 2DEG is formed at the interface (Figure 5.1) due to the difference in c/a ratio of the two alloys, similar to AlGaN/GaN HEMT's (Mishra, Parikh, & Wu, 2002).

Figure 5.1 Schematic of HEMT device structure with $Al_{0.85}Ga_{0.15}N$ barrier layer and $Al_{0.65}Ga_{0.35}N$ channel layer.

This 2DEG offers a high electron mobility $\sim\mu_n\sim300cm^2/Vs$ (Sakib Muhtadi, Hwang, Coleman, Asif, et al., 2017), as explained later. The mobility of 2DEG in $Al_{0.65}Ga_{0.35}N$ FET channel, on the other hand, is $\sim100cm^2/Vs$ (S. Muhtadi et al., 2017). This implies three times(3x) higher drain current in the $Al_{0.85}Ga_{0.15}N/Al_{0.65}Ga_{0.35}N$ HEMT devices, and therefore potentially three times(3x) higher responsivity ($R(\lambda)$) in these new HEMT device structures. Moreover, this HEMT structure has a very thin($\sim$20-30nm) $Al_{0.85}Ga_{0.15}N$ barrier layer. Since the band gap of this barrier layer is very high ((E_g=5.8eV, λ_{cutoff}=213nm), it acts as a transparent barrier layer and allows the incident DUV light to

penetrate into the $Al_{0.65}Ga_{0.35}N$ channel layer, and the direct bandgap of $Al_{0.65}Ga_{0.35}N$ ensures complete absorption of DUV light entering channel layer through barrier layer.

5.2 EXPERIMENTAL DETAILS

The device epilayer structures used in this study were grown with a 3µm thick AlN buffer layer over basal plane sapphire substrates using a growth procedure reported earlier(Fareed et al., 2007). The (102) off-axis X-ray peak linewidth for the AlN buffers was measured to be 330 arc-secs. This corresponds to an overall dislocation density $\sim 1x10^8$ cm^{-2} (Fareed et al., 2007) based on our previous calibrations. The undoped channel $Al_{0.65}Ga_{0.35}N$ layer for our structures was 0.5 µm thick. Reciprocal space lattice Mapping (RSLM) shows it to grow pseudomorphic over the AlN buffer. In contrast, the GaN channel layers are relaxed with a thickness of $\sim 1-2\mu m$, in case of AlGaN/GaN HEMT structures(Asif et al., 2014). This qualitative difference will become important in understanding the response time of the HEMT photodetector below (Iwaya et al., 2009).

The 30nm thick $Al_{0.85}Ga_{0.15}N$ barrier layers were then grown to form the polarization doped heterostructure as shown in HEMT structure in Figure 5.1, with the band diagram (Grundmann, n.d.) shown in Figure 5.2. These layers were also grown pseudomorphically as confirmed by XRD. The sheet resistivity of the 2DEG channel was 1900 $\Omega/\square$ as measured by an eddy current non-contact technique. The dark threshold voltage, V_T as measured by Hg-probe C-V system was -8V (Sakib Muhtadi, Hwang, Coleman, Asif, et al., 2017). This threshold voltage is in agreement with V_T measured from I-V, as seen below in Figure 5.4(b). The effective 2DEG channel mobility for these devices was measured to be $\sim 300cm^2/Vs$ (Sakib Muhtadi, Hwang, Coleman, Asif, et al., 2017), showing that the threading dislocations do not degrade the mobility due to efficient

100

screening by the high electron concentration in the channel.

The $Al_{0.65}Ga_{0.35}N$ channel HEMT devices were then fabricated using standard photo-lithography, mesa-etching and liftoff processing. After the mesa reactive-ion etching to isolate the $Al_{0.85}Ga_{0.15}N$ barriers and the induced conducting channel at its interface with the $Al_{0.65}Ga_{0.35}N$ layer Zr/Al/Mo/Au (10/100/40/30nm) ohmic-contacts and Ni/Au (100/100nm) gates were metalized. The ohmic-contacts were annealed at $950^{o}C$ for 30 sec. The gate-length L_G for all the devices was 1.8 µm. Figure 5.1 shows the device structure, and Figure 5.2 shows corresponding band diagram (Grundmann, n.d.).

Figure 5.2 Band diagram of the $Al_{0.85}Ga_{0.15}N/Al_{0.65}Ga_{0.35}N$ HEMT device under illumination. The distance is measured from the top of the device. As shown, optically generated electrons will be accumulated near the barrier/channel interface forming 2DEG and the holes floating away from this interface.

Figure 5.3(b) shows the cathodoluminescence (CL) spectrum of the fully fabricated device taken in a scanning electron microscope (SEM) with a built-in parabolic mirror. The spectrum shows clear band-edge emission at ~250nm, with a near band-edge signal at ~265nm, corresponding to the $Al_{0.65}Ga_{0.35}N$ channel. The micrograph shown in Fig. 5.3(a)

is taken with the CL spectrometer set to the peak emission at 250nm (10nm slit width), and scanned across the device, with the CL signal measured with an auxiliary input in the SEM. The $Al_{0.85}Ga_{0.15}N$ barrier mesa edges are clearly visible, even through the metal contacts giving an electrically active light absorbing area of $260x100\mu m^2$.

Figure 5.3 (a) CL image of the HEMT device under 250nm illumination. As shown, these are 2 finger devices consisting 2 source pads. The barrier mesa edges are highlighted as red dotted lines. (b) CL spectrum of the same device.

The photodetector characteristic results discussed here after are based on measurements of a 2-finger HEMT device (Figure 5.3(a)), fabricated as discussed above, with 100μm width and a source-drain distance of 8μm. The I-V measurements in the dark and under illumination were performed using an HP4155C parameter analyzer with a probe station. Similarly, capacitance-voltage (C-V) measurements were performed on large area Schottky-gate test structures fabricated on the same chip, with area $2\times10^{-4}cm^2$ at 1kHz. The photoresponse measurements were performed using a monochromator with a Xe-arc lamp source, and the illumination wavelength is varied from 500 nm down to 220nm. The light was illuminated from the top of the device at a 45° angle, with a spot size of $\sim1cm^2$. The optical power P_{opt} of light incident on the device is measured using a Thorlabs UV-

102

enhanced Si photodiode. The photocurrent was then measured and normalized to the beam power. The extracted relative responsivity was calibrated to a broad area hand-held 254nm Hg-vapor lamp with a uniform illumination density at $6.5 \mu W/cm^2$, comparable to the power in the monochromator beam at 254nm to obtain an absolute $R(\lambda)$ by using Equation 5.1.

The noise and ON/OFF transient measurements were performed with a Keithley 2610 2-channel source-meter unit (SMU). The two channels (channel-A and channel-B) in the SMU were used to apply gate voltage(V_G) and drain voltage(V_D) to the device. On the other hand, the device source is routed into a current trans-impedance pre-amplifier whose input functions as a virtual ground to measure the drain current I_D, which was also monitored using the source-meter. The output voltage from the pre-amplifier was fed into an oscilloscope where the time dependence of current under 250nm illumination was measured. In the dark, the drain current was allowed to stabilize for 5 minutes before taking data. For noise measurements, the time trace of the dark current was converted to a frequency dependence using the FFT function on the oscilloscope, enabling measurement of the dark noise spectrum between 1-100Hz.

5.3 RESULTS AND DISCUSSION

Figure 5.4(a) shows the measured output characteristics or family of curves(I_D-V_{SD}) under dark and 254nm illumination. A 254nm UV LED lamp is used for measuring these output characteristics, and the illumination power used for these measurements is fixed at 6.5 $\mu W/cm^2$ as measured as by using a calibrated Si photodiode. Similarly, the transfer characteristics (I_D-V_{GS}) of the device are measured both in dark and under 6.5 $\mu W/cm^2$ 254nm illumination. Figure 5.4(b) shows the transfer characteristics, i.e. drain current (I_{DS})

103

characteristics measured as a function of gate voltage(V_{GS}), in saturation region of the device for V_{DS}=+15V.

As clearly shown in these figures, the UV illumination on to the device causes an increase in the overall drain current level. This increase in drain current (I_D) is understood by considering the incident photon energy (4.9eV) of 254nm UV lamp. Since the incident 254nm photons have energy greater than the bandgap of the $Al_{0.65}Ga_{0.35}N$ channel layer which is ~4.8eV, these DUV photons will be absorbed in the channel layer and thus creating e-h pairs as shown in Figure 5.2. The holes diffuse away from the interface, while

Figure 5.4 (a) Output characteristics(I_{DS}-V_{DS}) of the HEMT photodetector in the dark (black curves) and under 254nm illumination (red curves). While the saturation current I_D is higher under illumination than in the dark, it is lower under illumination in the triode region due to lower mobility arising from poorer carrier confinement under illumination. (b) Transfer characteristics(I_D-V_{GS}) of device overlaid with C-V characteristic of large area test structure on the same chip in the dark and under the same 254nm illumination.

electrons fall into the quantum well, leading to an increase in the electron sheet concentration, n_s, in the well. The high electron sheet concentration in this quantum well also called as 2DEG results in higher drain current I_D in the current of the HEMT device.

This increase in n_s is accompanied by a reduction in confinement in the quantum well for the 2DEG. This is also manifested in the output curves, as shown in Figure 5.4(a), where the triode region shows weaker slope under illumination indicating lower channel mobility, and I_D eventually saturates at a higher current under illumination.

The gate-source C-V performed on large area Schottky gate test structures, also shows an increase in overall carrier concentration in the channel under 254nm illumination, manifested as a ~0.1V shift. As shown in Figure 5.4(b), the sheet carrier $n_s \approx 1.2 \times 10^{13} cm^{-2}$. This sheet carrier concentration, n_s is estimated by calculating the area of C-V curve in dark.

Figure 5.5 Responsivity action spectrum as a function of gate voltage. Vertical dotted line in black at 280nm shows the absorption edge of $Al_{0.65}Ga_{0.35}N$ channel of the HEMT device used in this study.

The spectral responsivity (or action spectrum) for the photodetector is shown from 220-520nm in Figure 5.5, for 3 different V_{GS}. A peak R(230nm) $=2.8\times10^6$A/W is seen in the on-state, decreasing to ~10^3A/W near threshold where NEP is the lowest (as will be discussed later in this section). Solar rejection ratio ~10^3 is seen across the V_{GS} range,

105

although a strong visible response is observed. Here, the solar rejection ratio for the HEMT device is defined as the ratio of peak responsivity corresponding to illumination wavelengths below 290 nm to the responsivity corresponding to 300 nm (i.e. wavelengths above 290nm). Since the AlN templates were grown at a different time than the HEMT devices, it is expected that trapping effects should decrease significantly if the entire structure is grown in-situ.

These HEMT photodetectors show excellent saturation, which indicates high output resistance, r_o, ideal for implementing these phototransistors in circuits. Large r_o leads to high small-signal voltage gain for detecting small light intensities. Moreover, large r_o also minimizes the thermal noise in photodetectors, where the spectral noise density as a function of frequency, $S_{n,\,thermal}(f)$ in A^2/Hz is:

$$S_{n,thermal}(f) = 4kT/r_o \qquad \text{(Eq.5.2)}$$

, which near threshold at V_{GS}=-8V is ~$3\times10^{-28}A^2$/Hz. This leads to a dark noise current $\sqrt{S_{n,thermal}(f)B}$ ~20fA at a bandwidth B=1Hz. The dark current just below threshold is ~0.3nA, giving a dark noise density:

$$S_{n,dark} = 2qI_D(V_{GS}, V_{DS} = 10V) \qquad \text{(Eq.5.3)}$$

,which near threshold gives a noise current of 10fA.

In Figure 5.5(f), using the measured dark currents in Fig. 5.3(a), the white noise components are estimated as a function of gate voltage using the Equations 5.2 and 5.3, assuming a bandwidth of 1Hz, using:

$$i_{noise,white}(V_{GS}, V_{DS} = 10V) = \sqrt{S_{n,thermal}B + S_{n,dark}B} \qquad \text{(Eq.5.4)}$$

106

The white noise component estimated here is compared with the measured noise power (Fig. 5.6(f)), $S_{n,1/f}(1)$, which is seen to be completely dominated by 1/f flicker noise. The lowest noise in saturation is displayed at V_{DS}=10V, for our measurements.

Figure 5.6 Noise spectrum in the dark of the HEMT as a function of gate voltage V_{GS} showing clear flicker $1/f^2$ noise. (a) V_{GS}=-8V, I_d(dark)=0.3nA, (b) V_{GS}=-7.9V, I_d(dark)=5.8nA, (c) V_{GS}=-7.5V, I_d(dark)=4.3μA, (d) V_{GS}=-7.0V, I_d(dark)=47.8μA (e) V_{GS}=-5V, I_d(dark)=746μA. (f) Comparison of measured $1/f^2$ noise current and predicted white noise from dark current characteristics as a function of V_{GS}. Y-axis shows V_{GS} dependence of the responsivity at λ=220nm, with the NEP values shown next to each data point. The inset shows the on and off photoresponse transients, with ~20s times in both directions.

The measured flicker noise spectral density for these HEMT's is $\sim 10^5$ higher, in comparison with EG/SiC photodetectors discussed in chapter 4, for similar dark currents and device areas. This large flicker noise has a $1/f^2$ dependence, sometimes called a Lorentzian dependence to distinguish it from normal 1/f noise, and is attributed to slow trapping effects often seen in III-N devices (Yan Kuin Su et al., 2003). From here, $S_{n,1/f}^2(1)$ will be used to refer to the measured $1/f^2$ noise at 1Hz, leading to $i_{noise,1/f^2} = \sqrt{S_{n,1/f^2}(1)}$ assuming B=1Hz.

107

Using the measured photocurrent i.e. $I_D(\lambda)$-$I_D(dark)$ from output curve measurements (Figure 5.2(a)), $R(\lambda)$ was extracted as a function of V_{GS} (shown in Figure 5.5), and is <u>seen to increase with dark current</u> as expected. The V_{GS} dependence of $R(\lambda)$ is shown for λ=220nm in Fig. 5.6(f). The R(220nm) decreases near the threshold voltage, although this is also accompanied by a sharp decrease in $i_{noise,1/f}^2$, leading to an overall improvement in NEP, defined as:

$$NEP = i_{noise,1/f^2}/R(\lambda) \qquad (Eq.5.5)$$

, shown in Fig. 5.6(f) next to each $R(\lambda, V_{GS})$ data point. Even at V_{GS}=-7V, where the HEMT is in the on-state, the NEP is in the pW range, surpassing Si photodiodes (Hamamatsu, 2009) in the DUV, dropping to the fW range at threshold (Table 5.1).

The specific detectivity(D^*) for these detectors is also estimated, as described in chapter 4, by using the equation:

$$D^* = \sqrt{AB}/NEP \qquad (Eq.5.7)$$

, where A=2.5×10^{-4}cm^2 is the absorbing mesa area (Fig. 5.2(a)) and B is the bandwidth.

This UWBG Al$_{0.65}$Ga$_{0.35}$N channel HEMT shows superior performance in most metrics, with among the lowest NEP for a solar-blind detector at these DUV wavelengths.

Table 5.1 Comparison of $Al_{0.85}Ga_{0.15}N/Al_{0.65}Ga_{0.35}N$ HEMT UV detector performance metrics with previous works.

Device		R (A/W)	Solar rejection (R_{Peak}:R_{300nm})	Response time	Dark Current (nA)	NEP (W) At 220nm	Specific Detectivity, D* (Jones)
This work	-8V	7.8×10^2	$\sim10^2$	20s	0.3	4.7 fW	3.3×10^{12} (BW=1Hz)
	+4V	1×10^6	$\sim5\times10^2$	N/A	6.5×10^6	N/A	N/A
AlGaN/GaN HFET[1]		10^5	>1	1.9ms (ON) 2.5ms (OFF)	1	N/A	N/A
AlGaN/AlGaN HFET[2]		3×10^3	$>10^4$	N/A	0.05	N/A	N/A
AlGaN/AlGaN MSM PD[3]		$>10^6$	$>10^6$	0.2s (ON) 1000s (OFF)	0.01	N/A	N/A
SiC APD[4]		93 (At 280nm)	N/A	N/A	0.005	20 fW (At 280nm)	6.4×10^{13} (BW=1KHz)
EG/SiC BJT[5]		17 (At 270nm)	<1	10ms (ON) 46ms (OFF)	0.2	~2.3fW (At 270nm)	4.4×10^{13} (BW=20Hz)

[1] (Iwaya et al., 2009), [2] (Yoshikawa et al., 2016), [3] (Yoshikawa et al., 2017), [4] (Bai et al., 2007), [5] (Chava et al., 2017)

In Table 5.1, the photodetector results of the present HEMT transistor are compared with other key related results in DUV detection

As shown in Figure. 5.4(b), the C-V characteristic curves measured at 1kHz under $6.5\mu W/cm^2$ illumination at 254nm shifts more negative by 0.1V near threshold at V_{GS}=-8V. In the dark, increasing V_{GS} by 0.1V increases I_{DS} from 0.3nA to 5.8nA (Figure 5.4(a)), implying a sub-threshold swing of ~80mV/decade, increasing to ~120mV/decade at V_{GS}=-7.5V, in excellent agreement with the 98mV/decade measured for other devices on the same chip (Sakib Muhtadi, Hwang, Coleman, Asif, et al., 2017). Thus, a pure photovoltaic response should result in a photocurrent of 5.5nA. However, the observed increase in I_D under illumination is significantly larger ~2μA (Figure 5.6(f) inset), indicating that persistent photoconductivity due to trapping is responsible for high I_D.

To understand the origin of these traps, the sub-threshold slope(SS) in this transistor is calculated to estimate the density of interface traps (Baca et al., 2016)·(Sze & Ng, 2006):

$$SS(\frac{mV}{dec}) = \frac{2.303kT}{q} \left[1 + \frac{qD_{it}}{C_G(V_T)}\right] \qquad (Eq.5.6)$$

, where D_{it} is the density of interface traps, C_{GS} is the measured gate capacitance. From the measured SS=80mV/dec near threshold above, (Figure. 5.4(b)), which is comparable to the 75mV/dec SS measured by Baca et.al (Baca et al., 2016), $D_{it}<3\times10^{10}cm^{-2}$ is estimated using $C_{GS}(-8V)<0.01\mu F/cm^2$ (Figure 5.3(b)) just below threshold to ensure that the capacitance and conductivity is entirely due to the barrier/channel interface, and not the substrate/channel interface. This suggests that the top $Al_{0.85}Ga_{0.15}N/Al_{0.65}Ga_{0.35}N$ barrier/channel interface is unlikely to be responsible for the persistent photoconductivity. We also exclude absorption of 254nm by the barrier layer, because the bandgap for

110

$Al_{0.85}Ga_{0.15}N$ is ~5.7eV greater than the energy of 254nm photons (4.9eV). Thus, persistent photoconductivity from surface barrier modulation as seen in AlGaN/GaN (Koley et al., 2002) cannot be responsible for $\lambda > 210$nm, the band-edge for the barrier.

This leaves the $Al_{0.65}Ga_{.35}N$/AlN channel/template interface. The AlN templates were grown at a different time from the HEMT structure, which could lead to trap states at this interface. Moreover, the carrier dynamics under UV-illumination suggest that holes could get trapped at this interface, as the electric field in the $Al_{0.65}Ga_{0.35}N$ channel drives holes from e-h pair creation to the back interface, as illustrated in Figure 5.2.

The ON/OFF response time characteristics at 250nm (Figure 5.6(f) inset) show slow transients ~20s, providing strong experimental evidence of this trapping effect (Koley et al., 2002). The observation of the $1/f^2$ noise (Figure 5.6(a-e)) correlates with this slow response time, as $S_n \sim [1+(f/f_0)^2]^{-1} \sim 1/f^2$ for $f > f_0$, where f_0 is the characteristic frequency associated with the trapping(Yan Kuin Su et al., 2003). Thus, reducing trapping effects through growth optimization of the AlN template/$Al_{0.65}Ga_{0.35}N$ channel interface will reduce $1/f^2$ noise, while simultaneously increasing speed. One solution to electrically isolate the 2DEG channel from these traps is to use a polarization-doped graded back barrier, graded from AlN down to the $Al_{0.65}Ga_{0.35}N$ channel region.

Note that the access regions between source-gate and gate-drain are also modulated by the incident light. Since the access regions are always in the 'on' state, they can also display persistent photoconductivity (Sze & Ng, 2006) as in photoconductors. In the present measurements, the time-constant for the on/off response times decreased somewhat from the >20s measured above near threshold to ~10s, still displaying a slow time-constant.

111

In other words, the response time was relatively insensitive to V_{GS}. However, the access regions are tentatively eliminated as responsible for the slow response, as Iwaya et. al (Iwaya et al., 2009) report fast response times in the 1-3 ms regime for similar geometry visible-blind $Al_{0.21}Ga_{0.79}N/GaN$ HEMT's with a p-GaN gate. However, their GaN channel layers are ~2μm thick on AlN templates on sapphire, and are metamorphic. Thus, the absorbing region ~0.4μm[22] is far from the AlN/GaN growth interface, minimizing the impact of trapping from this interface. This suggests the use of a thick channel epilayer as another potential solution to increase the speed of the device. The effect of device architecture on the response time and noise bears further investigation, as GaAs MESFET photodetectors have shown sub-ns response times (Flesner, Davis, & Wieder, 1982).

5.4 SUMMARY

In summary, a DUV detector based on $Al_{0.85}Ga_{0.15}N/Al_{0.65}Ga_{0.35}N$ HEMT device structure is demonstrated. This device showed a NEP=4.7fW when operated near threshold which is V_{GS}=-8V. A peak responsivity(R) as high as $3x10^6$A/W is achieved at 230nm for V_{GS}=+4V, in saturation mode at V_{DS}=+10V. A solar-rejection ratio of ~10^2 is observed at 220nm:300nm. The small sub-bandgap response is attributed to point defects in the epilayers, likely from the $AlN/Al_{0.65}Ga_{0.35}N$ (template/channel) growth interface. The photodetector is slow, with >20s response times for both on and off transients, again attributed to trapping at the AlN template/$Al_{0.65}Ga_{0.35}N$ growth interface, which may be improved by growth optimization. The elimination of the trapping should also reduce the $1/f^2$ noise, and consequently improving the NEP also.

REFERENCES

Anderson, T. J., Hobart, K. D., Greenlee, J. D., Shahin, D. I., Koehler, A. D., Tadjer, M. J., … Kub, F. J. (2015). Ultraviolet detector based on graphene/SiC heterojunction. *Applied Physics Express*, *8*(4), 41301. https://doi.org/10.7567/APEX.8.041301

Asif, F., Lachab, M., Coleman, A., Ahmad, I., Zhang, B., Adivarahan, V., & Khan, A. (2014). Deep ultraviolet photopumped stimulated emission from partially relaxed AlGaN multiple quantum well heterostructures grown on sapphire substrates. *Journal of Vacuum Science & Technology B, Nanotechnology and Microelectronics: Materials, Processing, Measurement, and Phenomena*, *32*(6), 61204. https://doi.org/10.1116/1.4898694

Ayalew, T. (2004). *SiC semiconductor devices technology, modeling and simulation*.

Baca, A. G., Armstrong, A. M., Allerman, A. A., Douglas, E. A., Sanchez, C. A., King, M. P., … Kaplar, R. J. (2016). An AlN/Al0.85Ga0.15N high electron mobility transistor. *Applied Physics Letters*, *109*(3), 33509. https://doi.org/10.1063/1.4959179

Bai, X., Guo, X., McIntosh, D. C., Liu, H. D., & Campbell, J. C. (2007). High detection sensitivity of ultraviolet 4H-SiC avalanche photodiodes. *IEEE Journal of Quantum Electronics*, *43*(12), 1159–1162. https://doi.org/10.1109/JQE.2007.905031

Bajaj, S., Akyol, F., Krishnamoorthy, S., Zhang, Y., & Rajan, S. (2016). AlGaN channel field effect transistors with graded heterostructure ohmic contacts. *Applied Physics Letters*, *109*(13), 133508. https://doi.org/10.1063/1.4963860

Balachandran, A. (2017). *High Quality Low Offcut 4H-SiC Epitaxy and Integrated Growth of Epitaxial Graphene for Hybrid Graphene/SiC Devices*. University of South Carolina.

Balandin, A. A., Ghosh, S., Bao, W., Calizo, I., Teweldebrhan, D., Miao, F., & Lau, C. N. (2008). Superior Thermal Conductivity of Single-Layer Graphene. *Nano*, *8*(3), 902–907.

Baliga, B. J. (2008). *Fundamentals of Power Semiconductor Devices*. Springer. https://doi.org/10.1007/978-0-387-47314-7

Barker, B. G., Chava, V. S. N., Daniels, K. M., Chandrashekhar, M. V. S., & Greytak, A. B. (2017). Sub-bandgap response of graphene/SiC Schottky emitter bipolar phototransistor examined by scanning photocurrent microscopy. *2D Materials*, *5*(1), 11003.

Blake, P., Brimicombe, P. D., Nair, R. R., Booth, T. J., Jiang, D., Schedin, F., … Novoselov, K. S. (2008). Graphene Based Liquid Crystal Device. *Nano Letters*, *8*,

1704.   Retrieved   from http://pubs.acs.org/doi/abs/10.1021/nl080649i%0Ahttp://pubs.acs.org/doi/pdfplus/10.1021/nl080649i

Bolotin, K. I., Sikes, K. J., Jiang, Z., Klima, M., Fudenberg, G., Hone, J., … Stormer, H. L. (2008). Ultrahigh electron mobility in suspended graphene. *Solid State Communications*, *146*(9–10), 351–355. https://doi.org/10.1016/j.ssc.2008.02.024

Bonaccorso, F., Sun, Z., Hasan, T., & Ferrari, A. C. (2010). Graphene photonics and optoelectronics. *Nature Photonics*, *4*(9), 611–622. https://doi.org/10.1038/nphoton.2010.186

Campbell, J. C. (2007). Recent advances in avalanche photodiodes. *JOURNAL OF LIGHTWAVE TECHNOLOGY*, *25*(1), 109–121. https://doi.org/10.1109/LEOS.2008.4688747

Campbell, J. C., Dentai, A. G., Qua, G. J., & Ferguson, J. F. (1983). Avalanche InP/InGaAs heterojunction phototransistor. *IEEE Journal of Quantum Electronics*, *19*(6), 1134–1138.

Cançado, L. G., Jorio, A., Ferreira, E. H. M., Stavale, F., Achete, C. A., Capaz, R. B., … Ferrari, A. C. (2011). Quantifying defects in graphene via Raman spectroscopy at different excitation energies. *Nano Letters*, *11*(8), 3190–3196. https://doi.org/10.1021/nl201432g

Chava, V. S. N., Barker, B. G., Balachandran, A., Khan, A., Simin, G., Greytak, A. B., & Chandrashekhar, M. V. S. (2017). High detectivity visible-blind SiF4grown epitaxial graphene/SiC Schottky contact bipolar phototransistor. *Applied Physics Letters*, *111*(24), 243504. https://doi.org/10.1063/1.5009003

Chava, V. S. N., Chandrashekhar, M. V. S., Daniels, K. M., Barker, B. G., & Greytak, A. B. (2016). Epitaxial graphene (EG)/SiC based Schottky emitter bipolar phototransistors for UV detection and effect of hydrogen intercalation on device I-V characteristics. In *Proceedings of IEEE Sensors* (pp. 1–3). https://doi.org/10.1109/ICSENS.2016.7808587

Chava, V. S. N., Omar, S. U., Brown, G., Shetu, S. S., Andrews, J., Sudarshan, T. S., & Chandrashekhar, M. V. S. (2016). Evidence of minority carrier injection efficiency >90% in an epitaxial graphene/SiC Schottky emitter bipolar junction phototransistor for ultraviolet detection. *Applied Physics Letters*, *108*(4). https://doi.org/10.1063/1.4940385

Chen, H., Liu, K., Hu, L., Al-Ghamdi, A. A., & Fang, X. (2015). New concept ultraviolet photodetectors. *Materials Today*, *18*(9), 493–502. https://doi.org/10.1016/j.mattod.2015.06.001

Chen, Q., Yang, J. W., Osinsky, A., Gangopadhyay, S., Lim, B., Anwar, M. Z., … Temkin, H. (1997). Schottky barrier detectors on GaN for visible–blind ultraviolet detection. *Applied Physics Letters*, *70*(17), 2277–2279. https://doi.org/10.1063/1.118837

Chen, X., Zhu, H., Cai, J., & Wu, Z. (2007). High-performance 4H-SiC-based ultraviolet

114

p-i-n photodetector. *Journal of Applied Physics*, *102*(2), 24505. https://doi.org/10.1063/1.2747213

Chow, T. P., Khemka, V., Fedison, J., Ramungul, N., Matocha, K., Tang, Y., & Gutmann, R. J. (2000). SiC and GaN bipolar power devices. *Solid-State Electronics*, *44*(2), 277–301. https://doi.org/10.1016/S0038-1101(99)00235-X

Colace, L., Ferrara, P., Assanto, G., Fulgoni, D., & Nash, L. (2007). Low dark-current germanium-on-silicon near-infrared detectors. *IEEE Photonics Technology Letters*, *19*(22), 1813–1815. https://doi.org/10.1109/LPT.2007.907578

Coletti, C., Forti, S., Principi, A., Emtsev, K. V., Zakharov, A. A., Daniels, K. M., … Starke, U. (2013). Revealing the electronic band structure of trilayer graphene on SiC: An angle-resolved photoemission study. *Physical Review B*, *88*(15), 155439. https://doi.org/10.1103/PhysRevB.88.155439

Coletti, C., Riedl, C., Lee, D. S., Krauss, B., Patthey, L., Von Klitzing, K., … Starke, U. (2010). Charge neutrality and band-gap tuning of epitaxial graphene on SiC by molecular doping. *Physical Review B*, *81*(23), 235401. https://doi.org/10.1103/PhysRevB.81.235401

Coraux, J., N'Diaye, A. T., Busse, C., & Michely, T. (2008). Structural coherency of graphene on Ir(111). *Nano Letters*, *8*(2), 565–570. https://doi.org/10.1021/nl0728874

Daas, B. K. (2012). *PLASMONICS USING HIGH QUALITY EPITAXIAL GRAPHENE: AN APPROACH TOWARDS NEXT-GENERATION OPTICAL COMPUTING*.

Daas, B. K., Daniels, K. M., Sudarshan, T. S., & Chandrashekhar, M. V. S. (2011). Polariton enhanced infrared reflection of epitaxial graphene. *Journal of Applied Physics*, *110*(11), 1–7. https://doi.org/10.1063/1.3666069

Daas, B. K., Nomani, W. K., Daniels, K. M., Sudarshan, T. S., Koley, G., & Chandrashekhar, M. V. S. (2012). Molecular Gas Adsorption Induced Carrier Transport Studies of Epitaxial Graphene Using IR Reflection Spectroscopy. *Materials Science Forum*, *717–720*, 665–668. https://doi.org/10.4028/www.scientific.net/MSF.717-720.665

Daas, B. K., Omar, S. U., Shetu, S., Daniels, K. M., Ma, S., Sudarshan, T. S., & Chandrashekhar, M. V. S. (2012). Comparison of epitaxial graphene growth on polar and nonpolar 6H-SiC faces: On the growth of multilayer films. *Crystal Growth and Design*, *12*(7), 3379–3387. https://doi.org/10.1021/cg300456v

Dawlaty, J. M., Shivaraman, S., Strait, J., George, P., Chandrashekhar, M., Rana, F., … Chen, Y. (2008). Measurement of the optical absorption spectra of epitaxial graphene from terahertz to visible. *Applied Physics Letters*, *93*(13), 131905. https://doi.org/10.1063/1.2990753

Dresselhaus, M. S., & Dresselhaus, G. (2002). Intercalation compounds of graphite. *Advances in Physics*, *51*(1), 1–186. https://doi.org/10.1080/00018730110113644

Ellison, A. (1999). *Silicon Carbide Growth by High Temperature CVD Techniques*. https://doi.org/10.1007/978-94-009-2101-6

115

Emtsev, K. V., Speck, F., Seyller, T., Ley, L., & Riley, J. D. (2008). Interaction, growth, and ordering of epitaxial graphene on SiC{0001} surfaces: A comparative photoelectron spectroscopy study. *Physical Review B - Condensed Matter and Materials Physics*, *77*(15), 155303. https://doi.org/10.1103/PhysRevB.77.155303

Fareed, Q., Adivarahan, V., Gaevski, M., Katona, T., Mei, J., Ponce, F. a., & Khan, A. (2007). Metal–Organic Hydride Vapor Phase Epitaxy of Al x Ga 1- x N Films over Sapphire. *Japanese Journal of Applied Physics*, *46*(No. 31), L752–L754. https://doi.org/10.1143/JJAP.46.L752

Flesner, L. D., Davis, N. M., & Wieder, H. H. (1982). High speed response of a GaAs metal-semiconductor field-effect transistor to electron-beam excitation. *Journal of Applied Physics*, *53*(5), 3873–3877. https://doi.org/10.1063/1.331087

Freitag, M. (2008). Graphene: Nanoelectronics goes flat out. *Nature Nanotechnology*, *3*(8), 455–457. https://doi.org/10.1038/nnano.2008.219

Garlow, J. A., Barrett, L. K., Wu, L., Kisslinger, K., Zhu, Y., & Pulecio, J. F. (2016). Large-Area Growth of Turbostratic Graphene on Ni(111) via Physical Vapor Deposition. *Scientific Reports*, *6*, 19804. https://doi.org/10.1038/srep19804

Grundmann, M. J. (n.d.). Bandeng_Mike Grudmann_UCSB.pdf. Retrieved from http://my.ece.ucsb.edu/mgrundmann/bandeng.htm

Gundimeda, A., Krishna, S., Aggarwal, N., Sharma, A., Sharma, N. D., Maurya, K. K., … Gupta, G. (2017). Fabrication of non-polar GaN based highly responsive and fast UV Photodetector, *103507*, 1–5. https://doi.org/10.1063/1.4978427

Haizheng Song, Tawhid Rana, M.V.S. Chandrashekhar, Sabih U. Omar, T. S. S. (2013). Comparison of SiC Epitaxial Growth from Dichlorosilane and Tetrafluorosilane precursors. *ECS Transactions*, *58*(4), 97–109.

Hamamatsu. (2009). *Opto-semiconductor handbook*. Hamamatsu Photonics K.K.Solid State Division. Retrieved from http://www.hamamatsu.com/resources/pdf/ssd/e02_handbook_si_photodiode.pdf

Hooge, F. N. (1994). 1/f Noise Sources. *IEEE Transactions on Electron Devices*, *41*(11), 1926–1935. https://doi.org/10.1109/16.333808

Hudgins, J. L., Member, S., Simin, G. S., Santi, E., & Khan, M. A. (2003). An Assessment of Wide Bandgap Semiconductors for Power Devices. *IEEE Transaction on Power Electronics*, *18*(3), 907–914.

Iwaya, M., Miura, S., Fujii, T., Kamiyama, S., Amano, H., & Akasaki, I. (2009). High-performance UV detector based on AlGaN/GaN junction heterostructure-field-effect transistor with a p-GaN gate. *Physica Status Solidi (C) Current Topics in Solid State Physics*, *6*(SUPPL. 2), S972–S975. https://doi.org/10.1002/pssc.200880815

Iyechika, Y. (2010). Application of Graphene to High-Speed Transistors : Expectations and Challenges. *Science & Technology Trends*, *37*, 76–92.

Kim, K. S., Zhao, Y., Jang, H., Lee, S. Y., Kim, J. M., Kim, K. S., … Hong, B. H. (2009).

116

Large-scale pattern growth of graphene films for stretchable transparent electrodes. *Nature*, *457*(7230), 706–710. https://doi.org/10.1038/nature07719

Kimoto, T. (2015). Material science and device physics in SiC technology for high-voltage power devices. *Japanese Journal of Applied Physics*, *54*, 40103. https://doi.org/10.7567/JJAP.54.040103

Kimoto, T. (2016). *Bulk and epitaxial growth of silicon carbide*. *Progress in Crystal Growth and Characterization of Materials*. Elsevier Ltd. https://doi.org/10.1016/j.pcrysgrow.2016.04.018

Kimoto, T., & Cooper, J. A. (2014). *Fundamentals of Silicon Carbide Technology: Growth, Characterization, Devices and Applications*. *Fundamentals of Silicon Carbide Technology: Growth, Characterization, Devices and Applications*. Wiley. https://doi.org/10.1002/9781118313534

Kimoto, T., Hiyoshi, T., Hayashi, T., & Suda, J. (2010). Impacts of recombination at the surface and in the substrate on carrier lifetimes of n-type 4H-SiC epilayers. *Journal of Applied Physics*, *108*(8), 83721. https://doi.org/10.1063/1.3498818

Koley, G., Cha, H., Thomas, C. I., Spencer, M. G., Koley, G., Cha, H., … Spencer, M. G. (2002). Laser-induced surface potential transients observed in III-nitride heterostructures Laser-induced surface potential transients observed in III-nitride heterostructures. *Applied Physics Letters*, *81*(12), 2282. https://doi.org/10.1063/1.1506416

Kostov, P., Gaberl, W., & Zimmermann, H. (2013). High-speed bipolar phototransistors in a 180 nm CMOS process. *Optics and Laser Technology*, *46*(1), 6–13. https://doi.org/10.1016/j.optlastec.2012.04.011

Kunihiro Suzuki. (1991). Emitter and base transit time of polycrystalline silicon emitter contact bipolar transistors. *IEEE Transactions on Electron Devices*, *38*(11), 2512–2518.

Kusdemir, E., Ozkendir, D., Firat, V., & Celebi, C. (2015). Epitaxial graphene contact electrode for silicon carbide based ultraviolet photodetector. *Journal of Physics D: Applied Physics*, *48*(9), 95104. https://doi.org/10.1088/0022-3727/48/9/095104

Larkin, D. J., Neudeck, P. G., Powell, J. A., & Matus, L. G. (1994). Site-competition epitaxy for superior silicon carbide electronics. *Applied Physics Letters*, *65*(13), 1659–1661. https://doi.org/10.1063/1.112947

Lee, C., Wei, X., Kysar, J. W., & Hone, J. (2008). Measurement of the Elastic Properties and Intrinsic Strength of Monolayer Graphene. *Science*, *321*(July), 385–388. https://doi.org/10.1126/science.1157996

Luo, Z., Yu, T., Kim, K. J., Ni, Z., You, Y., Lim, S., … Lin, J. (2009). Thickness-dependent reversible hydrogenation of graphene layers. *ACS Nano*, *3*(7), 1781–1788. https://doi.org/10.1021/nn900371t

Lupina, G., Kitzmann, J., Costina, I., Lukosius, M., Wenger, C., Wolff, A., … Mehr, W. (2015). Residual metallic contamination of transferred chemical vapor deposited

117

graphene. *ACS Nano*, *9*(5), 4776–4785. https://doi.org/10.1021/acsnano.5b01261

Luxmi, Srivastava, N., He, G., & Feenstra, R. M. (2008). Comparison of Graphene Formation on C-face and Si-face SiC {0001} Surfaces. *Physical Review B*, *82*(23), 235406.

Macmillan, M. F., Henry, A., & Janzeni, E. (1998). Thickness determination of low doped SiC epi-films on highly doped SiC substrates. *Journal of Electronic Materials*, *27*(4), 300–303. Retrieved from http://www.scopus.com/scopus/inward/record.url?eid=2-s2.0-0011641368&partner=40&rel=R5.0.1

Matsunami, H., & Kimoto, T. (1997). Step-controlled epitaxial growth of SiC: High quality homoepitaxy. *Materials Science and Engineering R: Reports*, *20*(3), 125–166. https://doi.org/10.1016/S0927-796X(97)00005-3

Mattevi, C., Kim, H., & Chhowalla, M. (2011). A review of chemical vapour deposition of graphene on copper. *J. Mater. Chem.*, *21*(10), 3324–3334. https://doi.org/10.1039/C0JM02126A

Mazzillo, M., Condorelli, G., Castagna, M. E., Catania, G., Sciuto, A., Roccaforte, F., & Raineri, V. (2009). Highly efficient low reverse biased 4H-SiC schottky photodiodes for UV-light detection. *IEEE Photonics Technology Letters*, *21*(23), 1782–1784. https://doi.org/10.1109/LPT.2009.2033713

McWhorter, A. L. (1957). *1/f Noise and Germanium Surface Properties*. *Semiconductor Surface Physics*. University of Pennsylvania press. Retrieved from http://scholar.google.com/scholar?q=related:6AGLLYe9BPwJ:scholar.google.com/&hl=en&num=30&as_sdt=0,5%5Cnfile:///Users/timothyamorgan/Dropbox/Papers/Library.papers3/Articles/1957/McWhorter/1957 McWhorter1f noise and germanium surface properties.pdf%5Cnpape

Mishra, U. K., Parikh, P., & Wu, Y. F. (2002). AlGaN/GaN HEMTs - An overview of device operation and applications. *Proceedings of the IEEE*, *90*(6), 1022–1031. https://doi.org/10.1109/JPROC.2002.1021567

Monroy, E., Munoz, E., Sanchez, F. J., Calle, F., Calleja, E., Beaumont, B., … Cusso, F. (1998). High-performance GaN p-n junction photodetectors for solar ultraviolet applications. *Semiconductor Science and Technology*, *13*(9), 1042–1046.

Monroy, E., Omn s, F., & Calle, F. (2003). Wide-bandgap semiconductor ultraviolet photodetectors. *Semiconductor Science and Technology*, *18*(4), R33–R51. https://doi.org/10.1088/0268-1242/18/4/201

Monroy, E., Omnes, F., & Calle, F. (2003). Wide-bandgap semiconductor ultraviolet photodetectors. *Semiconductor Science and Technology*, *18*(4), R33–R51. https://doi.org/10.1088/0268-1242/18/4/201

Monroy, E., Omnès, F., & Calle, F. (2003). Wide-bandgap semiconductor ultraviolet photodetectors. *Semiconductor Science and Technology*, *18*(4). https://doi.org/10.1088/0268-1242/18/4/201

Mueller, T., Xia, F., Freitag, M., Tsang, J., & Avouris, P. (2009). The role of contacts in

graphene transistors : A scanning photocurrent study. *Physical Review B*, *79*(24), 245430.

Muhtadi, S., Hwang, S., Coleman, A., Asif, F., Lunev, A., Chandrashekhar, M. V. S., & Khan, A. (2017). High temperature operation of *n* -AlGaN channel metal semiconductor field effect transistors on low-defect AlN templates. *Applied Physics Letters*, *110*(19), 193501. https://doi.org/10.1063/1.4982656

Muhtadi, S., Hwang, S. M., Coleman, A., Asif, F., Simin, G., Chandrashekhar, M., & Khan, A. (2017). High Electron Mobility Transistors With Al 0.65 Ga 0.35 N Channel Layers on Thick AlN/Sapphire Templates. *IEEE Electron Device Letters*, *38*(7), 914–917. https://doi.org/10.1109/LED.2017.2701651

Muhtadi, S., Hwang, S. M., Coleman, A. L., Lunev, A., Asif, F., Chava, V. S. N., … Khan, A. (2017). High-speed solar-blind UV photodetectors using high-Al content Al0.64Ga0.36N/Al0.34Ga0.66N multiple quantum wells. *Applied Physics Express*, *10*(1), 11004. https://doi.org/10.7567/APEX.10.011004

Neto, A. H. C., Guinea, F., Peres, N. M. R., Novoselov, K. S., & Geim, A. K. (2009). The electronic properties of graphene. *Reviews of Modern Physics*, *81*(1), 109. https://doi.org/10.1126/science.1213003

Neudeck, P. G., Okojie, R. S., & Chen, L. Y. (2002). High-temperature electronics - A role for wide bandgap semiconductors? *Proceedings of the IEEE*, *90*(6), 1065–1076. https://doi.org/10.1109/JPROC.2002.1021571

Ni, Z., Chen, W., Fan, X., Kuo, J., Yu, T., Wee, A., & Shen, Z. (2008). Raman spectroscopy of epitaxial graphene on a SiC substrate. *Physical Review B*, *77*(11), 115416. https://doi.org/10.1103/PhysRevB.77.115416

Novoselov, K. S., Fal'Ko, V. I., Colombo, L., Gellert, P. R., Schwab, M. G., & Kim, K. (2012). A roadmap for graphene. *Nature*, *490*(7419), 192–200. https://doi.org/10.1038/nature11458

Novoselov, K. S., Geim, A. K., Morozov, S. V, Jiang, D. A., Zhang, Y., Dubonos, S. V, … Firsov, A. A. (2004). Electric field effect in atomically thin carbon films. *Science*, *306*(5696), 666–669. https://doi.org/10.1126/science.1102896

Osinsky, A., Gangopadhyay, S., Lim, B. W., Anwar, M. Z., Khan, M. A., Kuksenkov, D. V., & Temkin, H. (1998). Schottky barrier photodetectors based on AlGaN. *Applied Physics Letters*, *72*(6), 742–744. https://doi.org/10.1063/1.120862

Osinsky, A., Gangopadhyay, S., Yang, J. W., Gaska, R., Kuksenkov, D., Temkin, H., … Kolbas, R. M. (1998). Visible-blind GaN Schottky barrier detectors grown on Si(111). *Applied Physics Letters*, *72*(5), 551–553. https://doi.org/10.1063/1.120755

Pedersen, H., Leone, S., Kordina, O., Henry, A., Nishizawa, S. I., Koshka, Y., & Janzén, E. (2012). Chloride-based CVD growth of silicon carbide for electronic applications. *Chemical Reviews*, *112*(4), 2434–2453. https://doi.org/10.1021/cr200257z

Pei, S., & Cheng, H. M. (2012). The reduction of graphene oxide. *Carbon*, *50*(9), 3210–3228. https://doi.org/10.1016/j.carbon.2011.11.010

119

Rana, T. (2013). *HIGH QUALITY SILICON CARBIDE EPITAXIAL GROWTH BY NOVEL FLUOROSILANE GAS CHEMISTRY FOR NEXT GENERATION HIGH POWER ELECTRONICS*.

Rana, T., Chandrashekhar, M. V. S., Daniels, K., & Sudarshan, T. (2015). Epitaxial growth of graphene on SiC by Si selective etching using SiF4 in an inert ambient. *Japanese Journal of Applied Physics*, *54*(3), 30304. https://doi.org/10.7567/JJAP.54.030304

Rana, T., Chandrashekhar, M. V. S., & Sudarshan, T. S. (2012). Elimination of silicon gas phase nucleation using tetrafluorosilane (SiF4) precursor for high quality thick silicon carbide (SiC) homoepitaxy. *Physica Status Solidi (A) Applications and Materials Science*, *209*(12), 2455–2462. https://doi.org/10.1002/pssa.201228319

Razeghi, M. (2002). Short-Wavelength Solar-Blind Detectors — Status , Prospects , and Markets. *Proceedings of the IEEE*, *90*(6), 1006–1014.

Razeghi, M., & Rogalski, A. (1996). Semiconductor ultraviolet detectors. *Journal of Applied Physics*, *79*(10), 7433–7473. https://doi.org/10.1063/1.362677

Riedl, C., Coletti, C., Iwasaki, T., Zakharov, A. A., & Starke, U. (2009). Quasi-free Standing Epitaxial Graphene on SiC by Hydrogen Intercalation. *Physical Review Letters*, *103*(24), 246804. https://doi.org/10.1103/PhysRevLett.103.246804

Robinson, J. A., Wetherington, M., Tedesco, J. L., Campbell, P. M., Weng, X., Stitt, J., … Gaskill, D. K. (2009). Correlating Raman Spectral Signatures with Carrier Mobility in Epitaxial Graphene : A Guide to Achieving High Mobility on the Wafer Scale 2009. *Nano Letters*, *9*(8), 2873–2876. https://doi.org/10.1021/nl901073g

Rumyantsev, S., Liu, G., Stillman, W., Shur, M., & Balandin, a. a. (2010). Electrical and Noise Characteristics of Graphene Field-Effect Transistors: Ambient Effects and Noise Sources. *Journal of Physics: Condensed Matter*, *22*(39), 395302. Retrieved from http://arxiv.org/abs/1008.2990

Schoen, K. J., Woodall, J. M., Cooper, J. a., & Melloch, M. R. (1998). Design considerations and experimental analysis of high-voltage SiC Schottky barrier rectifiers. *IEEE Transactions on Electron Devices*, *45*(7), 1595–1604. https://doi.org/10.1109/16.701494

Sciuto, A., Roccaforte, F., Di Franco, S., Liotta, S. F., Bonanno, G., & Raineri, V. (2007). High efficiency 4H-SiC Schottky UV-photodiodes using self-aligned semitransparent contacts. *Superlattices and Microstructures*, *41*(1), 29–35. https://doi.org/10.1016/j.spmi.2006.10.002

Sciuto, A., Roccaforte, F., Franco, S. Di, Raineri, V., & Bonanno, G. (2006). High responsivity 4 H -SiC Schottky UV photodiodes based on the pinch-off surface effect. *Applied Physics Letters*, *89*(8), 81111. https://doi.org/10.1063/1.2337861

Shaffer, P. T. B. (1969). A review of the structure of silicon carbide. *Acta Crystallographica Section B Structural Crystallography and Crystal Chemistry*, *25*(3), 477–488. https://doi.org/10.1107/S0567740869002457

Shetu, S. S., Omar, S. U., Daniels, K. M., Daas, B., Andrews, J., Ma, S., …

Chandrashekhar, M. V. S. (2013). Si-adatom kinetics in defect mediated growth of multilayer epitaxial graphene films on 6H-SiC. *Journal of Applied Physics*, *114*(16), 164903. https://doi.org/10.1063/1.4826899

Singh, A., Uddin, M. A., Sudarshan, T., & Koley, G. (2014). Tunable reverse-biased graphene/silicon heterojunction Schottky diode sensor. *Small*, *10*(8), 1555–1565. https://doi.org/10.1002/smll.201302818

Song, H., Chandrashekhar, M. V. S., & Sudarshan, T. S. (2014). Study of Surface Morphology, Impurity Incorporation and Defect Generation during Homoepitaxial Growth of 4H-SiC Using Dichlorosilane. *ECS Journal of Solid State Science and Technology*, *4*(3), P71–P76. https://doi.org/10.1149/2.0071503jss

Sridhara, S. ., Eperjesi, T. ., Devaty, R. ., & Choyke, W. . (1999). Penetration depths in the ultraviolet for 4H, 6H and 3C silicon carbide at seven common laser pumping wavelengths. *Materials Science and Engineering: B*, *61–62*, 229–233. https://doi.org/10.1016/S0921-5107(98)00508-X

Sridhara, S. G., Devaty, R. P., & Choyke, W. J. (1998). Absorption coefficient of 4H silicon carbide from 3900 to 3250 Å. *Journal of Applied Physics*, *84*(5), 2963–2964. https://doi.org/10.1063/1.368403

Su, Y. K., Chang, S. J., Chen, C. H., Chen, J. F., Chi, G. C., Sheu, J. K., … Tsai, J. M. (2002). GaN metal-semiconductor-metal ultraviolet sensors with various contact electrodes. *IEEE Sensors Journal*, *2*(4), 366–371. https://doi.org/10.1016/j.jcrysgro.2006.03.059

Su, Y. K., Chiou, Y. Z., Chang, C. S., Chang, S. J., Lin, Y. C., & Chen, J. F. (2002). 4H-SiC metal-semiconductor-metal ultraviolet photodetectors with Ni/ITO electrodes. *Solid-State Electronics*, *46*(12), 2237–2240. https://doi.org/10.1016/S0038-1101(02)00234-4

Su, Y. K., Wei, S. C., Wang, R. L., Chang, S. J., Ko, C. H., & Kuan, T. M. (2003). Flicker Noise of GaN-Based Heterostructure Field-Effect Transistors With Si-Doped AlGaN Carrier Injection Layer. *IEEE Electron Device Letters*, *24*(10), 622–624. https://doi.org/10.1109/LED.2003.817869

Sutter, P. W., Flege, J. I., & Sutter, E. A. (2008). Epitaxial graphene on ruthenium. *Nature Materials*, *7*(5), 406–411. https://doi.org/10.1038/nmat2166

Sze, S., & Ng, K. (2006). *Physics of semiconductor devices*. Wiley. Retrieved from https://books.google.com/books?hl=en&lr=&id=o4unkmHBHb8C&oi=fnd&pg=PR7&dq=S.M.Sze+Physics+of+semiconductor+devices+3rd+edition&ots=wGqkcJCk1W&sig=Idm6PYZeltLQVBZ7-Fg0ShYyZYE

Terrones, M., Botello-Méndez, A. R., Campos-Delgado, J., López-Urías, F., Vega-Cantú, Y. I., Rodríguez-Macías, F. J., … Terrones, H. (2010). Graphene and graphite nanoribbons: Morphology, properties, synthesis, defects and applications. *Nano Today*, *5*(4), 351–372. https://doi.org/10.1016/j.nantod.2010.06.010

Tongay, S., Lemaitre, M., Miao, X., Gila, B., Appleton, B. R., & Hebard, A. F. (2012).

Rectification at graphene-semiconductor interfaces: Zero-gap semiconductor-based diodes. *Physical Review X*, *2*(1), 11002. https://doi.org/10.1103/PhysRevX.2.011002

Tongay, S., Schumann, T., & Hebard, A. F. (2009). Graphite based Schottky diodes formed on Si , GaAs , and 4H-SiC substrates. *Applied Physics Letters*, *95*(22), 222103. https://doi.org/10.1063/1.3268788

Varchon, F., Feng, R., Hass, J., Li, X., Nguyen, B. N., Naud, C., … Magaud, L. (2007). Electronic structure of epitaxial graphene layers on SiC: effect of the substrate. *Physical Review Letters*, *99*(12), 126805. https://doi.org/10.1103/PhysRevLett.99.126805

Walker, D., Zhang, X., Kung, P., Saxler, A., Javadpour, S., Xu, J., & Razeghi, M. (1996). AlGaN ultraviolet photoconductors grown on sapphire. *Applied Physics Letters*, *68*(15), 2100–2101. https://doi.org/10.1063/1.115597

Wallace, P. R. (1947). The band theory of graphite. *Physical Review*, *71*(9), 622–634. https://doi.org/10.1103/PhysRev.71.622

Wang, C. K., Chang, S. J., Su, Y. K., Chiou, Y. Z., Chen, S. C., Chang, C. S., … Tang, J. J. (2006). GaN MSM UV photodetectors with titanium tungsten transparent electrodes. *IEEE Transactions on Electron Devices*, *53*(1), 38–42. https://doi.org/10.1109/TED.2005.860780

Wijesundara, M. B. J., & Azevedo, R. (2011). *Silicon Carbide Microsystems for Harsh Environments*. *Springer Science & Business Media* (Vol. 22). https://doi.org/10.1007/978-1-4419-7121-0

Wright, N. G., & Horsfall, A. B. (2007). SiC sensors: a review. *Journal of Physics D: Applied Physics*, *40*(20), 6345–6354. https://doi.org/10.1088/0022-3727/40/20/S17

Y.Mizushima, Y. A. and. (1984). Bipolar-mode Schottky contact and applications to high-speed diodes. *IEEE Transactions on Electron Devices*, *31*(1), 35–42.

Yang, W, Nohava, T., Krishnankutty, S., Torreano, R., Mcpherson, S., & Marsh, H. (1998). High gain GaN / AlGaN heterojunction phototransistor. *Applied Physics Letters*, *73*(7), 978–981.

Yang, W., Nohava, T., Krishnankutty, S., Torreano, R., McPherson, S., & Marsh, H. (1998). High gain GaN/AlGaN heterojunction phototransistor. *Applied Physics Letters*, *73*(7), 978–980. https://doi.org/10.1063/1.122058

Yoshida, S., Misawa, S., & Gonda, S. (1982). Properties of AlxGa1-xN films prepared by reactive molecular beam epitaxy Properties of Alx Ga 1 _ x N films prepared by reactive molecular beam epitaxy. *Journal of Applied Physics*, *53*(10), 6844–6848. https://doi.org/10.1063/1.329998

Yoshikawa, A., Ushida, S., Nagase, K., Iwaya, M., Takeuchi, T., Kamiyama, S., & Akasaki, I. (2017). High-performance solar-blind Al0.6Ga0.4N/Al0.5Ga0.5N MSM type photodetector. *Applied Physics Letters*, *111*(19), 191103.

Yoshikawa, A., Yamamoto, Y., Murase, T., Iwaya, M., Takeuchi, T., Kamiyama, S., &

122

Akasaki, I. (2016). High-photosensitivity AlGaN-based UV heterostructure-field-effect-transistor-type photosensors. *Japanese Journal of Applied Physics*, *55*, 05FJ04.

Zhang, N. (2011). *Characterization of Dislocations Structures and Properties in Silicon Carbide Bulk Crystals and Epilayers*. Retrieved from http://dspace.sunyconnect.suny.edu/bitstream/handle/1951/51169/000000658.sbu.pdf?sequence=1

Zhang, Z., & Sudarshan, T. S. (2005). Basal plane dislocation-free epitaxy of silicon carbide. *Applied Physics Letters*, *87*(15), 151913. https://doi.org/10.1063/1.2093931

Zhu, H., Chen, X., Cai, J., & Wu, Z. (2009). 4H-SiC ultraviolet avalanche photodetectors with low breakdown voltage and high gain. *Solid-State Electronics*, *53*(1), 7–10. https://doi.org/10.1016/j.sse.2008.09.002

APPENDIX A: PERMISSION TO REPRINT

CHAPTER 3:

AIP PUBLISHING LICENSE
TERMS AND CONDITIONS

Apr 12, 2018

This Agreement between University of South Carolina Columbia -- VENKATA SURYA NAGA RAJU CHAVA ("You") and AIP Publishing ("AIP Publishing") consists of your license details and the terms and conditions provided by AIP Publishing and Copyright Clearance Center.

License Number	4324400706550
License date	Apr 08, 2018
Licensed Content Publisher	AIP Publishing
Licensed Content Publication	Applied Physics Letters
Licensed Content Title	Evidence of minority carrier injection efficiency >90% in an epitaxial graphene/SiC Schottky emitter bipolar junction phototransistor for ultraviolet detection
Licensed Content Author	Venkata S. N. Chava, Sabih U. Omar, Gabriel Brown, et al
Licensed Content Date	Jan 25, 2016
Licensed Content Volume	108
Licensed Content Issue	4
Type of Use	Thesis/Dissertation
Requestor type	Author (original article)
Format	Print and electronic
Portion	Excerpt (> 800 words)
Will you be translating?	No
Title of your thesis / dissertation	STUDY OF 4H-SIC AND ALXGA1-XN BASED HETEROJUNCTION DEVICES FOR ULTRAVIOLET DETECTION APPLICATIONS
Expected completion date	Apr 2018
Estimated size (number of pages)	150
Requestor Location	University of South Carolina Columbia 301 Main St, Room 3A 80
	COLUMBIA, SC 29208 United States Attn: Venkata S.N.
Billing Type	Invoice
Billing Address	University of South Carolina Columbia 301 Main St, Room 3A 80
	COLUMBIA, SC 29208 United States Attn: Venkata S.N.
Total	0.00 USD

Terms and Conditions

AIP Publishing -- Terms and Conditions: Permissions Uses

AIP Publishing hereby grants to you the non-exclusive right and license to use and/or distribute the Material according to the use specified in your order, on a one-time basis, for the specified term, with a maximum distribution equal to the number that you have ordered. Any links or other content accompanying the Material are not the subject of this license.

124

1. You agree to include the following copyright and permission notice with the reproduction of the Material:"Reprinted from [FULL CITATION], with the permission of AIP Publishing." For an article, the credit line and permission notice must be printed on the first page of the article or book chapter. For photographs, covers, or tables, the notice may appear with the Material, in a footnote, or in the reference list.

2. If you have licensed reuse of a figure, photograph, cover, or table, it is your responsibility to ensure that the material is original to AIP Publishing and does not contain the copyright of another entity, and that the copyright notice of the figure, photograph, cover, or table does not indicate that it was reprinted by AIP Publishing, with permission, from another source. Under no circumstances does AIP Publishing purport or intend to grant permission to reuse material to which it does not hold appropriate rights.

   You may not alter or modify the Material in any manner. You may translate the Material into another language only if you have licensed translation rights. You may not use the Material for promotional purposes.

3. The foregoing license shall not take effect unless and until AIP Publishing or its agent, Copyright Clearance Center, receives the Payment in accordance with Copyright Clearance Center Billing and Payment Terms and Conditions, which are incorporated herein by reference.

4. AIP Publishing or Copyright Clearance Center may, within two business days of granting this license, revoke the license for any reason whatsoever, with a full refund payable to you. Should you violate the terms of this license at any time, AIP Publishing, or Copyright Clearance Center may revoke the license with no refund to you. Notice of such revocation will be made using the contact information provided by you. Failure to receive such notice will not nullify the revocation.

5. AIP Publishing makes no representations or warranties with respect to the Material. You agree to indemnify and hold harmless AIP Publishing, and their officers, directors, employees or agents from and against any and all claims arising out of your use of the Material other than as specifically authorized herein.

6. The permission granted herein is personal to you and is not transferable or assignable without the prior written permission of AIP Publishing. This license may not be amended except in a writing signed by the party to be charged.

7. If purchase orders, acknowledgments or check endorsements are issued on any forms containing terms and conditions which are inconsistent with these provisions, such inconsistent terms and conditions shall be of no force and effect. This document, including the CCC Billing and Payment Terms and Conditions, shall be the entire agreement between the parties relating to the subject matter hereof.

This Agreement shall be governed by and construed in accordance with the laws of the State of New York. Both parties hereby submit to the jurisdiction of the courts of New York County for purposes of resolving any disputes that may arise hereunder.

V1.2

Questions? customercare@copyright.com or +1-855-239-3415 (toll free in the US) or +1-978-646-2777.

125

www.manaraa.com

IEEE

Requesting permission to reuse content from an IEEE publication

Title: Epitaxial graphene (EG)/SiC based Schottky emitter bipolar phototransistors for UV detection and effect of hydrogen intercalation on device I-V characteristics

Conference Proceedings: SENSORS, 2016 IEEE

Author: Venkata S.N. Chava

Publisher: IEEE

Date: Oct. 2016

Copyright © 2016, IEEE

Logged in as:
VENKATA SURYA NAGA RAJU CHAVA
University of South Carolina Columbia
Account #:
3001271416

LOGOUT

Thesis / Dissertation Reuse

The IEEE does not require individuals working on a thesis to obtain a formal reuse license, however, you may print out this statement to be used as a permission grant:

Requirements to be followed when using any portion (e.g., figure, graph, table, or textual material) of an IEEE copyrighted paper in a thesis:

1) In the case of textual material (e.g., using short quotes or referring to the work within these papers) users must give full credit to the original source (author, paper, publication) followed by the IEEE copyright line © 2011 IEEE.
2) In the case of illustrations or tabular material, we require that the copyright line © [Year of original publication] IEEE appear prominently with each reprinted figure and/or table.
3) If a substantial portion of the original paper is to be used, and if you are not the senior author, also obtain the senior author's approval.

Requirements to be followed when using an entire IEEE copyrighted paper in a thesis:

1) The following IEEE copyright/ credit notice should be placed prominently in the references: © [year of original publication] IEEE. Reprinted, with permission, from [author names, paper title, IEEE publication title, and month/year of publication]
2) Only the accepted version of an IEEE copyrighted paper can be used when posting the paper or your thesis on-line.
3) In placing the thesis on the author's university website, please display the following message in a prominent place on the website: In reference to IEEE copyrighted material which is used with permission in this thesis, the IEEE does not endorse any of [university/educational entity's name goes here]'s products or services. Internal or personal use of this material is permitted. If interested in reprinting/republishing IEEE copyrighted material for advertising or promotional purposes or for creating new collective works for resale or redistribution, please go to http://www.ieee.org/publications_standards/publications/rights/rights_link.html to learn how to obtain a License from RightsLink.

If applicable, University Microfilms and/or ProQuest Library, or the Archives of Canada may supply single copies of the dissertation.

BACK | CLOSE WINDOW

Dear Surya Chava,

Thank you for your email.

I have chased this request on the CCC and it has now been processed.

Kind regards,
Christina

Copyright & Permissions Team
Gemma Alaway – Senior Rights & Permissions Adviser
Christina Colwell - Rights & Permissions Assistant

Contact Details
E-mail: permissions@iop.org
For further information about copyright and how to request permission: http://iopscience.iop.org/page/copyright
Please see our Author Rights Policy http://ioppublishing.org/author-rights/
Please note: We do not provide signed permission forms as a separate attachment. Please print this email and provide it to your publisher as proof of permission.

Please note: Any statements made by IOP Publishing to the effect that authors do not need to get permission to use any content where IOP Publishing is not the publisher is not intended to constitute any sort of legal advice. Authors must make their own decisions as to the suitability of the content they are using and whether they require permission for it to be published within their article.

CHAPTER-4:

AIP PUBLISHING LICENSE
TERMS AND CONDITIONS

Apr 12, 2018

This Agreement between University of South Carolina Columbia -- VENKATA SURYA NAGA RAJU CHAVA ("You") and AIP Publishing ("AIP Publishing") consists of your license details and the terms and conditions provided by AIP Publishing and Copyright Clearance Center.

License Number	4324410265369
License date	Apr 08, 2018
Licensed Content Publisher	AIP Publishing
Licensed Content Publication	Applied Physics Letters
Licensed Content Title	High detectivity visible-blind SiF4 grown epitaxial graphene/SiC Schottky contact bipolar phototransistor
Licensed Content Author	Venkata S. N. Chava, Bobby G. Barker, Anusha Balachandran, et al
Licensed Content Date	Dec 11, 2017
Licensed Content Volume	111
Licensed Content Issue	24
Type of Use	Thesis/Dissertation
Requestor type	Author (original article)
Format	Print and electronic
Portion	Excerpt (> 800 words)
Will you be translating?	No
Title of your thesis / dissertation	STUDY OF 4H-SIC AND ALXGA1-XN BASED HETEROJUNCTION DEVICES FOR ULTRAVIOLET DETECTION APPLICATIONS
Expected completion date	Apr 2018
Estimated size (number of pages)	150
Requestor Location	University of South Carolina Columbia 301 Main St, Room 3A 80 COLUMBIA, SC 29208 United States Attn: Venkata S.N.
Billing Type	Invoice
Billing Address	University of South Carolina Columbia 301 Main St, Room 3A 80 COLUMBIA, SC 29208 United States Attn: Venkata S.N.
Total	0.00 USD

Terms and Conditions

AIP Publishing -- Terms and Conditions: Permissions Uses

AIP Publishing hereby grants to you the non-exclusive right and license to use and/or distribute the Material according to the use specified in your order, on a one-time basis, for the specified term, with a maximum distribution equal to the number that you have ordered. Any links or other content accompanying the Material are not the subject of this license.

www.manaraa.com